

Shaped femtosecond pulses for coherent control transported via an optical fiber in the nonlinear regime



am
Fachbereich Physik
der
Freien Universität Berlin
eingereichte Dissertation

vorgelegt von
Monika Pawłowska

Berlin 2012

Erstgutachter: Prof. Dr. Ludger Wöste

Zweitgutachterin: Prof. Dr. Vlasta Bonačić-Koutecký

Tag der Disputation: 22. Juni 2012

Abstract

The aim of this work was to explore the possibilities of transporting shaped ultrashort laser pulses through an optical fiber in the nonlinear regime and applying them to coherent control of multi-photon processes. As a result, two approaches have been developed and their functionality has been proven experimentally.

Many research fields, notably life sciences, can benefit from transporting shaped femtosecond pulses through optical fibers. However, ultrashort pulses propagating in a fiber are distorted due to linear and nonlinear effects including chromatic dispersion, birefringence and self-phase modulation. These effects become significant already for pulse energies of the order of 0.1 nJ and are detrimental to transporting shaped femtosecond pulses even through short pieces of fiber. Therefore compensating for these effects is a prerequisite for any experiment involving shaped laser pulses and fibers.

In this work two approaches to applying shaped pulses transported through a fiber to coherent control are presented. The first part concerns excitation of two-photon transitions with phase-shaped pulses. It is shown that certain antisymmetric spectral phase functions combined with a phase offset for chromatic dispersion compensation partly retain their shape during propagation in the fiber in spite of self-phase modulation. This is sufficient for efficient and selective excitation of two-photon transitions, although the selectivity decreases with increasing pulse energy. Presented measurements for pulse energies up to 1 nJ are supported by simulations of nonlinear propagation based on numerically solving the nonlinear Schrödinger equation.

The other demonstrated approach is reverse propagation, a method that enables obtaining arbitrarily shaped pulses after nonlinear propagation through a fiber. Contrary to the previous approach it is not limited to two-photon transitions. On the other hand it requires a precise knowledge of linear and nonlinear properties of the fiber. Accordingly, the first step is performing a measurement of the dispersion and the nonlinear refractive index. Next, backward propagation of the desired output pulse shape through the fiber is simulated numerically to obtain the required input pulse shape and the corresponding phase and transmission mask of the modulator is calculated. The method is tested by generating and characterizing several series of phase and amplitude shaped pulses.

Finally, both methods are applied to selective two-photon excitation of molecules in solution. The laser dyes used for demonstration purposes have broad, overlapping absorption spectra which is typical for fluorophores used in biological imaging. It is shown that in spite of spectral narrowing of the pulse in the fiber a contrast that should be sufficient for imaging purposes can be achieved.

Kurzfassung

Ziel dieser Arbeit war es, die Möglichkeiten der Übertragung geformter, ultrakurzer Laserpulse durch eine optische Faser im nichtlinearen Pulsenergiebereich und ihre Verwendung zur kohärenten Kontrolle von Mehrphotonenprozessen zu erforschen. Als Ergebnis wurden zwei unterschiedliche Verfahren entwickelt, deren korrekte Funktionsweise experimentell nachgewiesen wurde.

Viele Forschungsfelder, insbesondere die Biowissenschaften, können von der Übertragung geformter Femtosekundenlaserpulse profitieren. Allerdings werden ultrakurze Pulse in einer Glasfaser durch lineare und nichtlineare Effekte verzerrt, unter anderem durch chromatische Dispersion, Doppelbrechung und Selbstphasenmodulation. Diese schädlichen Effekte werden bereits bei Pulsenergien in der Größenordnung von 0,1 Nanojoule und Übertragung durch kurze Faserstücke signifikant. Daher ist die Kompensation dieser Effekte für alle Experimente mit geformten Laserpulsen in Fasern eine notwendige Voraussetzung.

In dieser Arbeit werden zwei Ansätze zur kohärenten Kontrolle mit geformten Pulsen, die durch eine Faser transportiert werden, präsentiert. Der erste Teil befasst sich mit der Anregung von Zweiphotonenübergängen mit phasengeformten Pulsen. Es wird gezeigt, dass die Form bestimmter antisymmetrischer spektraler Phasenfunktionen, in Verbindung mit einem Phasoffset zur Kompensation der chromatischen Dispersion, trotz Selbstphasenmodulation teilweise erhalten bleibt. Dies ermöglicht es, Zweiphotonenübergänge effektiv und selektiv anzuregen, wobei jedoch die Selektivität mit zunehmender Pulsenergie abnimmt. Die aufgeführten Messergebnisse für Pulsenergien bis 1 Nanojoule werden durch die Simulationen der nichtlinearen Ausbreitung mittels numerische Lösung der nichtlinearen Schrödingergleichung bestätigt.

Der andere Ansatz ist die Rückrechnung, eine Methode, die es ermöglicht, nach der Übertragung durch eine Faser beliebig geformte Pulse zu erhalten. Der Ansatz ist, im Gegensatz zum vorherigen, nicht auf Zweiphotonenübergänge beschränkt. Er erfordert jedoch eine genaue Kenntnis der linearen und nichtlinearen Eigenschaften der Faser. Deswegen ist der erste Schritt die Messung der Dispersion und des nichtlinearen Brechungsindex. Anschließend wird die Ausbreitung der gewünschten Pulsform rückwärts durch die Faser numerisch simuliert, um die benötigte Eingangspulsform und die entsprechende Phasen- und Amplitudenmaske des Pulsformers zu berechnen. Die Methode wird durch Erzeugung und Vermessung von mehreren Serien phasen- und amplitudengeformter Pulse getestet.

Zuletzt werden beide Methoden auf die selektive zweiphotonische Anregung von Molekülen in einer Lösung angewendet. Die für die Demonstration verwendeten Laserfarbstoffe haben breite, überlappende Absorptionsspektren, wie es auch für Luminophoren im biologischen bildgebenden Verfahren typisch ist. Es wird gezeigt, dass obwohl das Pulsspektrum nach der Faser schmaler wird, ein für ein bildgebendes Verfahren ausreichender Kontrast erreicht werden kann.

Contents

Acronyms	vi
1 Introduction	1
2 Fundamentals	3
2.1 Electromagnetic wave propagation	3
2.1.1 Wave equation	3
2.1.2 Gaussian beam	5
2.1.3 Fiber modes	6
2.2 Pulsed light	6
2.2.1 Mathematical description of laser pulses	6
2.2.2 Pulse shaping and coherent control	8
2.3 Second-order nonlinear processes	9
2.3.1 Second-harmonic generation	9
2.3.2 Two-photon absorption	12
2.3.3 Coherent control of two-photon processes	13
2.4 Nonlinear effects in an optical fiber	16
2.4.1 Third-order nonlinear processes	16
2.4.2 Nonlinear Schrödinger equation	17
2.4.3 Consequences of self-phase modulation	18
2.4.4 Higher-order nonlinear effects	19
2.4.5 Split-Step Fourier Method	20
2.5 Jones formalism for polarized light	20
3 Experimental setup	21
3.1 Femtosecond pulse generation	21
3.1.1 Oscillator	21
3.1.2 Amplifier	21
3.1.3 Pulse compression	21
3.2 Pulse shaping	22
3.2.1 Liquid crystal modulator	22
3.2.2 $4f$ setup	24
3.2.3 Phase and amplitude shaping	25
3.2.4 Polarization shaping	26
3.2.5 Limitations of a pulse shaper	28
3.3 Pulse characterization	30
3.3.1 Autocorrelation	31
3.3.2 Cross-correlation and XFROG	31
3.3.3 Polarization shaped pulses	32
3.3.4 Optimization of the pulse duration	32
3.4 Test systems: nonlinear crystals and dyes	33
3.4.1 BBO crystals	33
3.4.2 Laser dyes	34

4	Optical fiber	37
4.1	Coupling light into the fiber	37
4.1.1	Mode diameter matching	37
4.1.2	Influence of space-time coupling on the output pulse spectrum	37
4.2	Polarization properties	38
4.3	Chromatic dispersion and nonlinear effects	40
4.3.1	Pulse width and duration measurements	40
4.3.2	Simulations and fiber dispersion measurement	41
4.4	Parametrically shaped pulses in the linear regime	44
4.4.1	Short pulse	44
4.4.2	Complex pulse trains	45
5	Coherent control of two-photon transitions	51
5.1	Preliminary measurements	51
5.1.1	Measurements without fiber	51
5.1.2	Antisymmetric phase after nonlinear propagation: proof of principle	54
5.2	Optimization of the spectral phase	54
5.2.1	Single-objective optimization	55
5.2.2	Multi-objective optimization	56
5.2.3	Optimization for different transition wavelengths	57
5.3	Selective excitation	59
5.3.1	Measurements with pulses with a π step spectral phase	59
5.3.2	Propagation simulation for the π step spectral phase	61
5.3.3	Other phase functions	63
5.4	Polarization shaped pulses	64
6	Reverse propagation	69
6.1	Method description	69
6.1.1	Motivation and previous work	69
6.1.2	The principle of reverse propagation	71
6.1.3	Algorithm	72
6.2	Determination of the simulation parameters	72
6.2.1	Chromatic dispersion	73
6.2.2	Nonlinear refractive index	73
6.2.3	Laser pulse parameters	74
6.3	Examples of parametrically shaped pulses	74
6.3.1	Oscillator pulses	75
6.3.2	Amplified pulses	78
6.3.3	Pulses with antisymmetric spectral phase	83
6.4	Discussion	84
7	Selective excitation of molecules in solution	87
7.1	Motivaton	87
7.2	Measurements without fiber	88
7.3	Phase shaped pulses	92
7.4	Phase and amplitude shaped pulses	95
7.4.1	Pulses with variable central wavelength generated by reverse propagation	95
7.4.2	Selective excitation results	95
7.5	Discussion	98

Contents **v**

8 Summary **101**

Bibliography **103**

Appendices **109**

 List of publications 110

 Acknowledgements 111

Acronyms

AOPDF acousto-optic programmable dispersive filter

BBO β barium borate

DFG difference-frequency generation

FWHM full width at half maximum

GVD group-velocity dispersion

HWP half wave plate

LC liquid crystal

NLSE nonlinear Schrödinger equation

QWP quarter wave plate

SFG sum-frequency generation

SH second harmonic

SHG second-harmonic generation

SLM spatial light modulator

SPM self-phase modulation

THG third-harmonic generation

TL transform limited

TOD third-order dispersion

TP two-photon

TPA two-photon absorption

XC cross-correlation

XFROG cross-correlation frequency resolved optical gating

XPM cross-phase modulation

Introduction

1

Light is an excellent tool for investigating and controlling the processes of nature. In the history of physics, optical spectroscopy contributed to the development of quantum mechanics by providing results about energy states of atoms that could not be explained using classical physics. In modern physics an important milestone was the development of the laser in the 1960s. Since this time the laser became an essential tool in many research fields. While continuous, narrow band lasers enable extremely precise measurements of optical frequencies, mode-locked pulsed lasers have opened the way to studying processes happening on timescales that are inaccessible to other measurement techniques. In particular, photoinduced processes in molecules take place on a picosecond and often even femtosecond timescale. This makes femtosecond laser pulses an invaluable tool for studying chemical reactions.

The stimulated emission that is the underlying principle of the laser operation was a theoretical discovery by Einstein. It is an excellent example how something that at first seems an obscure quantum mechanical effect can lead to applications not only in experimental sciences but also in daily life. Another example of how a fundamental physical effect - in this case guided propagation of light - leads to technologies that nowadays became indispensable is the optical fiber. The first, then still short and lossy, optical fibers appeared in 1920s. Now they are used everywhere where the light cannot be transported simply by sending a collimated beam in a straight line, whether due to distance as in transatlantic communication or due to difficult access as in endoscopic devices.

Combining ultrashort pulses with optical fibers is attractive for many applications. The most prominent example are life sciences. In recent years many methods benefiting from the high peak power and broad frequency spectrum of ultrashort laser pulses have been developed. Some of them are briefly described in section 7.1 of this work. Combining those techniques with endoscopic devices based on optical fibers would allow to use them in *in vivo* applications. Another aspect is that in life sciences stable, hands-off operation is desirable and it becomes a prerequisite if living animals or people are involved. Fiber-coupled devices fulfill this condition much easier than free-space ones. More generally, any experiment that involves bringing ultrashort laser pulses to an inaccessible or remote place can benefit from transporting them through an optical fiber. However, optical properties of fibers make delivering coherent, spectrally broad pulses with high peak power challenging. Chromatic dispersion, birefringence and nonlinear effects cause distortions that stretch the pulse temporally and change its polarization and spectral width.

So far most of the experiments with transporting femtosecond laser pulses through optical fibers concentrated on obtaining pulses that remained as short and broadband as possible. A short review of these attempts is given in section 6.1.1. Most of those methods cannot be extended to delivering arbitrarily shaped pulses. However, by limiting oneself to Fourier transform-limited pulses one loses one of the biggest advantages of using mode-locked lasers which is having at one's disposal a continuous broad spectrum of phase-locked frequencies that can be used to excite coherent wavepackets. The spectral phase and amplitude of the laser pulse determines the relative phases of the different quantum states constituting the wavepacket and thus leads to constructive or destructive interference. This way the final quantum state of the system can be controlled. This is the underlying idea behind the concept of coherent control.

In this work I demonstrate some approaches to coherent control with shaped ultrashort pulses transported through an optical fiber in the nonlinear regime, that is with both linear and nonlinear effects significantly influencing the pulse during the propagation through the fiber. In the first

part I concentrate on one class of processes, namely coherent two-photon processes. I investigate the possibility of extending the method of controlling such processes with phase-shaped pulses to pulses distorted by nonlinear effects in the fiber. In the second part I present a more general approach of generating arbitrarily shaped pulses after transmission through the fiber, that is reverse propagation. This method is also subsequently applied to coherent control of two-photon absorption.

The text is organized as follows: in chapter 2 I introduce the fundamental physical concepts that form the theoretical basis of the presented experiments. First, the laws governing the propagation of light in a medium are summarized. Several aspects, including the transverse distribution of electric field and mathematical description of ultrashort pulses are discussed in more detail. Special attention is devoted to nonlinear effects. In section 2.3, two-photon nonlinear effects and their coherent control are described. Section 2.4 concerns third- and higher-order nonlinear effects in an optical fiber. Finally, in section 2.5 the Jones formalism for describing polarized light is introduced.

Chapters 3 and 4 concern the experimental aspects of this work. In chapter 3 I describe the setup for generating, shaping and characterizing the ultrashort pulses. I also introduce the systems that were the subjects of coherent control. Chapter 4 concentrates on one part of the experimental setup, that is the optical fiber. I describe the technical aspects of coupling shaped pulses into a fiber as well as the influence of linear and nonlinear effects on the pulse shape. Then in section 4.4 I briefly discuss transporting phase-, amplitude- and polarization-shaped pulses through the fiber in the pulse energy regime where nonlinear effects can be neglected and present some examples.

The results are presented in chapters 5, 6 and 7. First, in chapter 5 coherent control of two-photon processes with phase-shaped pulses transported through the fiber is demonstrated. It is shown that a certain class of spectral phase functions can be still used to efficiently and selectively excite two-photon transitions in spite of the distortions caused by the nonlinear effects. The presented measurements are accompanied by numerical simulations that explain the obtained results. Next, in chapter 6 the method of reverse propagation (also called backwards propagation), is described. The theoretical as well as technical aspects of the method are discussed and examples of shaped pulses obtained by it are presented. Finally, in the last chapter the pulse shaping methods described in chapters 5 and 6 are applied to a specific problem, that is selective two-photon excitation of molecules (in my case, laser dyes) in solution. The excitation efficiency and contrast obtained by both approaches are compared and their relative merits are discussed.

Fundamentals

2

In this chapter I will briefly introduce the fundamental physical laws governing the propagation of light in matter as well as equations that describe some particular situations that are relevant for this work.

2.1 Electromagnetic wave propagation

2.1.1 Wave equation

Light is an electromagnetic wave, so its propagation in a medium is governed by Maxwell's equations. If there are no free charges in the medium, Maxwell's equations can be used to obtain the wave equation [1]

$$\nabla \times \nabla \times \mathbf{E} = -\frac{1}{c^2} \frac{\partial^2 \mathbf{E}}{\partial t^2} - \mu_0 \frac{\partial^2 \mathbf{P}}{\partial t^2}, \quad (2.1.1)$$

where \mathbf{E} is the electric field vector and \mathbf{P} the induced electric polarization. \mathbf{P} is related to the electric flux density \mathbf{D} that appears in Maxwell's equations through the relation [1]

$$\mathbf{D} = \epsilon_0 \mathbf{E} + \mathbf{P}. \quad (2.1.2)$$

The speed of light c , the vacuum permittivity ϵ_0 and the vacuum permeability μ_0 are fundamental constants connected through the relation $\mu_0 \epsilon_0 = 1/c^2$. For a complete description, a relation between the induced polarization \mathbf{P} and the electric field \mathbf{E} is needed. In general, this requires a quantum-mechanical approach. However, if the frequency of the considered electric field is far enough from medium resonances, a phenomenological relation can be used [1]

$$\mathbf{P} = \epsilon_0 (\chi^{(1)} \cdot \mathbf{E} + \chi^{(2)} : \mathbf{E}\mathbf{E} + \chi^{(3)} \vdots \mathbf{E}\mathbf{E}\mathbf{E} + \dots) \quad (2.1.3)$$

where $\chi^{(j)}$ is j th order electric susceptibility of the medium. In general, $\chi^{(j)}$ is a tensor of rank $j + 1$ and so $:$ and \vdots are the double and triple inner products respectively. In anisotropic media the off-diagonal components of these tensors are not zero. As a result \mathbf{P} is not parallel to \mathbf{E} or in other words the medium is birefringent.

The polarization \mathbf{P} is often decomposed into a sum of two parts

$$\mathbf{P}(\mathbf{r}, t) = \mathbf{P}_L(\mathbf{r}, t) + \mathbf{P}_{NL}(\mathbf{r}, t), \quad (2.1.4)$$

where the linear part \mathbf{P}_L is the first term in eq. 2.1.3, linear in electric field \mathbf{E} , and the nonlinear part \mathbf{P}_{NL} is the sum of terms with $\chi^{(j)}$ for $j \geq 2$. If $\mathbf{P}_{NL} = 0$, eq. 2.1.1 becomes linear in the electric field and it is useful to write it in the frequency domain as [1]

$$\nabla \times \nabla \times \mathbf{E}(\mathbf{r}, \omega) = (1 + \tilde{\chi}^{(1)}(\omega)) \frac{\omega^2}{c^2} \tilde{\mathbf{E}}(\mathbf{r}, \omega), \quad (2.1.5)$$

where $\tilde{\mathbf{E}}(\mathbf{r}, \omega)$ is the Fourier transform of $\mathbf{E}(\mathbf{r}, t)$ defined as

$$\tilde{\mathbf{E}}(\mathbf{r}, \omega) = \int_{-\infty}^{\infty} \mathbf{E}(\mathbf{r}, t) \exp(i\omega t) dt \quad (2.1.6)$$

and $\tilde{\chi}^{(1)}(\omega)$ is the Fourier transform of $\chi^{(1)}$. The frequency-dependent dielectric constant $\epsilon(\omega)$ is then defined as

$$\epsilon(\omega) = 1 + \tilde{\chi}^{(1)}(\omega). \quad (2.1.7)$$

$\tilde{\chi}^{(1)}(\omega)$ is in general a complex function and its real and imaginary parts are related to the refractive index $n(\omega)$ and the absorption coefficient $\alpha(\omega)$ by the relations

$$n(\omega) = 1 + \frac{1}{2}\Re[\tilde{\chi}^{(1)}(\omega)], \quad (2.1.8)$$

$$\alpha(\omega) = \frac{\omega}{nc}\Im[\tilde{\chi}^{(1)}(\omega)]. \quad (2.1.9)$$

The frequency dependence of $n(\omega)$ is referred to as chromatic dispersion. On a fundamental level, its origin is related to the characteristic resonance frequencies at which the medium absorbs light.

In a lossless, homogeneous linear medium $n^2(\omega) = \epsilon(\omega)$ and eq. 2.1.5 takes the form of the Helmholtz equation

$$\nabla^2 \tilde{\mathbf{E}} + \beta^2(\omega) \tilde{\mathbf{E}} = 0. \quad (2.1.10)$$

where

$$\beta(\omega) = n(\omega) \frac{\omega}{c} \quad (2.1.11)$$

is the mode-propagation constant. If $\tilde{\mathbf{E}}$ describes a broadband light pulse instead of a monochromatic wave, it is useful to expand $\beta(\omega)$ in a Taylor series about the frequency ω_0 at which the pulse spectrum is centered:

$$\beta(\omega) = \beta_0 + \beta_1(\omega - \omega_0) + \frac{1}{2}\beta_2(\omega - \omega_0)^2 + \dots \quad (2.1.12)$$

The parameter β_1 is related to the group velocity v_g :

$$\beta_1 = \frac{1}{v_g}. \quad (2.1.13)$$

Group velocity is the velocity at which the envelope of an optical pulse is traveling in the medium. Parameter β_2 describes the frequency dependency of the group velocity, known as the group-velocity dispersion (GVD). For most transparent materials β_2 is positive in the visible spectral range, so $\beta_2 > 0$ is often called normal dispersion and $\beta_2 < 0$ anomalous dispersion. In the normal dispersion regime, high frequency (blue-shifted) components of an optical pulse travel slower than the low-frequency (red-shifted) components. In the anomalous dispersion regime the opposite is true. The coefficient β_3 is called third-order dispersion (TOD).

The rotation operator in eq. 2.1.5 on the preceding page was eliminated by using the identity $\nabla \times \nabla \times \mathbf{E} = \nabla(\nabla \cdot \mathbf{E}) + \nabla^2 \mathbf{E}$. The Maxwell equation $\nabla \cdot \mathbf{D} = 0$ implies $\nabla \cdot \mathbf{E} = 0$ only in a linear medium, but the latter is true also in nonlinear media for transverse, infinite plane waves and most of other cases of interest [2].

The electromagnetic field is fully described by two time- and position-dependent vectors, the electric field vector $\mathbf{E}(\mathbf{r}, t)$ and the magnetic field vector $\mathbf{H}(\mathbf{r}, t)$. In a three-dimensional space this corresponds to six components, but because $\mathbf{E}(\mathbf{r}, t)$ and $\mathbf{H}(\mathbf{r}, t)$ must satisfy Maxwell's equations, only two of the six components are independent. The wave equation for these two components can be then solved by separation of variables. In the following solving the wave equation for one of these components will be discussed.

Let's assume light propagating along z . It is convenient to express the electric field in the frequency domain in the form

$$\tilde{E}(\mathbf{r}, \omega) = F(x, y) \tilde{A}(z, \omega) \exp(i\beta_0 z). \quad (2.1.14)$$

where $\beta_0 \equiv \beta(\omega_0)$ and ω_0 is the carrier frequency. $F(x, y)$ describes the transverse field distribution and $\tilde{A}(z, \omega)$ the frequency-dependent propagation. It is assumed that $\tilde{A}(z, \omega)$ is a slowly varying function of z . This leads to the following two equations

$$\frac{\partial^2 F}{\partial x^2} + \frac{\partial^2 F}{\partial y^2} + \left[\epsilon(\omega) \frac{\omega^2}{c^2} - \tilde{\beta}^2 \right] F = 0, \quad (2.1.15)$$

$$2i\beta_0 \frac{\partial \tilde{A}}{\partial z} + (\tilde{\beta}^2 - \beta_0^2) \tilde{A} = 0. \quad (2.1.16)$$

The wave number $\tilde{\beta}$ has to be determined by solving eq. 2.1.15 [1].

A detailed discussion of solutions to eq. 2.1.15 is not relevant to my work. There are, however, two cases that I will consider in the following sections: Gaussian beams and fiber modes.

2.1.2 Gaussian beam

Gaussian beam is a solution of the Helmholtz equation that exhibits the characteristics of a typical laser beam. Most of its intensity is confined within a small cylindrical volume and is distributed symmetrically around the axis of this cylinder. At the same time, the beam propagates with minimal angular spread. The fact that the intensity distribution in the transverse plane is a Gaussian function makes it possible to derive analytical formulas describing its propagation, but at the same time it is a quite good approximation for actual laser beams. In cylindrical coordinates $\mathbf{r} = (\rho, \phi, z)$ the electric field amplitude of a Gaussian beam is given by [3]

$$E(\mathbf{r}) = E_0 \frac{w_0}{w(z)} \exp \left[\frac{-\rho^2}{w^2(z)} \right] \exp \left(-i\beta z - i\beta \frac{\rho^2}{2R(z)} + i\zeta(z) \right) \quad (2.1.17)$$

where

$$w(z) = w_0 \sqrt{1 + \left(\frac{z}{z_0} \right)^2} \quad (2.1.18)$$

$$R(z) = z \left[1 + \left(\frac{z_0}{z} \right)^2 \right] \quad (2.1.19)$$

$$\zeta(z) = \arctan \left(\frac{z}{z_0} \right) \quad (2.1.20)$$

$$z_0 = \frac{\pi w_0^2}{\lambda} \quad (2.1.21)$$

$w(z)$ and $R(z)$ are measures of the beam width and curvature, respectively. z is defined so that $z = 0$ corresponds to the beam waist, where the beam width is at its minimum ($w(z) = w_0$) and the wavefronts are almost planar ($|R| \rightarrow \infty$). About 86% of the beam intensity is contained within the radius $\rho = w(z)$, so $w(z)$ is regarded as the beam radius for practical purposes. z_0 is the Rayleigh range and is a measure of how well collimated the beam is.

Transmission of Gaussian beams through optical components such as lenses can be for many cases calculated analytically using the ABCD matrix formalism. In this formalism each optical

element, including free space, is described by a 2×2 matrix and the beam is represented by a vector. As an example, a matrix for a telescope consisting of two lenses is computed by multiplying in the right order the matrices of the lenses and of a free space region with thickness corresponding to the lenses distance. The ABCD matrices are useful in experimental work eg. for calculating what lenses to use in a telescope to obtain a given magnification.

2.1.3 Fiber modes

Conventional optical fibers guide light due to total internal reflection. This requires a core with a greater refractive index than that of the cladding. A fiber in which the refractive index is constant in both the core and the cladding and changes abruptly at the boundary is called step-index fiber. A function that describes the electric field of a mode propagating in the fiber core of a step-index fiber must satisfy the Helmholtz equation where $n = n_1$ in the core and $n = n_2$ in the cladding; the cladding radius is usually big enough that it can be assumed to be infinite. The number of solutions describing guided modes depends on the difference of the refractive indexes $n_1 - n_2$ and the core radius (larger core supports more modes). In general different modes have different group velocities which is undesirable. Moreover, uncontrollable imperfections and strain in actual fibers cause random phase shift between modes which leads to so called modal noise [3]. To avoid those effects I used a single-mode fiber in my work.

Chromatic dispersion in single-mode fibers has several sources: material dispersion, waveguide dispersion and nonlinear dispersion. Material dispersion, that is the dependence of the refractive index on wavelength, was already discussed in 2.1.1. In addition, a fiber mode is mostly confined to the core, but a part of it propagates in the cladding. The electromagnetic field distribution depends on the ratio between the wavelength and the core radius. This means that the relative portions of optical power in the core and the cladding change with wavelength, so the group velocity would depend on wavelength even if the material dispersion was negligible. This dependence is known as waveguide dispersion. If the refractive indexes of the core and the cladding are known, the waveguide influence can be calculated analytically [3].

Material and waveguide dispersion depend solely on the fiber parameters. Yet another effect occurs when the intensity of light is sufficiently high. The refractive index becomes intensity-dependent and the high-intensity parts of a pulse undergo different phase shift than the low-intensity parts. I will discuss the nonlinear effects in more detail in section 2.4.2.

2.2 Pulsed light

In the previous sections the transverse distribution of the electric field was considered. In this section I will discuss the frequency (or equivalently time) dependence and introduce the necessary formalism for describing ultrashort pulses. I will also discuss the effects of dispersion on the temporal shape of an ultrashort pulse. Finally, I will discuss the concept of pulse shaping and its applications, primarily coherent control.

2.2.1 Mathematical description of laser pulses

A laser pulse consists of many frequency components which have a defined phase relation. Since the pulse originates in a laser resonator, the components are the longitudinal modes of the laser cavity:

$$L = \frac{m\lambda}{2}, m \in N^+ \quad (2.2.1)$$

where L is the (optical) length of the laser cavity. For a typical laser cavity $L = 1.5$ m, so the frequency difference between two consecutive modes $\Delta\nu$ is 100 MHz. The ultrashort laser pulses that I will consider in my work have a bandwidth of the order of 10 THz, which means that they consist of 10^5 modes. Because of that the spectrum of an ultrashort pulse can be treated as continuous even though it is, strictly speaking, discrete[†]. The slowly varying envelope $\tilde{A}(z, \omega)$ introduced in eq. 2.1.14 on page 5 is then a continuous function.

Pulses emitted by many lasers can be approximated by a Gaussian shape

$$A(0, t) = A_0 \exp\left(-\frac{t^2}{2T_0^2}\right), \quad (2.2.2)$$

where T_0 is the half-width at $1/e$ -intensity point. In practice, the full width at half maximum (FWHM) is used. For a Gaussian pulse, the two are related by

$$\tau = 2\sqrt{(\ln 2)}T_0 \quad (2.2.3)$$

The spectral amplitude of such pulse is also described by a Gaussian function

$$\tilde{A}(0, \omega) = A_0 T_0 \sqrt{\frac{\pi}{2}} \exp\left(-\frac{\omega^2 2 \ln 2}{\Delta\omega^2}\right), \quad (2.2.4)$$

where $\Delta\omega$ is the FWHM of the pulse spectrum. The relation between the pulse duration and its spectral width can be obtained by Fourier transformation:

$$\tau\Delta\omega = 2 \ln 2. \quad (2.2.5)$$

When the pulse propagates in a dispersive medium, it acquires additional phase and the pulse duration changes. As an example, let us consider a linear medium which has only second-order dispersion (so the Taylor expansion of $\beta(\omega)$ given by eq. 2.1.12 on page 4 ends after three terms). After propagation by a distance z the pulse acquires quadratic spectral phase:

$$\tilde{A}(z, \omega) = \tilde{A}(0, \omega) \exp\left(\frac{i}{2}\beta_2\omega^2 z\right). \quad (2.2.6)$$

By inverse Fourier transformation one finds that the temporal envelope of the pulse remains a Gaussian function but the pulse duration increases:

$$T(z) = T_0 \sqrt{1 + \left(\frac{z}{L_D}\right)^2} \quad (2.2.7)$$

where the dispersion length $L_D = T_0^2/|\beta_2|$. For $z \gg L_D$ the pulse duration increases linearly with the propagation distance in the medium. Further, by taking a derivative of the temporal phase one finds that the instantaneous frequency of the pulse increases linearly with time. This means that a quadratic spectral phase corresponds to a linear frequency chirp. Similarly, a third-order spectral phase caused by TOD causes a quadratic frequency chirp. In addition, TOD changes the temporal shape of the pulse so that it becomes asymmetric.

Relation 2.2.5 holds for Gaussian pulses with a flat spectral phase. A similar relation of the form

$$\tau\Delta\omega \geq \text{const} \quad (2.2.8)$$

can be obtained for any pulse envelope shape. In general, the minimum pulse duration is inversely proportional to the spectral width. The pulse that reaches this limit is called a transform limited (TL) pulse.

[†]Another reason to treat the spectrum as continuous are the fluctuations of the carrier envelope phase that lead to shifting of the discrete frequencies in the spectrum.

2.2.2 Pulse shaping and coherent control

In the previous section I described how the spectral phase of a pulse changes during propagation in a dispersive medium. More generally, any modulation induced by a medium where the refractive index and absorption are frequency-dependent can be expressed as

$$\tilde{E}_{out}(\omega) = \tilde{H}(\omega)\tilde{E}_{in}(\omega) \quad (2.2.9)$$

where the modulation function $H(\omega)$ consists of an amplitude filter $R(\omega)$ and a phase filter $\Phi(\omega)$:

$$H(\omega) = R(\omega) \exp(i\Phi(\omega)). \quad (2.2.10)$$

The amplitude filter $R(\omega)$ is connected to the frequency-dependent transmission of the medium $T(\omega)$ by the following relation:

$$I_{out}(\omega) \propto \left| \tilde{E}_{out}(\omega) \right|^2 = R^2(\omega) \left| \tilde{E}_{in}(\omega) \right|^2 = T(\omega) \left| \tilde{E}_{in}(\omega) \right|^2 \propto T(\omega) I_{in}(\omega). \quad (2.2.11)$$

In many experiments with ultrashort pulses TL pulses are preferred. If a spectral modulation is applied to the pulse, its only aim is compensating for the dispersion and other effects that elongate the pulse. However, a number of fields such as coherent control [4, 5], multidimensional spectroscopy [6], biological imaging [7] and many others (see for example the references in [8]) benefit from arbitrarily shaped optical waveforms. Here I want to discuss the one that has the longest tradition and is probably the broadest, namely coherent control. Application of shaped pulses to biological imaging will be discussed in chapter 7.

The field of coherent control stems from the works of Brumer and Shapiro [9] and of Tannor, Kosloff and Rice [10, 11]. In 1980s the authors proposed two different schemes for controlling electronic transitions with coherent light. Although both schemes have been successfully applied to simple molecules, they share a weakness: both use only one parameter for control, in the first case the phase between two laser beams, in the other case the time delay between two pulses. But real quantum systems are usually too complex to be controlled with a single parameter.

The general problem of controlling the path to a specified final state of a quantum-mechanical system by driving the wavepacket with an optimal electric field is treated in the optimal control theory (OCT) [12]. A practical way to find such an optimal field was proposed by Judson and Rabitz [13]. Their idea was to optimize the electric field in a closed loop by generating a shaped laser pulse and then using an appropriate observable as a fitness function for an optimization algorithm. The pulse shape is gradually adapted to yield maximum fitness and so in the end the algorithm converges to a solution without having any prior knowledge of the system itself. This method was successfully applied in many experiments for various systems, including complex biomolecules (see for example the review papers [4, 5]). This was made possible, among other things, by the advances in pulse shaping [14].

The scheme of Judson and Rabitz requires arbitrarily shaped pulses. In experiment a temporal modulation of femtosecond laser pulses is not feasible, because no electronic devices operating on a femtosecond timescale are available, so the pulse spectrum has to be modulated instead. One way of generating a modulation in the spectral domain is placing an optical element made of an appropriate material in the beam. Some transmission filters made of colored glass use this principle. However, it is not so easy to engineer dispersion. Instead, in most practical realizations the pulse spectrum is spatially separated by a dispersive element such as a diffraction grating. After doing that one has several possibilities.

In a grating compressor different wavelengths are sent along optical paths of different length. By combining diffraction gratings with mirrors or imaging elements, both positive and negative

linear chirp can be introduced. In addition in some versions of the grating compressor quadratic chirp can be introduced by tuning the grating angle.

In a prism compressor different optical paths in air are combined with different optical paths in the second prism. Variable linear chirp can be introduced by changing the prism distance and position of the second prism, but the quadratic chirp that results from the material dispersion of the prisms cannot be varied independently from linear chirp.

Finally, a typical pulse shaper consists of a zero-dispersion compressor - that is, a grating or prisms configuration that introduces no dispersion on its own - and a spatial light modulator (SLM) placed in the Fourier plane, that is the plane where the spectral components are maximally separated in space. The SLM can be a fixed mask, but it is much more convenient to use a programmable device where the position-dependent phase and transmission can be controlled by a computer. This will be described in detail in section 3.2 on page 22.

A pulse shaper controls the phase and amplitude of individual spectral components. Mathematically, any modulation in the spectral domain corresponds to a modulation in the temporal domain which yields the same result. In some cases it is convenient to incorporate the Fourier transform in the algorithm controlling the shaper and look for the solution in the temporal domain even though physically the modulation is applied in the spectral domain. However, in both cases the result of optimizing hundreds of independent parameters will be difficult to interpret. Moreover, an actual experiment is noisy and usually limited in time by some technical factors, so an optimization with too many parameters will simply not converge fast enough.

Several solutions have been proposed to solve these problems. The one that is most often employed is reducing the dimensionality of the search space. The simplest example of such restrictions is merging of pixels [15] or allowing a limited number of voltage values, like in binary phase shaping [16]. Another possibility is parametrization of the spectral phase by expressing it as a polynomial function or a periodic function [15].

A parametrization that is particularly suitable for controlling processes consisting of a few distinct steps, such as the pump-dump scheme of Tannor, Kosloff and Rice [11], is expressing the electric field as a sum of several subpulses in the time domain [15, 17]. Experimentally this can be seen as an extension of pump-probe scheme, where the pulse is split by a beam splitter and one of the copies is delayed by a mechanical delay stage. The advantages of using a pulse shaper instead are no need to search for the spatial overlap and easiness to control the parameters of subpulses or generating more than two subpulses without using additional optical elements. The method proposed by Hornung et al. [17] has been extended to manipulate the intensity, phase, position in time and chirp of the pulse and in this form applied to control of multiphoton ionization of NaK [18]. Later, restricted [19] and finally also full [20] polarization control of subpulses was implemented as well.

2.3 Second-order nonlinear processes

In this section I will discuss second-order nonlinear effects. I will concentrate on second-harmonic generation in a nonlinear crystal and two-photon absorption of ultrashort pulses.

2.3.1 Second-harmonic generation

Linear optical properties of nonmetallic solids are very well described by the Lorentz model of the atom. In this model the atom is treated as a harmonic oscillator. The model can be extended to nonlinear optics by allowing the possibility of a nonlinear restoring force exerted on the electron.

A limitation of this approach is that it assumes only one resonant frequency while in fact all atoms have multiple resonant frequencies. However, the classical model provides a good description as long as all the optical frequencies taken into consideration are smaller than the lowest electronic resonance frequency of the material system. If this is not the case, a quantum-mechanical model has to be used [2].

Using the extended Lorentz model it can be derived that the second-order nonlinear susceptibility $\chi^{(2)}$ is nonvanishing only in a noncentrosymmetric medium. The absence of central symmetry leads to nonvanishing terms with an odd power of the spatial coordinate in the potential energy of the electron. The differential equation describing the electron motion can be then solved by means of a perturbation expansion as long as the applied field is sufficiently weak. The lowest contribution to the equation is then the same as the equation resulting from the linear Lorentz model. From the next term, the lowest order correction, the nonlinear induced polarization vector is obtained [2]

$$P_{NL,i}(\omega_n + \omega_m) = \sum_{jk} \sum_{(nm)} \chi_{ijk}^{(2)}(\omega_n + \omega_m; \omega_n, \omega_m) E_j(\omega_n) E_k(\omega_m). \quad (2.3.1)$$

The indices ijk denote the cartesian components of the fields. In general, in a second-order processes two photons of frequencies ω_1 and ω_2 are destroyed and a photon of frequency ω_3 is simultaneously created in a single quantum-mechanical process. By looking at eq. 2.3.1 it would seem that to describe the mutual interaction of three waves of frequencies ω_1 , ω_2 and $\omega_3 = \omega_1 + \omega_2$ one would need 12 tensors corresponding to the permutations of these frequencies and their negatives (for example $\chi_{ijk}^{(2)}(\omega_1; -\omega_2, \omega_3)$, $\chi_{ijk}^{(2)}(\omega_1; \omega_3, -\omega_2)$ and so on). Each tensor has 27 coordinates, so in total 324 complex numbers would be needed. Fortunately, there are a number of restrictions resulting from symmetries and thus far fewer number are sufficient [2].

Theoretically, several different second-order processes can happen at the same time: second-harmonic generation (SHG) of each of the input fields, sum-frequency generation (SFG), difference-frequency generation (DFG) and optical rectification (OR). However, usually only one of them is efficient. The reason for this is phase-matching. In short, the electromagnetic waves generated by the atoms along the whole propagation distance must interfere constructively for the signal to be generated efficiently. This requires that the wavevector mismatch

$$\Delta k = k_1 + k_2 - k_3 \quad (2.3.2)$$

is equal to zero, which for collinear beams means

$$n_1\omega_1 + n_2\omega_2 = n_3\omega_3. \quad (2.3.3)$$

For the case of second-harmonic generation, where $\omega_1 = \omega_2$ this requires that

$$n(\omega_1) = n(2\omega_1) \quad (2.3.4)$$

which is not possible for most materials that exhibit normal dispersion and thus $n(\omega)$ increases monotonically with ω . A similar argument can be made in the case of sum-frequency generation.

There are several methods of circumventing this problem in order to achieve phase-matching in spite of the normal dispersion. A common one is to use a birefringent crystal where the refractive index depends on the light polarization. The crystal should be oriented so that the lower frequency component propagates along the axis with higher refractive index and the difference between the refractive indices for the two polarizations counterbalances the difference due to chromatic dispersion. An appropriate choice of the crystal angle and the orientation of the input field allows perfect phase matching for a certain fundamental frequency ω_1 and its second harmonic. For SFG

there are two possibilities to realize this kind of phase matching: type I phase matching, where the two lower-frequency waves have the same polarization and the sum frequency polarization is perpendicular with respect to it, and type II where the two input beams are orthogonal. For SHG type I phase matching is required. In the following it will be assumed that this is the case and that the considered second-harmonic field is perpendicular to the fundamental frequency field. For simplicity, the cartesian indices will be omitted.

It should be noted that phase matching by tuning the crystal angle has one serious drawback. For most crystal orientations the Poynting vector (representing the direction of energy flux) is not parallel to the propagation vector which causes a divergence between the ordinary and extraordinary rays, in this case - fundamental and second harmonic. This walkoff effect limits the spatial overlap and decreases the efficiency of the nonlinear mixing process. An alternative to that is temperature tuning which is possible in crystals where birefringence depends strongly on temperature.

For monochromatic radiation the process of second-harmonic generation can have almost 100% efficiency; this is routinely used in many CW lasers, for example for doubling the near infrared output of a Nd:YAG laser. However, in the case of broadband ultrashort pulses it is usually not possible to have phase matching for the whole spectrum. Moreover, in this case it is not strictly correct to talk about second-harmonic generation, because what actually takes place is sum-frequency generation between all the frequency pairs in the pulse. Nevertheless it is customary to call the process SHG to distinguish it from the SFG of two distinct femtosecond pulses with different central wavelengths or propagation directions.

In the regime where the SHG efficiency is small and the depletion of the fundamental beam can be neglected, the second harmonic field in the frequency domain is given by [21]

$$\tilde{E}_{SH}(2\omega) = \int_{-\infty}^{\infty} \tilde{E}(\omega + \Omega) \tilde{E}(\omega - \Omega) d\Omega \times D(2\omega), \quad (2.3.5)$$

where \tilde{E} is the complex electric field that can be decomposed into its real positive magnitude $|E(\omega)|$ and phase $\Phi(\omega)$: $\tilde{E}(\omega) = |E(\omega)| \exp(i\Phi(\omega))$. $D(\omega)$ describes the phase-matching. Assuming that a perfect phase-matching is achieved at a frequency ω_0 , the phase-matching factor for a given frequency ω is equal to

$$D(\omega) = \Gamma L \operatorname{sinc} \left(\frac{1}{2} \alpha L (\omega_0 - \omega) \right), \quad (2.3.6)$$

where Γ is a constant describing the nonlinear coupling efficiency proportional to $\chi^{(2)}$, L is the crystal length and $\alpha = 1/v_{g1} - 1/v_{g3}$ is the group-velocity mismatch between the fundamental and doubled waves. One has to keep in mind that even when the group velocities are matched, for broadband pulses and long propagation distances the next term, the GVD, can become significant.

To estimate the influence of phase matching on the SHG spectrum it is convenient to introduce the interaction length given by $L_i = \tau/|\alpha|$, where τ is the duration of a transform limited fundamental pulse. Let us consider the two limits, the thick crystal regime where $L \gg L_i$ and the thin crystal regime where $L \ll L_i$. In the first case $D(\omega)$ is very narrow and can be approximated by $\delta(\omega - \omega_0)$. The SHG spectrum is limited by the spectral filtering due to phase matching. The power of the quasi-monochromatic second harmonic is then

$$P_{SH}^{thick} \propto \left| \int_{-\infty}^{\infty} |E(\omega_0 + \Omega)| |E(\omega_0 - \Omega)| \times \exp \{i [\Phi(\omega_0 + \Omega) + \Phi(\omega_0 - \Omega)]\} d\Omega \right|^2. \quad (2.3.7)$$

The second harmonic field at a frequency $2\omega_0$ results from summing up all frequency pairs in the fundamental beam fulfilling the energy conservation condition $2\omega_0 = \omega_i + \omega_j$. The value of the

integral depends on the spectral phase of the input pulse. One can use this property to achieve coherent control of the process by shaping the spectral phase of the input pulse [21]. I will discuss this in more detail in section 2.3.3.

In the other limit, the thin crystal regime, $D(\omega)$ can be approximated by a constant value over the whole input pulse spectrum and the width of the second harmonic spectrum is limited only by the spectrum of the input pulse. The power of the second harmonic can be written as:

$$P_{SH}^{thin} \propto \int_{-\infty}^{\infty} \left| \int_{-\infty}^{\infty} \tilde{E}(\omega + \Omega) \tilde{E}(\omega - \Omega) d\Omega \right|^2 d\omega, \quad (2.3.8)$$

or by taking a Fourier transform and using the convolution theorem

$$P_{SH}^{thin} \propto \int_{-\infty}^{\infty} I^2(t) dt, \quad (2.3.9)$$

where $I(t)$ is the intensity of the fundamental beam. This integral is maximized by the TL pulse. This has been noted and applied to pulse compression. In 1997 two groups [22, 23] demonstrated the use of a pulse shaper combined with an adaptive algorithm with second harmonic (SH) intensity as the feedback signal for minimizing the pulse duration. Many other similar experiments have followed (see e.g. references in [24]).

In the above I considered SHG in bulk noncentrosymmetric crystals. Another situation where second-order nonlinear processes can take place is an interface between two different centrosymmetric nonlinear optical materials. Even though they have no second-order nonlinear optical susceptibility in bulk, in the thin (of the order of one molecular diameter thickness) region near the interface the symmetry is broken, and this layer can emit a second-harmonic wave [2]. In bio-imaging SHG is used to discern the orientation of noncentrosymmetric second-harmonic generating structures such as collagen type I, skeletal muscles, and microtubules [25, 26].

2.3.2 Two-photon absorption

Another class of nonlinear processes are processes where light causes transitions in atoms or molecules in spite of the lack of a one-photon resonance, such as two-photon absorption (TPA). The extended Lorentz model cannot be applied for TPA, because the condition that all resonant states are far away is not fulfilled. On the contrary, I want to consider a situation where the second harmonic of the electromagnetic field coincides with a resonance. In particular, I will consider nonresonant two-photon (TP) transitions, that is transitions with no intermediate state.

Let us consider a weak ultrashort pulse interacting with a two-level system. E_g and E_f are energies of the ground and excited states, respectively, so the resonance frequency is $\omega_r = (E_f - E_g)/\hbar$. The system is initially in the ground state and the electric field of the excitation pulse $E(t)$ is much shorter than the lifetime of the excited state. First-order time-dependent perturbation theory predicts the following amplitude of the excited state [27]

$$a_{1P}(t) = \frac{\mu_{fg}}{i\hbar} \int_{-\infty}^t E(t') \exp(i\omega_r t') dt', \quad (2.3.10)$$

where μ_{fg} is the dipole matrix element. If we consider a time t after the excitation pulse has ended, this integral is simply the Fourier component of the optical field which is at resonance with the transition. Therefore the one-photon transition probability to the excited state depends only on the energy content of this frequency component. The phases and amplitudes of all the other components do not affect the transition probability.

If the pulse is not resonant with any one-photon transition, it may still induce a two-photon transitions. Second-order time-dependent perturbation theory gives

$$a_{2P}(t) = \frac{1}{\hbar^2} \sum_n \mu_{fn} \mu_{ng} \int_{-\infty}^t \int_{-\infty}^{t'} E(t') E(t'') \exp(i\omega_{fn} t') \exp(i\omega_{ng} t'') dt'' dt', \quad (2.3.11)$$

where $\hbar\omega_{ij} = E_i - E_j$ and the summation is performed over all possible intermediate states. To perform this summation one has to note that the intermediate levels are far from resonance and as a consequence they add coherently only for a very short time so that one can use the approximation

$$\sum_n \mu_{fn} \mu_{ng} \exp\left[\frac{iE_n(t'' - t')}{\hbar}\right] = \begin{cases} \langle f | \mu^2 | g \rangle, & |t' - t''| < \bar{\omega}^{-1} \\ 0, & |t' - t''| \geq \bar{\omega}^{-1}, \end{cases} \quad (2.3.12)$$

where $\hbar\bar{\omega}$ is the weighted average energy (see [27]). This simplifies the double integration in 2.3.11 and one obtains the TP transition probability to the excited state following the pulse excitation

$$S_{2P} = \frac{1}{\hbar^4} \left| \frac{\langle f | \mu^2 | g \rangle}{\bar{\omega}} \right|^2 \left| \int_{-\infty}^{\infty} E^2(t) \exp(i\omega_r t) dt \right|^2. \quad (2.3.13)$$

The two-photon transition probability depends on the spectral component of $E^2(t)$ resonant with the transition.

It turns out that a similar relation holds also for higher-order processes. If transitions of order lower than N are nonresonant, the probability for an N -photon transition is proportional to the resonant Fourier component of $E^N(t)$:

$$S_{NP} \propto \left| \int_{-\infty}^{\infty} E^N(t) \exp(i\omega_r t) dt \right|^2. \quad (2.3.14)$$

What remains to be done is rewriting the expression 2.3.13 in the frequency domain. This can be done by applying the convolution theorem from which follows that the Fourier transform of a function squared is equal to the convolution of this function with itself:

$$S_{2P} \propto \left| \int_{-\infty}^{\infty} \tilde{E}(\omega + \Omega) \tilde{E}(\omega - \Omega) d\Omega \right|^2, \quad (2.3.15)$$

where $\omega = \omega_r/2$. This expression is very similar to eq. 2.3.5 on page 11, describing second-harmonic generation in a thick crystal. This is actually not surprising, but merely confirms the validity of the Lorentz model. A quantum mechanical derivation of SHG generation is analogical to the derivation for TPA presented here.

I have shown above that the efficiency of the two processes, SHG and TPA, is described by the same expression and that it depends on the spectral amplitude and phase of the input pulse. Consequently both processes can be controlled by manipulating the spectral phase of the pulse which I will discuss in the next section.

2.3.3 Coherent control of two-photon processes

For a pulse with electric field spectrum described by $E(\omega) = |E(\omega)| \exp[i\Phi(\omega)]$ it is convenient to introduce the second-order spectrum at a frequency 2ω :

$$\tilde{E}^{(2)}(2\omega) = \int_{-\infty}^{\infty} |E(\omega + \Omega)| |E(\omega - \Omega)| \times \exp\{i[\Phi(\omega + \Omega) + \Phi(\omega - \Omega)]\} d\Omega, \quad (2.3.16)$$

As shown in the previous section, the second-order spectrum as defined above is actually the effective field driving a narrow two-photon transition at the frequency 2ω . Now the probability of any TP transition can be written as

$$S_{2P} \propto \int_{-\infty}^{\infty} g(\omega) |E^{(2)}(\omega)|^2 d\omega, \quad (2.3.17)$$

where $g(\omega)$ corresponds to the phase-matching function for SHG or the line-shape function for TPA.

It is easy to verify that this probability is maximized, for a given pulse energy and power spectrum $|E(\omega)|^2$, by the transform limited pulse, i.e. the pulse with $\Phi(\Omega) = 0$. This is generally true for most nonlinear processes: a nonlinear effect is maximized by a pulse with the highest peak power, that is the shortest duration. However, in this particular case another nontrivial solution exists. Let us consider a pulse with an antisymmetric phase distribution around a certain frequency ω_0 , i.e. a phase that satisfies the condition

$$\Phi(\omega_0 + \Omega) = -\Phi(\omega_0 - \Omega) \quad (2.3.18)$$

for all Ω . In this case, the phase terms in eq. 2.3.16 cancel each other for $\omega = \omega_0$ so that at this frequency the TP transition probability is identical with that of a TL pulse. This result is somewhat counterintuitive, as the pulse with an antisymmetric phase can be significantly spread in time so that it has much lower peak intensity than the TL pulse. A side effect is that the phase can be tailored to eliminate or at least reduce other multiphoton transitions [27].

Although resonant two-photon transitions are beyond the scope of this work, it is worth mentioning that for such transitions the transition probability for some phase-shaped pulses can be significantly higher than for TL pulses [28]. An intermediate level plays a role in the excitation even if it does not exactly coincide with the pulse central frequency. The reason for that is the uncertainty principle: because the system spends only a very short time in the intermediate state, the energy of this state is broadened which allows for some detuning between the exciting photons and the resonance frequency. As a result, the expression 2.3.11 changes. One difference is that photons with energy smaller and larger than the energy difference between the ground state and the intermediate state contribute to the total transition probability amplitude with different signs, so they interfere destructively if no phase shaping is applied. Experimental examples, supported by theoretical calculations, showing how pulse shaping can lead to an increase of the transition probability for transitions with an intermediate state can be found in [28].

Controlling nonresonant two-photon transitions with pulses with antisymmetric spectral phase is an important part of this work, so I will now discuss it in more detail. First I will consider a particularly simple spectral phase, namely a π spectral phase step:

$$\Phi = \frac{\pi}{2} \text{sgn}(\Omega - \omega_0). \quad (2.3.19)$$

Figure 2.1 shows calculated two-photon spectra for a Gaussian pulse with a π step phase for different positions of the π step. The first thing to note is that the amplitude of the TP spectrum of the shaped pulse at the position of the π step is the same as the amplitude of the TL pulse at this frequency. Secondly, for all positions of the π step there is a frequency at which the amplitude of the TP spectrum of the shaped pulse is equal to zero.

The effects of a spectral phase of this form on TPA were investigated by Meshulach and Silberberg [27] who confirmed that the absorption efficiency behaves as predicted both for a narrow transition (atomic gas of cesium atoms) and a broad transition (laser dye Coumarin 6H). Later it

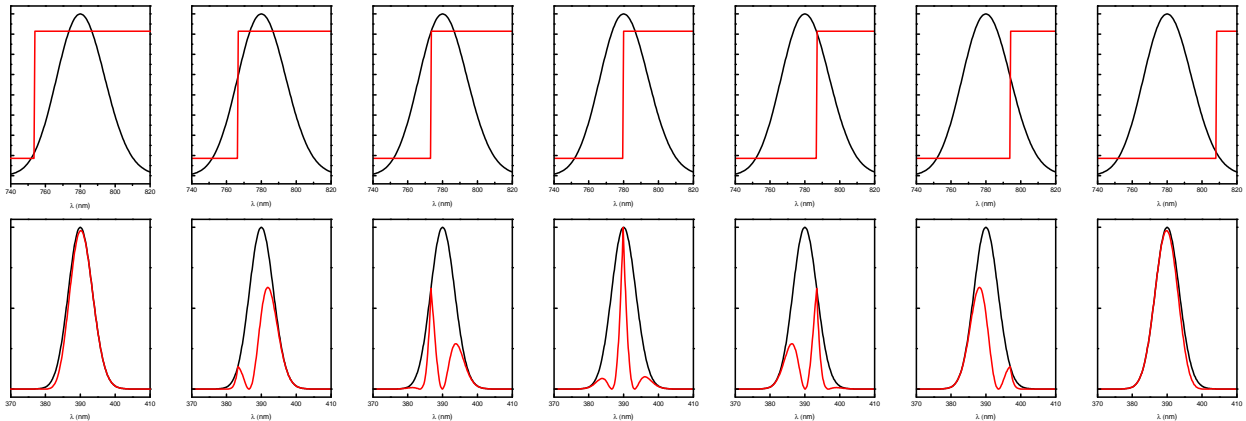


Figure 2.1: Effect of a π -step spectral phase on the second-order spectrum. The first row shows the first order spectrum of the pulse (black) and the phase function (red). The second row shows the second-order spectrum of the shaped pulse (red) and of the TL pulse with the same spectral amplitude (black).

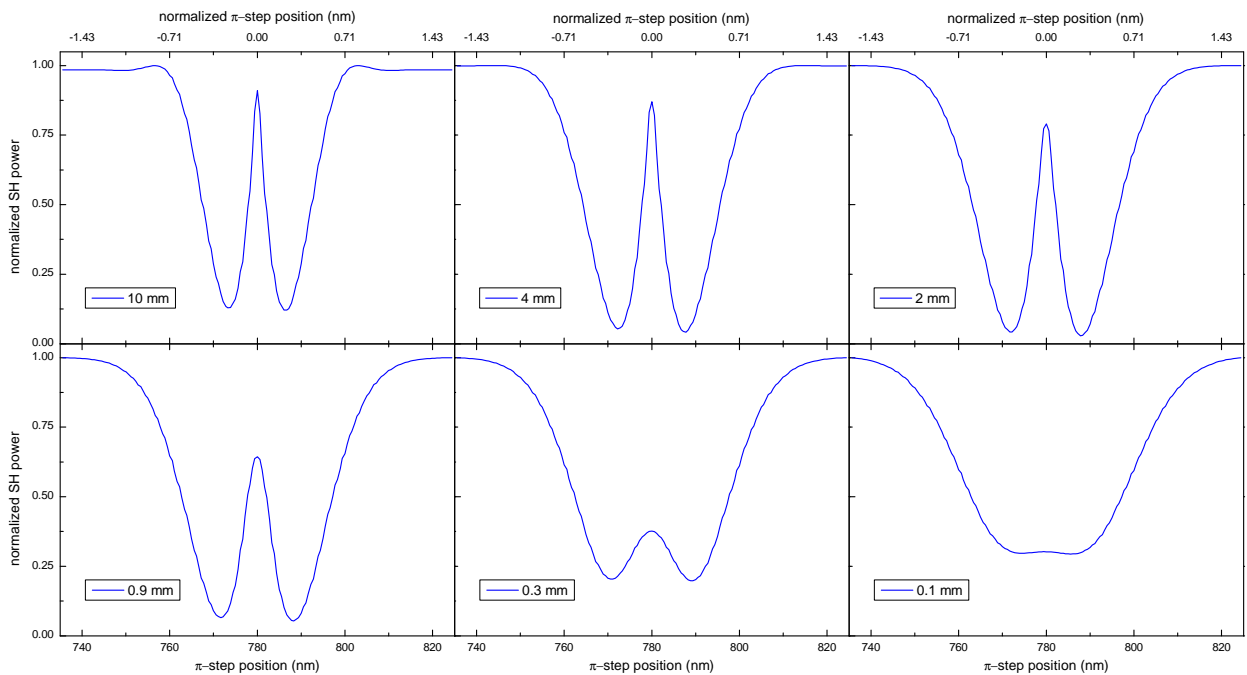


Figure 2.2: Simulation of normalized second harmonic signal generated in a BBO crystal for different crystal thickness. The crystal angle is chosen so that the phase matching maximum coincides with the central wavelength of the pulse. The lower axis shows the absolute position of the π step and the upper axis the position relative to the central wavelength in units of the spectral width of the pulse (28 nm).

has been shown experimentally that the SHG process is an analogue of TPA and that by changing the crystal thickness one can vary the transition width. This way one can not only study the coherent control of both limits - narrow and broad transitions - but also in the intermediate regime without using a different system and different experimental setup (a gas cell, a dye cell etc.) for each case [21]. To illustrate this, fig. 2.2 shows normalized second harmonic signal generated by pulses with a π step spectral phase for different crystal thickness. The crystal angle is chosen to achieve phase matching for the central wavelength of the pulse. The signal is one if the π step is far away from the central wavelength and starts dropping at the distance of about one spectral width. For the thick crystal the signal goes almost to zero, but then it increases again and there is a sharp peak at the central wavelength (the values of 0 and 1 are not reached because of the finite crystal thickness). With decreasing crystal thickness the transition width increases and the effect of the constructive interference is less and less visible. Finally, for a thin crystal the π step has no influence apart from decreasing the signal.

In both cases, SHG as well as TPA, it has been observed that for narrow transitions there were pulses of similar temporal shape, but significantly different TP efficiencies, as predicted by the simulation in fig. 2.1. If the π step position ω_0 is shifted from the transition frequency by a certain amount, no net absorption takes place. Such dark pulses are analogous to dark states, which are coherent superpositions of quantum states that do not absorb resonant light [27]. The fact that such a dark pulse always exists means that there is a potential for selective excitation of two-photon transitions. Moreover, Panek and Becker [29] have shown, both numerically and experimentally, that a dark pulse can be found also for a resonant two-photon transitions if a generalized form of the phase described by eq. 2.3.19 is used, with the step amplitude different from π .

Obviously, a π step phase is not the only function that satisfies eq. 2.3.18. Any antisymmetric function can be used as long as its complexity is not too large to be realized experimentally. The first demonstration of coherent control of a two-photon transition by phase shaping was done using a sinusoidal phase with varying phase and amplitude [30]. Sinusoidal phase was also applied to attain selective excitation in nonlinear microscopy [31, 32]. Lozovoy *et al* analyzed different spectral phases to determine which is most suitable to distinguish between competing two and three photon transitions [33].

2.4 Nonlinear effects in an optical fiber

2.4.1 Third-order nonlinear processes

Section 2.3.1 dealt with second-order nonlinear processes that are a consequence of second-order nonlinear polarization:

$$P^{(2)}(t) = \epsilon_0 \chi^{(2)} E(t)^2. \quad (2.4.1)$$

For the simplest case of a monochromatic wave $\tilde{E}(t) = E_0 \cos \omega t$ the second order polarization has the form

$$P^{(2)} = \frac{1}{2} \epsilon_0 \chi^{(2)} E_0^2 (1 + \cos 2\omega t). \quad (2.4.2)$$

The first term in this expression does not lead to generation of electromagnetic radiation, but only to a static electric field in the medium, known as optical rectification [2]. The second term describes the SHG. Other second-order processes that can take place in the more general case of a polychromatic wave also involve creation of new frequencies.

If the medium has inversion symmetry on the molecular level, the lowest order non-vanishing nonlinear susceptibility is $\chi^{(3)}$. Again, the third-order nonlinear susceptibility $\chi^{(3)}$ can be derived

by perturbation expansion using the extended Lorentz model, this time with a symmetric potential energy. Contrary to $\chi^{(2)}$, $\chi^{(3)}$ is never zero, so for a sufficiently large peak intensity third order nonlinear effects can be observed in any medium including liquids and gases.

The third-order contribution to the nonlinear polarization has the form

$$P^{(3)}(t) = \epsilon_0 \chi^{(3)} E(t)^3. \quad (2.4.3)$$

By substituting a monochromatic wave and using trigonometric identities one obtains [2]

$$P^{(3)}(t) = \frac{1}{4} \epsilon_0 \chi^{(3)} E_0^3 (\cos 3\omega t + 3 \cos \omega t). \quad (2.4.4)$$

The two terms are responsible for different physical processes. The first term again describes frequency conversion, in this case third-harmonic generation (THG). Analogically to SHG, during THG three photons are destroyed and one of a three times greater energy is created. Also here phase matching is required for the process to be efficient.

Here I want to concentrate on the second term in eq. 2.4.4. This term has the same frequency as the input field and can be described as a nonlinear contribution to the refractive index experienced by the propagating wave. The refractive index is then

$$n = n_0 + n_2 I, \quad (2.4.5)$$

where n_0 is the linear refractive index, n_2 the nonlinear refractive index proportional to $\chi^{(3)}$ and I light intensity. It should be noted $\chi^{(3)}$ is a fourth-rank tensor which can lead to processes that affect the polarization of the light, such as nonlinear birefringence. However, if the optical field is linearly polarized, only one component $\chi_{xxxx}^{(3)}$ of the tensor contributes to the refractive index.

If n_2 is positive, one of its consequences is self-focusing. This process has a great practical importance. On one hand, it can lead to damage as the beam reaches high intensity at the focal spot. On the other hand, it enables so-called Kerr lens modelocking which is commonly used in solid state oscillators to generate ultrashort pulses (more about that in sec. 3.1.1). Under proper conditions self-focusing can also counteract diffraction and lead to appearance of filaments.

In the case of an optical pulse the light intensity varies not only in the transverse plane, but also in time. This means that in presence of third-order nonlinearity the pulse tails experience a different refractive index than the pulse peak and the pulse phase changes in a way that depends on its intensity. This effect is known as self-phase modulation (SPM) and is the dominating nonlinear effect in optical fibers. I will discuss it in more detail in the next section.

2.4.2 Nonlinear Schrödinger equation

In section 2.1.1 equation 2.1.16, that is the propagation equation for the slowly varying envelope of a pulse, was introduced. To include nonlinear effects in this description, one can assume that $\tilde{\beta}$ now consists of a linear part $\beta(\omega)$ and a smaller nonlinear part $\Delta\beta(\omega)$. The difference $\tilde{\beta}^2 - \beta_0^2$ can be approximated by $2\beta_0(\tilde{\beta} - \beta_0)$ and now eq. 2.1.16 takes the form [1]

$$\frac{\partial \tilde{A}}{\partial z} = i [\beta(\omega) + \Delta\beta(\omega) - \beta_0] \tilde{A}. \quad (2.4.6)$$

Both $\beta(\omega)$ and $\Delta\beta(\omega)$ can be expanded in Taylor series (see eq. 2.1.12 on page 4). The number of terms in the expansion of $\beta(\omega)$ depends on the pulse bandwidth and properties of the medium. For example, if the central wavelength of the pulse is close enough to the zero-dispersion

wavelength of the medium, β_3 is the dominating term and has to be included even if the pulse spectrum is relatively narrow. I will include β_3 in the following because it turned out to have a non-negligible influence on the pulse shape in most of the experiments presented in this thesis.

As for the nonlinear part, in the first order approximation it can be assumed that it is not frequency-dependent so that $\Delta\beta \approx \Delta\beta_0$. This term includes the effects of fiber loss denoted by α and nonlinearity. After taking the inverse Fourier transform we obtain the equation [1]

$$\frac{\partial A}{\partial z} + \beta_1 \frac{\partial A}{\partial t} + \frac{i\beta_2}{2} \frac{\partial^2 A}{\partial t^2} - \frac{\beta_3}{6} \frac{\partial^3 A}{\partial t^3} + \frac{\alpha}{2} A = i\gamma(\omega_0)|A|^2 A, \quad (2.4.7)$$

where $|A|^2$ represents the optical power and the nonlinear parameter γ is defined as [1]

$$\gamma(\omega_0) = \frac{n_2(\omega_0)\omega_0}{cA_{eff}}. \quad (2.4.8)$$

A_{eff} is the effective mode area that can be calculated from the modal distribution $F(x, y)$ obtained by solving eq. 2.1.15 on page 5. For a Gaussian distribution (see eq. 2.1.17) $A_{eff} = \pi w^2$.

In the special case of $\alpha = 0$, eq. 2.4.7 is referred to as the nonlinear Schrödinger equation (NLSE) because it resembles the Schrödinger equation with a nonlinear potential term (here the variable z plays the role of time). It is a fundamental equation of nonlinear science and has been studied extensively. Generally it cannot be solved analytically except for some specific cases, so a numerical approach is required. In section 2.4.5 I will describe briefly the most often used method, that is the split-step Fourier method.

2.4.3 Consequences of self-phase modulation

Before attempting to solve the NLSE it is useful to get an idea about the importance of the linear and nonlinear effects in the considered case. This can be done by introducing two length scales, known as the dispersion length L_D and the nonlinear length L_{NL} :

$$L_D = \frac{T_0^2}{|\beta_2|}, \quad (2.4.9)$$

$$L_{NL} = \frac{1}{\gamma P_0}, \quad (2.4.10)$$

where T_0 is the pulse duration and P_0 the peak power. The effects become significant if the respective length scale is comparable to the fiber length L . If $L_D \ll L_{NL}$, the nonlinear effects can be neglected and if $L_D \gg L_{NL}$ they dominate. Finally, if both length scales are comparable and not longer than the fiber length, then dispersion and nonlinearity act together, which can lead to a qualitatively different behavior than that expected from GVD or SPM alone. For example, in the anomalous dispersion regime the fiber can support solitons because both kinds of effects counteract each other.

To understand what happens to the spectrum of a pulse due to SPM, let's first consider propagation along a short distance l . Due to the nonlinear contribution to the refractive index (eq. 2.4.5 on the previous page) there is also a nonlinear contribution to the temporal phase of the pulse [2]:

$$\Phi_{NL}(t) = -n_2 I(t) \omega_0 \frac{l}{c}. \quad (2.4.11)$$

The spectrum of the pulse can be now obtained by the Fourier transform. However, it is more intuitive to introduce the instantaneous frequency of the pulse

$$\omega(t) = \omega_0 + \delta\omega(t) \quad (2.4.12)$$

where

$$\delta\omega(t) = \frac{d\Phi_{NL}(t)}{dt}. \quad (2.4.13)$$

By substituting expression 2.4.11 we obtain the time-dependent frequency shift

$$\delta\omega(t) = -n_2\omega_0 \frac{l}{c} \frac{dI(t)}{dt}. \quad (2.4.14)$$

As a consequence, for a positive n_2 the leading edge of the pulse is shifted to lower frequencies and the trailing edge is shifted to higher frequencies. In the normal dispersion regime this leads to a broadening of a short pulse. Because of the GVD the low-frequency components of the pulse spectrum propagate faster, so they become the leading edge of the pulse, where they become further downconverted due to SPM. At the same time the high frequencies that stay at the trailing edge lead to generation of new higher frequencies. However, if the pulse has a negative frequency chirp, that is the instantaneous frequency decreases with time, the opposite happens. The higher frequencies get downconverted and the lower upconverted which results in a spectral narrowing. This effect was demonstrated experimentally and explained by Oberthaler and Höpfel [34]. In section 4.3 I will show measurements and numerical simulations that illustrate the dependence of spectral width change due to SPM on the pulse chirp.

2.4.4 Higher-order nonlinear effects

Although the propagation equation 2.4.7 on the facing page successfully explains a large number of nonlinear effects, for pulses that are shorter than 1 ps the spectral width becomes large enough that several approximations made in its derivation are not necessarily valid anymore.

First of all, intrapulse Raman scattering starts to play a significant role. The physical origin of this effect is the delayed nature of the Raman (vibrational) response. As a result, the low-frequency components of a pulse get amplified by an energy transfer from the high-frequency components of the same pulse and the whole pulse spectrum shifts toward the low-frequency side. This phenomenon can be described by introducing a time-dependent third-order susceptibility. Another consequence of the broad spectrum is that more terms in the Taylor expansion of $\beta(\omega)$ and $\Delta\beta(\omega)$ (see eq. 2.4.6) have to be included.

The propagation equation now takes the form [1]

$$\frac{\partial A}{\partial z} = \left[-\frac{i\beta_2}{2} \frac{\partial^2 A}{\partial T^2} + \frac{\beta_3}{6} \frac{\partial^3 A}{\partial T^3} - \frac{\alpha}{2} + i\gamma \left(|A|^2 + \frac{i}{\omega_0} \frac{1}{A} \frac{\partial}{\partial t} (|A|^2 A) - T_R \frac{\partial |A|^2}{\partial t} \right) \right] A. \quad (2.4.15)$$

There are two new nonlinear terms in this expression. The term proportional to ω_0^{-1} results from the frequency dependence of $\Delta\beta(\omega)$; the frequency dependence of both n_2 and A_{eff} is included here. It is responsible for self-steepening. The last term proportional to T_R has its origin in the Raman response. T_R is the first moment of the nonlinear response function that has to be included in $\chi^{(3)}$ to describe the delayed character of Raman scattering [1].

Equation 2.4.15 is written in a different frame of reference than eq. 2.4.7 on the preceding page. The new frame of reference is moving with the pulse at its group velocity v_g and is defined by the transformation [1]

$$T = t - \frac{z}{v_g} \equiv t - \beta_1 z. \quad (2.4.16)$$

2.4.5 Split-Step Fourier Method

To understand the idea behind the split-step Fourier method it is useful to write the NLSE formally in the form [1]

$$\frac{\partial A}{\partial z} = \left[\hat{D} + \hat{N}(A) \right] A, \quad (2.4.17)$$

where \hat{D} is a differential operator that contains the linear part of the equation, that is dispersion and losses, and \hat{N} is a nonlinear operator that describes the effect of fiber nonlinearities. In general, all these effects act together along the length of the fiber. The split-step Fourier method obtains an approximate solution by assuming that for a small propagation distance h the dispersive and nonlinear effects act independently. The propagation over distance h is carried out in two steps: in the first step only \hat{N} is not zero and in the second only \hat{D} .

Because of the form of the operators \hat{D} and \hat{N} it is convenient to make the linear step in the frequency domain and the nonlinear one in the time domain. This requires taking the Fourier and the inverse Fourier transforms for each step, hence the word ‘‘Fourier’’ in the name. However, this is quite efficient if the finite-Fourier-transform (FFT) algorithm is used, so the split-step Fourier method is much faster than most other methods. [1]

2.5 Jones formalism for polarized light

Until now I considered linearly polarized electric fields. In this section I will introduce the Jones formalism which is a convenient way to describe the polarization state of coherent light. In this formalism the electric field is described by a complex vector

$$\mathbf{E}_0 = \begin{bmatrix} E_x \\ E_y \end{bmatrix}. \quad (2.5.1)$$

The magnitude of the relative phase between E_x and E_y determines whether the light is linearly, circularly or elliptically polarized and the sign of the phase determines helicity. An optical element is described by a 2×2 matrix \mathbf{J} so that

$$\mathbf{E}_{out} = \mathbf{J}\mathbf{E}_{in}. \quad (2.5.2)$$

The Jones theorems [35] state that any optical system is equivalent to a systems consisting of just a few (at most four) elements. Each of the elements is described by one of the three operators: polarizer \mathbf{J}_{pol} , retardation plate \mathbf{J}_{ret} , and rotator \mathbf{J}_{rot} . The matrices representing these operators are:

$$\mathbf{J}_{pol} = \begin{bmatrix} p_x & 0 \\ 0 & p_y \end{bmatrix}, \quad \mathbf{J}_{ret}(\phi) = \begin{bmatrix} e^{i\phi/2} & 0 \\ 0 & e^{-i\phi/2} \end{bmatrix} \text{ and } \mathbf{J}_{rot}(\theta) = \begin{bmatrix} \cos \theta & -\sin \theta \\ \sin \theta & \cos \theta \end{bmatrix}, \quad (2.5.3)$$

where p_x and p_y are real numbers between 0 and 1. If $p_x = 1$ and $p_y = 0$, \mathbf{J}_{pol} represents an ideal polarizer. For $p_x = p_y$ it is an attenuator. If an element described by a matrix \mathbf{J} is rotated by an angle θ , its new matrix can be found by rotation transformation

$$\mathbf{J}' = \mathbf{J}_{rot}(-\theta)\mathbf{J}\mathbf{J}_{rot}(\theta). \quad (2.5.4)$$

Including the rotation operators for describing the relative orientations of elements, an optical system can be described by a sequence of seven operators:

$$\mathbf{J} = \mathbf{J}_{rot}(\theta_1)\mathbf{J}_{ret}(\phi_1)\mathbf{J}_{rot}(\theta_2)\mathbf{J}_{pol}\mathbf{J}_{rot}(\theta_3)\mathbf{J}_{ret}(\phi_2)\mathbf{J}_{rot}(\theta_4). \quad (2.5.5)$$

This relatively simple formalism is sufficient to describe fully polarized light. Randomly polarized, partially polarized, or incoherent light would have to be treated using Mueller calculus.

Experimental setup

3.1 Femtosecond pulse generation

3.1.1 Oscillator

All ultrashort pulses used in this work were generated by a Ti:sapphire femtosecond oscillator. The titanium-doped aluminum oxide (Al_2O_3) crystal serves as the active medium in the laser and at the same time provides the mechanism for generation of ultrashort pulses, the Kerr lens mode locking [36]. Due to nonlinear refraction a beam with a higher peak intensity has a smaller waist in the crystal. At the same time, because of the broad gain profile of the Ti:sapphire crystal many longitudinal modes appear in the cavity which leads to intensity fluctuations in the time domain. In consequence, if the cavity is designed in such a way that the beam with the smaller waist experiences smaller loss, it can happen that an intensity maximum that appeared due to fluctuations will be amplified more than the rest of the beam and the whole energy in the cavity will be transferred to a single short pulse.

Apart from nonlinear gain (sometimes referred to as artificial saturable absorber), mode-locked lasers require some kind of intracavity dispersion compensation mechanism. This is usually done by introducing optical components with anomalous dispersion to counteract the naturally occurring normal dispersion.

For the experiments presented in this work a commercially available femtosecond oscillator Mira Seed produced by Coherent, pumped by Verdi V5, was used [37]. The laser generates ultrashort pulses by Kerr lens mode locking. Beam waist-dependent loss is introduced by adjusting the width of a slit inserted in one of the resonator arms. A prism pair provides chromatic dispersion compensation so that pulses with spectral width up to 50 nm can be generated. In addition, the central wavelength can be tuned with a birefringent filter. There is no element that enables a direct control over the spectral bandwidth, but the amount of intracavity dispersion can be changed by shifting one of the prisms and thus generating pulses with different spectral bandwidths is possible. In this work pulses with FWHM between 20 and 30 nm were used.

3.1.2 Amplifier

The femtosecond oscillator Mira Seed delivers pulses with up to 10 nJ pulse energy. If this was not sufficient, a regenerative amplifier (RegA 9050, Coherent) continuously pumped with 9 W power by a Millennia X (Spectra Physics) was used. Just like the oscillator, the amplifier uses a Ti:sapphire crystal as the active medium. A seed pulse is injected into the cavity and then ejected after a prescribed number of roundtrips by means of diffraction on an acoustic wave generated in a TeO_2 crystal. The central wavelength and spectral bandwidth of the amplified pulse are a result of an interplay between the seed pulse spectrum and the amplifier gain.

The parameters of the femtosecond laser system used in this work are summarized in table 3.1.

3.1.3 Pulse compression

Although the net cavity dispersion of a femtosecond oscillator has to be close to zero, the pulse leaving the output coupler is generally chirped. To obtain a TL pulse, an external compensation is

	Mira	RegA
central wavelength tunability	760-840 nm	780-820 nm
FWHM spectral width	16-50 nm	20-30 nm
pulse energy	10 nJ	4 μ J
repetition rate	76 MHz	\leq 300 kHz

Table 3.1: Specifications of the femtosecond laser system [37–39].

required. This was achieved by using a prism compressor consisting of two identical fused silica prisms. The beam is reflected after the second prism so that it passes through each prism twice and exits the dispersion line almost parallel to the input beam. The prism compressor can only compensate the second-order dispersion so that the pulse compressed this way is always slightly longer than TL. The remaining third- and higher-order dispersion can be removed with a pulse shaper.

The amplifier used in this work operates on the principle of chirped pulse amplification (CPA) [40]. In this scheme the pulse is stretched before entering the amplifier to reduce the peak intensity and then after amplification recompressed by applying the same amount of dispersion with the opposite sign. For this purpose RegA 9050 is equipped with a stretcher-compressor system. Each of those two setups contains one diffraction grating that reflects the beam four times. The gratings are identical, but the the stretcher contains a relay imaging telescope which creates an effective negative distance. If the optical path of the beam and the grating angles of the stretcher and the compressor are the same, then the GVD and the TOD are perfectly balanced. The additional GVD introduced by the amplifier optics can be compensated for by adjusting the distance of one of the gratings and a mismatch of the grating angles enables the TOD compensation. Again, higher-order dispersion can be compensated for by a pulse shaper.

One disadvantage of grating stretchers and compressor is that they are very sensitive to alignment. It has been shown that if conventional alignment methods and standard diagnostic techniques are used, there is usually some residual angular chirp left [41,42]. In case of the stretcher this limits the amplified bandwidth. Angular chirp after the compressor leads to temporal distortions, tilted pulse fronts and reduced intensity in focus. All this is detrimental for coherent control.

3.2 Pulse shaping

There are several ways to realize a programmable pulse shaper. Most of them belong to one of the two classes: spatial masks in the Fourier plane of a zero-dispersion line, already mentioned in 2.2.2, or shapers employing the phase transfer principle, such as acousto-optic programmable dispersive filters (AOPDF) [43]. Examples of setups suitable for different applications and spectral ranges as well as discussion of their limitations can be found in the extensive review by Weiner [44] or in the newer paper by Monmayrant et al. that incorporates the latest developments in the field of pulse shaping and characterization [8]. Here I will discuss one kind of a spatial mask, the liquid crystal (LC) spatial light modulator. I will show several examples of pulse shaper setups based on this principle that I used in my work.

3.2.1 Liquid crystal modulator

A liquid crystal modulator consists of a thin layer of nematic (that is, with long-range directional order) liquid crystal (LC) placed between two glass substrates as shown in fig. 3.1. One side is

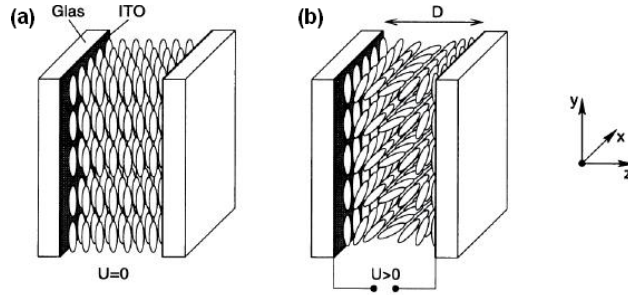


Figure 3.1: A single pixel of a LC modulator. (a) Without voltage, the molecules stay parallel to the pixel surface. (b) If a voltage is applied, they start to turn in plane. This causes a change of the refractive index for one polarization direction.

covered with transparent electrodes which enable the application of voltage. If no voltage is applied, the elongated LC molecules are oriented in one direction parallel to the substrate (fig. 3.1(a)). Otherwise they tend to align along the field by rotating in plane (fig. 3.1(b)). The liquid crystal is birefringent, with different refractive indices in the planes perpendicular and parallel to the long axes of the molecules. Consequently, in the parallel plane the refractive index of the crystal depends on the molecules orientation and thus on voltage. Liquid crystals have many applications, including the widely used LC displays where a crystal is placed between two crossed polarizers and transmits light only if birefringence is induced by applying voltage.

In my work I used a programmable LC light modulator SLM-640 from Cambridge Research Instruments. It consists of two one-dimensional LC arrays 640 pixels each. In some experiments a smaller version of this modulator, SLM-128 with two 128 pixel arrays, was used as well. In both devices the crystals in the two arrays are oriented at $+45^\circ$ and -45° to the horizontal. The Jones matrix of a single pixel can be expressed as a product of wave retarders and rotators (see eq. 2.5.3) [39]:

$$\mathbf{J}_{dlc}(\varphi_a, \varphi_b) = \mathbf{J}_{rot}(+45^\circ) \mathbf{J}_{ret}(\varphi_b) \mathbf{J}_{rot}(-45^\circ) \mathbf{J}_{rot}(-45^\circ) \mathbf{J}_{ret}(\varphi_a) \mathbf{J}_{rot}(+45^\circ) = e^{\frac{i}{2}(\varphi_a + \varphi_b)} \begin{bmatrix} \cos\left(\frac{\varphi_a - \varphi_b}{2}\right) & i \sin\left(\frac{\varphi_a - \varphi_b}{2}\right) \\ i \sin\left(\frac{\varphi_a - \varphi_b}{2}\right) & \cos\left(\frac{\varphi_a - \varphi_b}{2}\right) \end{bmatrix}. \quad (3.2.1)$$

The phase retardances φ_a and φ_b are functions of applied voltages.

The vector describing the electric field after it passed through such a pixel can be calculated by multiplying the input electric field vector by the Jones matrix of the pixel. Assuming that the input electric field is horizontally polarized, one obtains

$$\mathbf{E}_{out} = \mathbf{J}_{dlc}(\varphi_a, \varphi_b) \cdot E_0 \begin{bmatrix} 1 \\ 0 \end{bmatrix} = E_0 e^{\frac{i}{2}(\varphi_a + \varphi_b)} \begin{bmatrix} \cos\left(\frac{\varphi_a - \varphi_b}{2}\right) \\ i \sin\left(\frac{\varphi_a - \varphi_b}{2}\right) \end{bmatrix}. \quad (3.2.2)$$

This vector describes elliptically polarized light. The principal axes of the polarization ellipse are parallel to the horizontal and vertical directions and the ellipticity (ratio of principal axes lengths) is

$$r = \frac{E_{minor}}{E_{major}} = \min \left(\tan \left(\frac{\varphi_a - \varphi_b}{2} \right), \cot \left(\frac{\varphi_a - \varphi_b}{2} \right) \right). \quad (3.2.3)$$

This definition ensured that the ellipticity is always between 0 and 1 (or -1 and 1 to include helicity).

By changing the two independent parameters, φ_a and φ_b , it is possible to control two parameters of the electromagnetic wave - in this case phase and polarization ellipticity (but not orientation). A full control of polarization would require another independent parameter. The idea

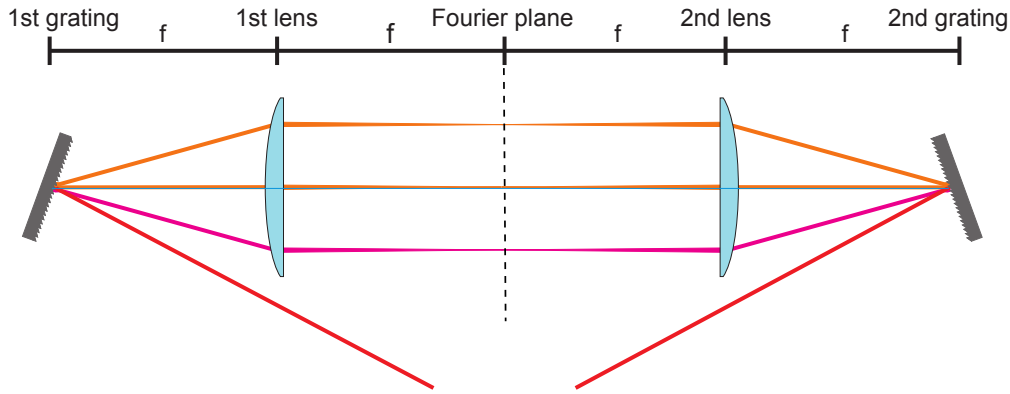


Figure 3.2: $4f$ setup consisting of two diffraction gratings and two cylindrical lenses.

of polarization shaping using two LC arrays oriented at $+45^\circ$ and -45° was first introduced by Wefers and Nelson [45].

3.2.2 $4f$ setup

A single piece of liquid crystal could be used to adjust the overall phase and polarization of light. In fact, variable, electronically controlled liquid crystal wave plates are commercially available. However, they are much too slow to control the time-dependent parameters of an ultrashort pulse. Actually, there is no electronic device fast enough to shape a femtosecond pulse in the time domain. The modulation has to be done in the spectral domain instead, for example with an array of independent liquid crystals, each of them modulating a different spectral component of the pulse. A versatile pulse shaper setup which makes it possible to control spectral components of the pulse independently, a $4f$ line, was first proposed by Froehly and co-workers in 1983 [46].

A $4f$ line is a particular arrangement of a pair of diffraction gratings and a pair of lenses with focal length f . As shown in fig. 3.2, the gratings are at a distance f from the lenses and the total length of the setup is $4f$, hence the name. When the input laser beam hits the first grating, each of its spectral components is angularly dispersed and then focused to a small spot by the first lens in plane at a distance f from the lens. In this plane, called Fourier plane, the spectral components are maximally separated, so this is where the SLM is placed. At the same time the Fourier plane is the symmetry plane of the setup.

In other versions of the $4f$ setup the gratings are replaced by prisms or the lenses by curved mirrors. The main advantage of using mirrors is avoiding additional dispersion and chromatic aberrations. Folded setups with a mirror placed directly after the modulator are sometimes used as well.

The resolution of the setup depends on the focal length f and the grating period d . In addition, the finite size of the focus has to be taken into account. For a pulse with central wavelength λ_0 and the input beam size Δx_{in} (related to the waist of the beam w_{in} by $\Delta x_{in} = w_{in} \sqrt{2 \ln 2}$) the focus size is [8]

$$\Delta x_0 = 2 \ln 2 \frac{\cos \theta_i}{\cos \theta_d} \frac{f \lambda_0}{\pi \Delta x_{in}}, \quad (3.2.4)$$

where θ_i is the incident angle of the grating and θ_d the diffraction angle. The choice of θ_i depends on the grating - the angle has to be chosen so that the efficiency in the chosen diffraction order is as close to one as possible to minimize loss. The size of the input beam Δx_{in} is limited by the

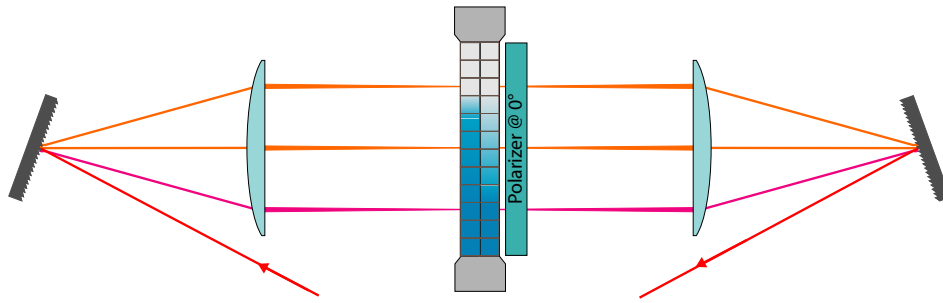


Figure 3.3: Pulse shaper setup for phase and amplitude shaping. A double array LC SLM is placed in the Fourier plane of a $4f$ line. A horizontally oriented polarizer selects one component of the modulated ellipse. Picture taken from [39].

vertical aperture of the modulator, in case of SLM-640 5 mm. The only remaining parameter is f . From looking at expression 3.2.4 it seems that f should be as small as possible. However, there is another parameter of the $4f$ setup that has to be considered: the width of the dispersed spectrum in the Fourier plane. For a frequency component ω_k the position in the Fourier plane is

$$X_k = \alpha \omega_k, \quad (3.2.5)$$

where α depends on the $4f$ line geometry:

$$\alpha = \frac{\lambda_0^2 f}{2\pi c d \cos \theta_d}. \quad (3.2.6)$$

α is proportional to f , so to illuminate as many pixels of the mask as possible one wants f to be big - which makes the focal spot in the Fourier plane bigger and limits the resolution. This means that a compromise has to be found.

In practice, the resolution of the shaper setup is limited by the resolution of the modulator itself, in case of a LC array the pixel size, which is $100 \mu\text{m}$ for the SLM-640. It is sufficient if the focus size is smaller than the pixel size.

For the $4f$ setups used for the experiments presented here two pairs of cylindrical lenses were used, one with $f = 200 \text{ mm}$ and one with $f = 250 \text{ mm}$. For an input beam with 5 mm diameter this results in $40 \mu\text{m}$ and $50 \mu\text{m}$ focus respectively, in both cases smaller than the pixel size. In both cases the same diffraction gratings with 1200 lines/mm were used. The resolution (determined experimentally by measuring the wavelength transmitted through each pixel separately) was 0.340 nm/pixel for the 200 mm lenses and 0.277 nm/pixel for the 250 mm lenses.

3.2.3 Phase and amplitude shaping

The double array SLM described in section 3.2.1 can be used for phase and amplitude shaping. For that a horizontally oriented polarizer is placed directly after the modulator or after the second grating (see fig. 3.3). The output electric field is now linearly polarized and has the form

$$\mathbf{E}_{out} = E_0 e^{\frac{i}{2}(\varphi_a + \varphi_b)} \cos\left(\frac{\varphi_a - \varphi_b}{2}\right). \quad (3.2.7)$$

It is more convenient to specify the spectral phase and transmission that should be applied by the modulator than the retardances of the arrays. For a given spectral phase ϕ and transmission T the retardances $\varphi_{a,b}$ can be calculated [39]

$$\varphi_{a,b} = \frac{\pi}{2} + \phi \pm \arccos(\sqrt{T}). \quad (3.2.8)$$

The retardances have to be in the $(-\pi, \pi)$ range. If one wants to apply a phase function that exceeds this range, it has to be wrapped, that is, the $\text{mod } 2\pi$ operation has to be performed. A wrapped function is equivalent to the unwrapped one because applying a phase shift of $n \cdot 2\pi$ has no influence on the electric field.

3.2.4 Polarization shaping

There are several known pulse shaper setups capable of full or restricted control of polarization. One of them was already mentioned in sec. 3.2.1. It is similar to the setup in fig. 3.3, but with the polarizer removed. For a complete description of this setup, one has to include the influence of the second diffraction grating which typically has different reflectivity for horizontally and vertically polarized light. To take this into account, the electric field described by eq. 3.2.2 has to be multiplied by a matrix

$$\mathbf{J}_g = \begin{bmatrix} 1 & 0 \\ 0 & \sqrt{g} \end{bmatrix}. \quad (3.2.9)$$

Analogically to eq. 3.2.8 formulas connecting retardances to a given phase and ellipticity can be derived. Brixner and Gerber chose a different approach. To keep the energy of the shaped pulses constant, they placed a stack of Brewster plates after the shaper to attenuate the polarization component that was more efficiently reflected by the grating [47]. The setup they developed was subsequently applied to coherent control of K_2 molecules [48].

One does not have to think about polarized light in terms of polarization ellipse. A much simpler and in some situations more convenient way to describe a polarized electromagnetic wave is to consider two orthogonal polarization components with independent phases. These phases correspond simply to the retardances of the individual arrays. Theoretically, this setup is identical to the previous one and described by the matrix 3.2.1. Practically, one needs to take into account the grating reflectivity and multiply matrix 3.2.1 by 3.2.9. However, after this operation the eigenvectors of the matrix change. Physically this means that the simplicity which was the main advantage of this configuration - each polarization component controlled independently by one of the arrays - is lost. The solution is to place a half wave plate after the SLM inside the $4f$ setup to rotate the polarization by 45° before the beam hits the second grating. This way the reflection from the grating does not mix the polarization components but only changes the amplitude ratio. The modulation induced by this setup is then described by the matrix

$$\mathbf{J}_{AB} = \mathbf{J}_g \mathbf{J}_{rot}(+\pi/4) \mathbf{J}_{dlc} = \frac{1}{\sqrt{2}} \begin{bmatrix} e^{i\varphi_a} & e^{i\varphi_a} \\ -\sqrt{g}e^{i\varphi_b} & \sqrt{g}e^{i\varphi_b} \end{bmatrix}. \quad (3.2.10)$$

and the output electric field has the form

$$\mathbf{E}_{out} = \mathbf{J}_{AB} \begin{bmatrix} E_0 \\ 0 \end{bmatrix} = \frac{E_0}{\sqrt{2}} \begin{bmatrix} e^{i\varphi_a} \\ -\sqrt{g}e^{i\varphi_b} \end{bmatrix}. \quad (3.2.11)$$

The principle of operation of this setup is schematically shown in fig. 3.4. This setup was used for some experiments described in this work in section 5.4.

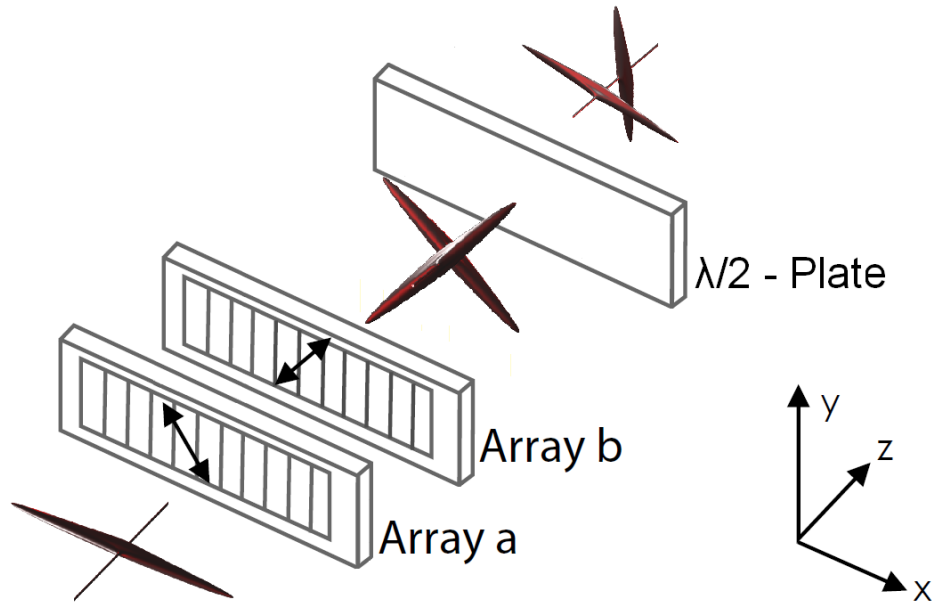


Figure 3.4: The principle of operation of the independent arrays setup for polarization shaping. Each of the two orthogonal polarization components experiences modulation by one of the two orthogonal SLM arrays. In the example shown here one of the components is delayed with respect to the other. Next, the shaped pulse is rotated by 45° by a half wave plate.

The setups I described until now utilized one double array LC modulator to control two parameters of the electric field. The number of parameters required for a full control of the electric field is four [49]. This can be still achieved in a setup with only one modulator by placing the modulator in a Mach-Zehnder interferometer and using one half of the array pixels for each polarization component [50]. However, this solution is not very practical as it requires interferometric stability. More recently, modified more stable versions of this setup were demonstrated [51, 52], but they still have the property that the two polarization components are first spatially separated and then recombined, so they are not entirely free from interferometric stability problems.

Another way to get more than two degrees of freedom out of one modulator is to sequentially pass the pulse through different areas of the SLM, with a polarizer between the two passes [53]. Although this setup uses effectively four LC masks, it offers control of only three parameters: phase, amplitude and ellipticity, but not the orientation. Its main advantage over the Mach-Zehnder setup is no need for interferometric stability.

For some experiments presented in this work another version of the setup described above was used. Instead of different areas of a single modulator, two modulators with a polarizer in between placed in a single $4f$ setup were used (see fig. 3.5). The matrix describing this configuration can be obtained by multiplying the matrices of the three elements

$$\mathbf{J}_{2SLM} = \mathbf{J}_{dlc}(\varphi_c, \varphi_d) \mathbf{J}_{pol}(1, 0) \mathbf{J}_{dlc}(\varphi_a, \varphi_b) = \quad (3.2.12)$$

and the output electric field has the form

$$\mathbf{E}_{out} = \mathbf{J}_{2SLM} \begin{bmatrix} E_0 \\ 0 \end{bmatrix} = E_0 e^{i(\varphi_a + \varphi_b + \varphi_c + \varphi_d)} \cos\left(\frac{\varphi_a - \varphi_b}{2}\right) \begin{bmatrix} \cos\left(\frac{\varphi_c - \varphi_d}{2}\right) \\ i \sin\left(\frac{\varphi_c - \varphi_d}{2}\right) \end{bmatrix}. \quad (3.2.13)$$

There are four independent parameters in this expression, but two of them, $(\varphi_a + \varphi_b)$ and $(\varphi_c + \varphi_d)$, control the phase, although one would be sufficient, and the orientation of the polarization ellipse is fixed. As a result, this setup allows phase, amplitude and restricted polarization shaping.

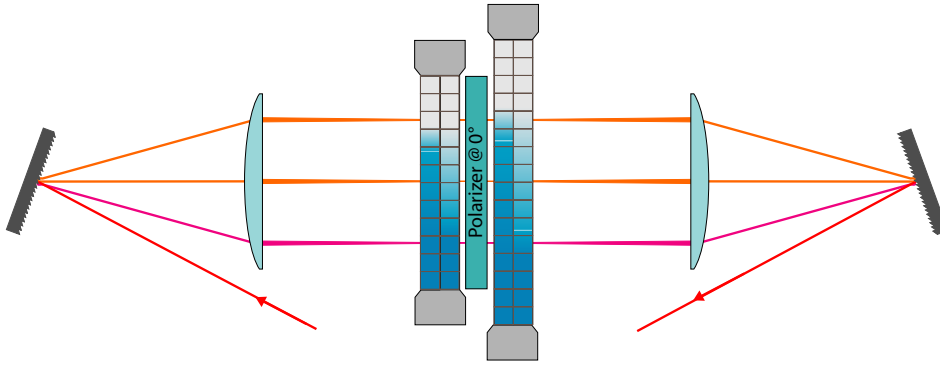


Figure 3.5: Setup for phase, amplitude and (restricted) polarization shaping. Two double LC modulators separated by a polarizer are placed in the Fourier plane. The functionality of the setup is identical to the one described in [53]. Picture taken from [39].

The easiest way to implement this setup would be to use two SLM-640 modulators, but only one was available, so the SLM-128 was used instead. Fortunately, the two modulators have the same pixel size which simplifies the conversion of frequency-dependent retardances into voltages arrays.

In their paper [53] Plewicki et al. not only presented a setup for restricted polarization shaping, but also proposed a similar one capable of full polarization shaping. It consists of four arrays at orientations that are not achievable with two double layer SLM with arrays at $\pm 45^\circ$. The setup was later realized using three standard double layer modulators, but with two of the six arrays not active [49].

3.2.5 Limitations of a pulse shaper

To interpret experimental results correctly it is necessary to know the limitations of the shaper setup and possible deviations from the desired pulse shape that can result from them.

One of the limitations is the already mentioned finite pixel size together with the finite number of pixels. The resolution of the $4f$ line can be obtained from equations 3.2.5 and 3.2.6 [8]:

$$\delta\omega = \frac{\Delta x_0}{\alpha}. \quad (3.2.14)$$

However, this is true only for continuous mask. In case of pixelated masks the resolution is limited by the pixel size instead of the focus size. Through the Fourier transform, the resolution corresponds to a window T in the time domain [8]

$$T = \frac{4 \ln 2}{\delta\omega}, \quad (3.2.15)$$

which is the time window available for shaping. It defines a temporal upper bound for shaping achievable with a $4f$ line (the temporal lower bound is determined by the available optical bandwidth). If the duration of the shaped pulse is much bigger than T , distortions occur. However, it must be noted that the time window is in fact not a single number, but rather a function - Gaussian shaped - that describes the capability of delaying the pulse by a certain time. T as given by eq. 3.2.15 describes the FWHM of this function. As shown in [8], a subpulse delayed by a half of this distance will have only a half of the maximal peak intensity.

The resolutions of the shaper setups used in this work was given in 3.2.2. They correspond to a time window of 2.6 ps for the setup with the worse resolution ($f = 200$ mm) and 3.2 ps for the setup with improved resolution ($f = 250$ mm).

Let us now consider in more detail what happens to the beam in a $4f$ line. The first grating couples each spectral component into a given direction, which is then mapped by the first lens to a given position in the Fourier plane. As a result, any position in the Fourier plane corresponds both to a certain frequency component and to a certain direction. Consequently, the part of the mask lying at this position acts simultaneously on both frequency and direction. This is the origin on an effect called space-time coupling [8]. It turns out that this effect is inherent not only to SLMs in a $4f$ line, but also to acousto-optic programmable dispersive filter (AOPDF)s [54], although there the mechanism is different.

There are several papers discussing different aspect of space-time coupling [55–58]. Here I will discuss one effect that is particularly relevant for the experiments presented in this work, namely the influence of applying significant linear chirp with the modulator on the beam profile. The analysis presented here is based on expressions presented in [58].

By using Fourier optics, one can obtain an expression for the slowly varying electric field $\tilde{A}(x, \Omega)$ depending on the position x with respect to the center of the beam and frequency Ω relative to the carrier frequency ($\Omega = \omega - \omega_c$). The y coordinate dependence is omitted because it remains unaffected by the shaper. The electric field directly after the shaper is found to be

$$\tilde{A}_s(x, \Omega) = \frac{ik_c}{bf} e^{-4ik_c f} \int_{-\infty}^{\infty} dx' \tilde{A}_{in}(-x', \Omega) \tilde{M} \left(\frac{-k_c}{bf} (x - x') \right) e^{i\gamma\Omega(x-x')/b}, \quad (3.2.16)$$

where $k_c = k(\omega_c)$ is the wave vector associated with the central frequency,

$$b = \frac{\cos \theta_i}{\cos \theta_d} \quad \text{and} \quad \gamma = \frac{2\pi}{\omega_c d \cos \theta_d} \quad (3.2.17)$$

are parameters of the $4f$ setup and $\tilde{M}(k_x)$ is the spatial Fourier transform of the modulator's transfer function $M(x)$.

As will be explained later, in most of the experiments in this work a quadratic phase offset of ≈ 50000 fs² is applied to compensate for the chromatic dispersion of the fiber. For a quadratic phase the transfer function takes the form $M(x) = e^{i\beta_2 x^2/2}$. After taking the Fourier transform and substituting it in eq. 3.2.16, the equation was solved numerically using Mathematica software. The results are shown in fig. 3.6. Fig. 3.6(a) shows the undistorted profile for a flat spectral phase. In fig. 3.6(b) a linear spatial chirp can be seen. Also the spectral phase shows some position dependence (fig. 3.6(c)). It can be expected that the spatial chirp introduced by the shaper will influence coupling of the pulse into the fiber and this is in fact the case. The corresponding measurements will be shown in sec. 4.1.2.

Limited time window and space-time coupling are present even in case of a continuous mask. In addition, there are some further known issues caused by the pixelization of the modulator. Several of them are analyzed in detail in [59]; here I will summarize them briefly.

The $100 \mu\text{m}$ wide pixels in the modulators used in this work are spaced by $2 \mu\text{m}$. An immediate consequence is that about 2% of the pulse spectrum remains unshaped, so there will be always a small pulse left at $t = 0$ (unless the modulator is placed between crossed polarizers). Secondly, the gaps cause smoothing of the phase, which at the first glance seems a good thing, but is undesirable in the points where the phase has to be wrapped. If the phase function contains big phase differences, the phase must be wrapped many times and so the deviation caused by the smoothing becomes significant. Finally, pixelization leads to appearance of replica pulses.

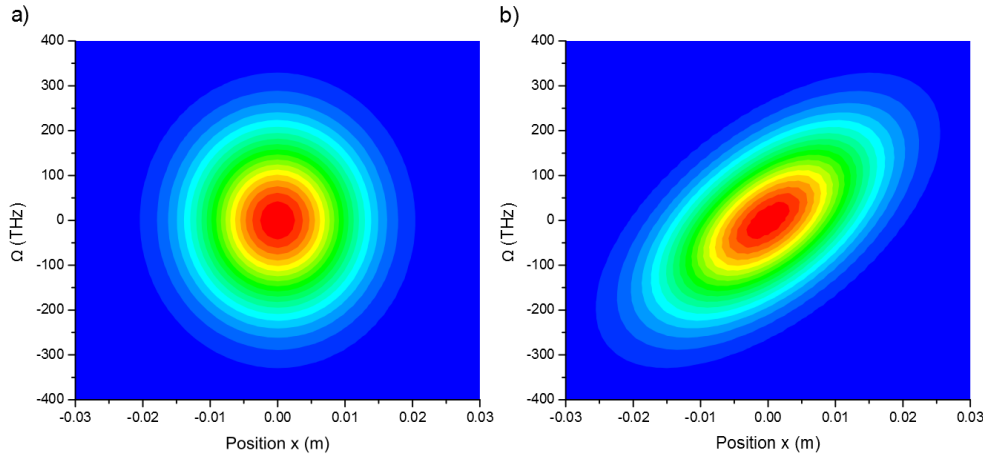


Figure 3.6: Solutions to eq. 3.2.16 describing space-time coupling. The field distributions for (a) a flat spectral phase ($\beta_2 = 0$) and (b) a quadratic spectral phase of 50000 fs^2 are shown.

Another issue that has to be considered is that if the pixel size is finite, the function to be written on the modulator cannot change too rapidly. This can be described mathematically by using the Nyquist theorem [39]. Applied to pixelated shapers it states that the phase difference between two adjacent pixels cannot be bigger than π .

The importance of the effects described here depends on the application. In the classical coherent control scheme, where a pulse shape is first found by optimization and then characterized by some pulse characterization method, errors in phase and amplitude caused by interpixel gaps and finite resolution are not so important. As long as the shaper is reproducible, the actual optimal pulse shape can be deduced from the measurement. However, one has to keep in mind that the limitations of the shaper introduce a certain bias. For example, two subpulses separated by a distance of the order of the time window will have a smaller overall intensity than two subpulses separated by half of this distance which can result in a smaller fitness even if the pulse with subpulses further apart is better suited to the investigated transition.

If parametric pulse shaping is employed, the setup has to be carefully calibrated and characterized prior to the measurement, but it has been shown that a high degree of agreement between the measured and the intended pulse shape is possible even for a relatively complicated setup for full phase, amplitude and polarization shaping [20].

Finally, depending on the experimental application, the refreshing rate of the shaper can play a role. In a LC modulator, turning of the liquid crystals required to change the retardance takes time (for the models used in this work 35 ms for 2π radians), but once the crystals are oriented, they stay in still. Consequently, the frequency of switching between different pulse forms is limited, but there is no limitation of the repetition rate of the laser pulses that can be shaped.

3.3 Pulse characterization

In any pulse shaping experiment a pulse characterization setup is required to confirm that the shaper setup functions as desired and to check its limitations. In this section I will shortly describe the pulse characterization methods used in this work and comment on their advantages and disadvantages. A detailed discussion of pulse characterization can be found in [60]. In [8], a shorter summary focused on application to shaped pulses can be found.

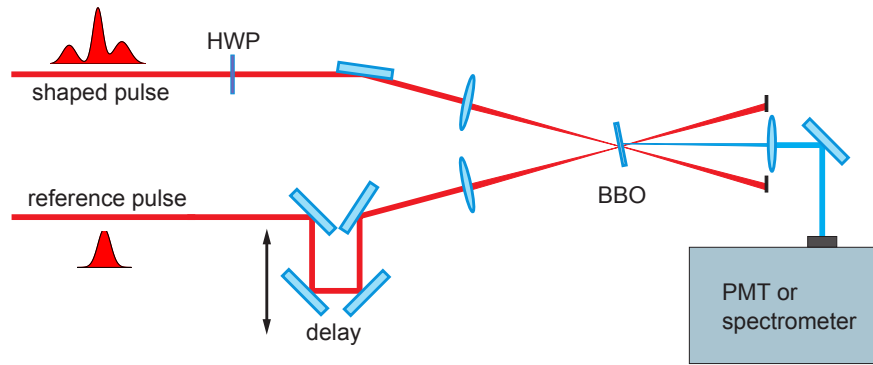


Figure 3.7: XC and XFROG setup capable of time-resolved ellipsometry measurement. A shaped pulse is rotated with a half wave plate (HWP) and overlapped with a short reference pulse in a BBO crystal. The second harmonic signal depending on delay is measured with a photomultiplier (PMT) or a spectrometer.

3.3.1 Autocorrelation

Autocorrelation is one of the simplest and most widely used pulse characterization methods. The autocorrelator setup is an interferometer with variable delay in one of the arms. After passing the interferometer both replicas of the pulse are focused and overlapped in a second-order nonlinear detector. For a pulse with time-dependent intensity $I(t)$ the measured signal is then

$$S(\tau) \propto \int I(t)I(t - \tau)dt. \quad (3.3.1)$$

This kind of autocorrelation is called intensity autocorrelation.

The main advantage of this device is simplicity. However, it provides only limited information of the pulse. It can be used to estimate the pulse duration and compare it to the duration of a TL pulse with the same spectrum. From the shape of the envelope one can draw some conclusions about the phase. However, the autocorrelation function is symmetric in time, so the sign of the phase cannot be deduced.

In my work I used two commercial autocorrelators made by APE. One of them, Mini, used a photodiode with a bandgap that was larger than the energy of a single infrared photon so that only two photon absorption was possible. The other one, PulseCheck, used a thin BBO crystal instead. The crystal angle had to be optimized prior to measurement. In addition, PulseCheck had a serial port that enabled recording the autocorrelation traces on a computer.

3.3.2 Cross-correlation and XFROG

Cross-correlation (XC) is an extension of the autocorrelation method, particularly suited for characterizing complex shaped pulses. The difference between cross-correlation and autocorrelation is that one of the replicas of the unknown pulse is replaced by a known reference pulse, preferably a TL one. Such a setup allows reconstruction of the intensity profile $I(t)$ of the unknown pulse. Some ambiguities remain, for example the relative phase between pulses in a pulse sequence cannot be deduced. The self-built cross-correlation setup that was used for measurements in this work is shown in fig. 3.7.

An easy way to extract more information from SHG autocorrelation or cross-correlation is to measure the spectrum of the second harmonic signal instead of its integrated intensity. The

self-referenced version of this method is called frequency resolved optical gating (FROG) and was first proposed by Kane and Trebino [61]. Although it provides more information than the autocorrelation, the time reversal ambiguity is still present and an iterative algorithm has to be used to extract phase and amplitude.

The time reversal ambiguity is absent in third-order FROG variations, where a third instead of second order nonlinear process is used for detection. One example is the transient grating (TG) FROG [62]. In our group TG FROG was successfully applied to characterizing sub-7 fs pulses with 500 nm bandwidth [63]. However, the use of third order nonlinearity makes this method particularly suited for pulses with high peak power. We choose instead to use cross-correlation FROG, or XFROG. For this the photomultiplier was replaced by a high resolution spectrometer sensitive in the 360-450 nm range (HR4000, Ocean Optics).

3.3.3 Polarization shaped pulses

The setup presented in fig. 3.7 was further extended to characterize polarization shaped pulses. Technically, this extension is very simple. A HWP is placed in the beam to rotate the polarization of the pulse. The BBO crystal is polarization sensitive, so only one polarization component will be selected and characterized. Retrieval is slightly more challenging. At each point in time, the angle-dependent function

$$P(\theta) = \frac{I}{2} \left(1 - \left(\frac{r^2 - 1}{r^2 + 1} \right) \cos(2(\gamma - \theta)) \right), \quad (3.3.2)$$

where I is the light intensity and r and γ are the polarization ellipse parameters: ellipticity (as defined in eq. 3.2.3) and orientation, is fitted to the measured data [39]. As there are three independent parameters, at least three projections are required to fully characterize the polarization. Afterwards, to visualize the result it is presented as a three-dimensional XC trace. It should be noted that this method is not sensitive to helicity.

Strictly speaking, the XC, three dimensional XC and XFROG traces have to be deconvoluted to obtain the actual time-dependent. However, in this work only measured traces will be presented.

3.3.4 Optimization of the pulse duration

In many cases the aim is not just to know the spectral phase of the pulse, but also to make it flat in order to obtain a TL pulse. To a certain degree this can be done with a prism or grating compressor that were described in section 3.1.3. If this is not sufficient or for some reason not practical, the pulse shaper can be used to determine an offset phase that yields a TL pulse at a given place in the setup. One way or the other, a feedback signal is needed.

An advantage of using the pulse shaper is the possibility of determining the compensation by an automated procedure, either a systematic one- or more-dimensional scan, or an optimization algorithm. In both cases a fast and robust feedback signal is required. An autocorrelator could be used, but a much faster and simpler method is to use a broadband nonlinear detector, such as a thin nonlinear crystal, and maximize the signal. In my work in I used a GaAsP diode which has no one-photon absorption at 800 nm, so only TPA can occur. It has been shown that the photocurrent of this photodiode is inversely proportional to the pulse duration for near infrared pulses [64]. The signal from the photodiode was converted by an analog-to-digital converter and directly used as a feedback signal. The sensitivity of the diode was adjusted by adapting the size of the focus on the diode and if this was not enough, a lock-in amplifier and a chopper running at about 300 Hz was used.

3.4 Test systems: nonlinear crystals and dyes

A part of this work concerns coherent control of two-photon transitions with shaped pulses. For demonstration of the control capability, two kinds of systems were used: BBO crystals and laser dyes in solution. The results of coherent control experiments are presented in chapters 5 and 7 respectively. Below I will summarize the technical aspects of the experiments.

3.4.1 BBO crystals

As explained in section 2.3, the SHG process is a good model for a nonresonant two-photon transition. It also has the advantages of technical simplicity and tunability. In this thesis I present experiments with SHG in β barium borate (BBO) crystals. BBO crystals are commonly used for doubling near-infrared light because of their large nonlinear coefficient, high damage threshold and excellent optical homogeneity.

As a model of a narrow TP transition, a 4 mm thick BBO crystal was used. The transition wavelength was tuned by rotating the crystal by a small angle and observing the second harmonic spectrum (see fig. 3.8). The second harmonic signal was separated from the fundamental frequency with a dichroic mirror and collected with a photodiode.

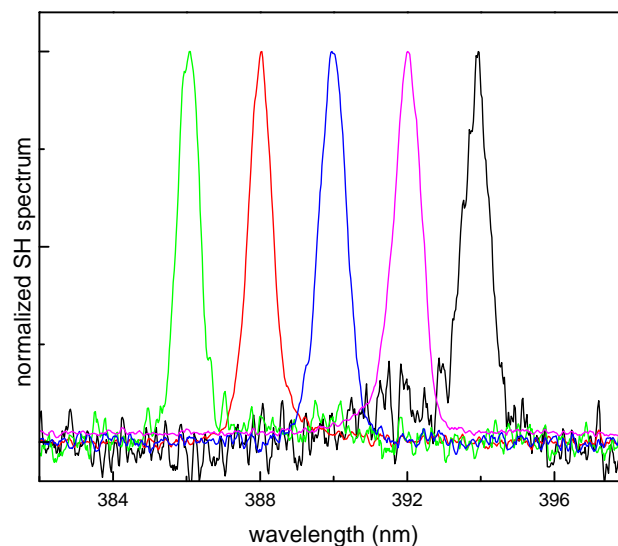


Figure 3.8: Second harmonic spectra from a 4 mm BBO crystal for different crystal angles.

One important point while using a thick SHG crystal is the beam divergence. The oscillator pulses, especially after transmission through the fiber, have relatively small pulse energy, so the beam waist inside the crystal has to be small to achieve a good conversion efficiency. At the same time, phase-matching in BBO and other birefringent nonlinear crystals is angle-sensitive, so the beam has to be well collimated within the whole crystal length using a telescope. Otherwise, if the beam is simply focused in the middle of the crystal, the convergent and divergent parts of the beam near the crystal faces are converted differently than the beam waist in the middle of the crystal.

A π step spectral phase scan, such as the one shown in fig. 2.2, is very sensitive both to the phase matching and to errors in the pulse spectral phase (resulting for example from a misalignment of the prism compressor). In practice it turned out that performing such a scan was the best way to verify the alignment at the beginning of each experiment day or after changing the setup configuration.

A second BBO crystal with a thickness of 0.3 mm was used as a model of a broad TP transition. This was the same crystal that was used for the XC measurements. It is thin enough to convert the whole pulse spectrum, especially after the spectral narrowing due to SPM but at the same time thick enough to yield a measurable signal.

3.4.2 Laser dyes

The choice of dyes suitable for the coherent control experiments as well as the choice of appropriate solvent for each dye and optimum concentration was the focus of the diploma thesis of Nona Rahmat [65]. For the measurements presented in this work three dyes were selected: Coumarin 1[†], Rhodamine B and Fluorescein isothiocyanate. They are listed in table 3.2 along with the abbreviated names used in the following part of the text. The spectral range in which the fluorescence was collected is shown as well.

name	abbreviation	solvent	fluorescence range (nm)
Coumarin 1	C1	ethanol	400-520
Rhodamine B	RB	ethanol	540-680
		alkaline water (pH 12)	580-670
Fluorescein isothiocyanate	FITC	alkaline water (pH 12)	480-540

Table 3.2: Laser dyes used in the selective excitation experiment. The abbreviated name, the solvent and the spectral range in which the fluorescence was collected (depending on the solvent) are listed.

Although one-photon excitation spectra of laser dyes are well known, this is not the case for two-photon excitation spectra. However, some data for the dyes used in this work is available. Ogilvie et al measured TP excitation of Coumarin 1 dissolved in methanol in the spectral range 400-430 nm [66]. According to this measurement the TP absorption maximum lies below 400 nm. In [67] more systematic measurements of several dyes in a broader spectral range including comparison to literature can be found. In fig. 3.9 the TP absorption spectra from Rhodamine B and Fluorescein are shown. The first one has a maximum at 420 nm and the second one at 390 nm, so a mixture of these two dyes should be suitable for testing selective TP excitation with pulses centered at 805 nm. However, it should be noted that the measurements were performed in different solvents: methanol for RB and alkaline water for FITC. Therefore it is not obvious how to achieve efficient selective excitation in a mixture, in particular, which solvent and what concentration should be used. Another possible choice for selective excitation is a mixture of C1 and RB. Here one encounters a similar problem: although TP absorption spectrum for each of the dyes dissolved in methanol is known, the absorption of C1 is given only in arbitrary units, so the optimal concentration had to be determined experimentally. The mixtures used in the presented measurements along with the concentrations and solvents are summarized in table 3.3

The experimental setup used to collect the fluorescence is presented in fig. 3.10 on page 36. The shaped laser beam is focused into a quartz cuvette (111-QS, Suprasil) containing the solution. Two other lenses collect the laser induced fluorescence into a fiber-coupled spectrometer operating in the visible range. The two regions of the spectrum corresponding to the fluorescence of the two dyes (see table 3.2) are integrated and saved as the fluorescence signal.

[†]also known as Coumarin 460 or Coumarin 47

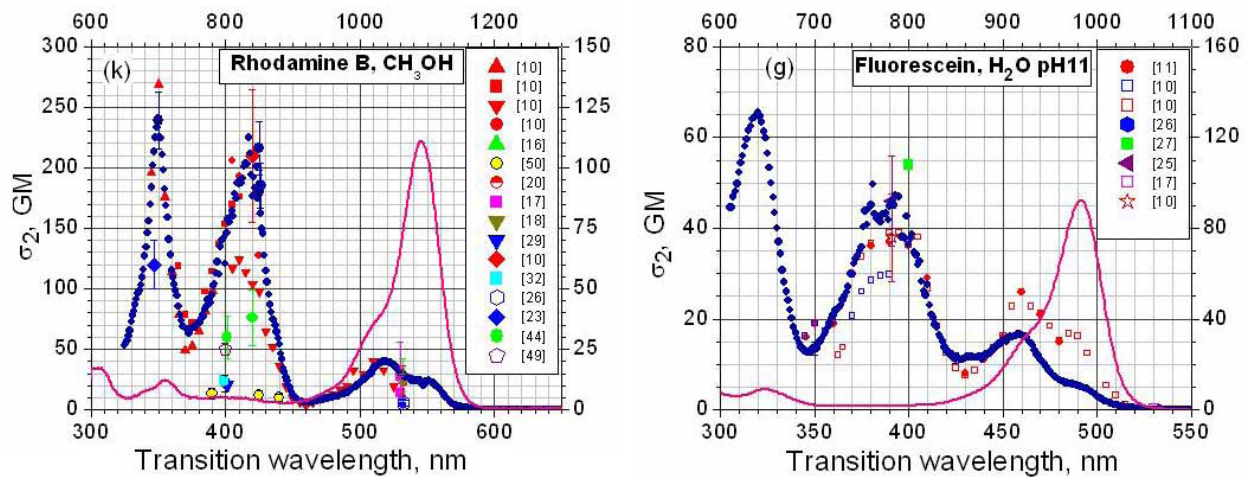


Figure 3.9: TPA spectra (dark blue circles, left vertical-axis) and molar extinction (magenta line, right vertical axis) for RB (left) and FITC (right) taken from [67]. Large dark blue circles are absolute cross sections at selected wavelengths measured here. Other symbols are the literature data with corresponding references shown in inset.

name	quantity (mM)	name	quantity (mM)	solvent
C1	6.6	RB	0.33	ethanol
FITC	2	RB	0.33	alkaline water

Table 3.3: Laser dyes mixtures used in the selective excitation experiment.

From the dimensions of the lens L2 and its distance from the laser beam focus it can be estimated that about 10% of the fluorescence was collected assuming isotropic emission. Out of that, probably about 15% was lost because of the lack of antireflective coating on the lenses. The efficiency of coupling into the spectrometer is difficult to estimate.

The focus of the laser beam is not in the center of the cuvette but rather close to the side on which the fluorescence is collected. This kind of geometry is necessary because otherwise the fluorescence intensity is diminished by reabsorption and cross-absorption. This is caused by the fluorescence spectrum of one dye overlapping with the absorption spectrum of the other dye. In addition, because the absorption and emission spectra of the dyes are broad, the fluorescence photons with shorter wavelength can be reabsorbed by the same dye that emitted them. This is illustrated by fig. 3.11 on the next page, where the joint fluorescence spectrum of two dyes is shown depending on the distance on the laser focus from the cuvette wall.

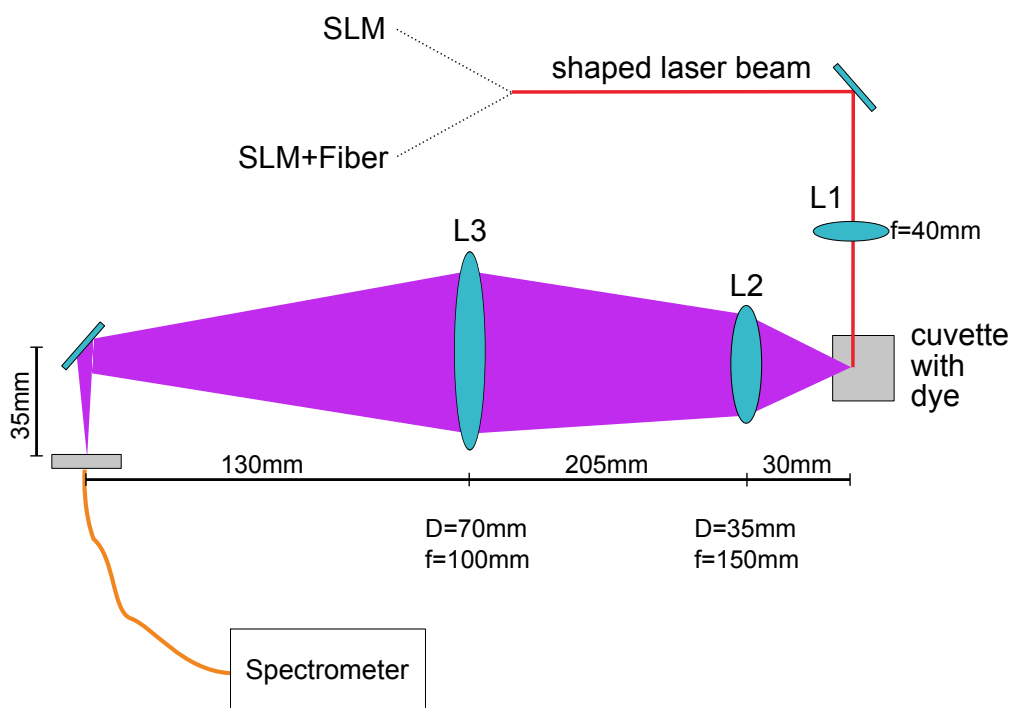


Figure 3.10: Experimental setup for collecting laser induced fluorescence. The shaped beam is focused in a cuvette with the lens L1. Part of the fluorescence is collected by a set of two lenses L2 and L3 and focused into a fiber coupled spectrometer. Focal lengths, diameters and distances of the lenses are marked on the picture.

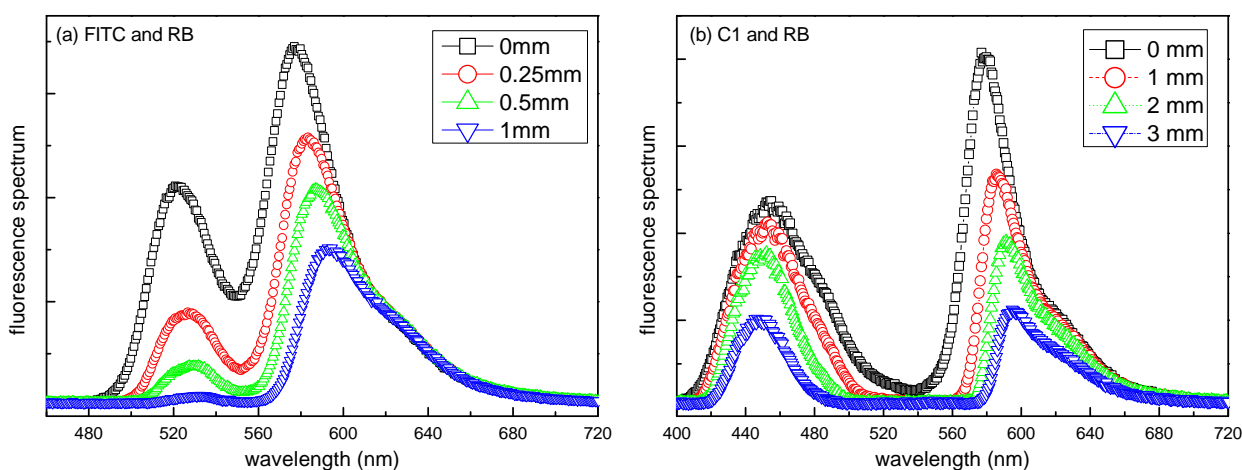


Figure 3.11: Collected spectra of the laser induced fluorescence emitted by a mixture of (a) FITC and RB and (b) C1 and RB depending on the distance of the laser focus from the cuvette wall.

Optical fiber

4

4.1 Coupling light into the fiber

The fiber used in this work was a standard silica single-mode step-index fiber SM750 produced by Fibercore Limited. The mechanism of guiding in step-index fibers as well as the motivation for using a single mode fiber was already discussed in section 2.1.3. In this section I will describe the coupling of the shaped laser beam into the fiber and its polarization properties. Next, measurements showing the influence of the linear and nonlinear effects on the pulse spectrum and duration will be presented. Finally, I will show examples of shaped pulses transported through the fiber in the linear regime. The results obtained in the nonlinear regime will be presented in the next chapters.

4.1.1 Mode diameter matching

The SM750 fiber has a mode field diameter of $5.3 \mu\text{m}$ at its operating wavelength 780 nm. The fiber was purchased in the form of a (nominally) 1 meter long cable with FC/PC (ferrule connector physical contact) connectors at both ends (F-SE-C-1FC, Newport). To be precise, two separate pieces of fiber with lengths of 115 cm and 104 cm were used during the measurements. The reason for replacing the fiber was damage of the fiber ends, most probably laser-induced.

To be coupled into the fiber the beam has to be focused to the appropriate size, i.e. the beam waist at the fiber input has to be as close as possible to the diameter of the fiber mode. Both too large and too small waist will result in loss. The beam was focused on the fiber end with a collimator designed to accept FC type fiber connectors and collimate a 780 nm beam exiting a single-mode fiber to a 3 mm beam (F-C5-F3-780, Newport). Thus for an optimal coupling the input beam had to be collimated with a 3 mm diameter. If necessary, the beam size after the shaper was adapted with a telescope. On the output a second identical collimator was used to collect and collimate the beam. The coupling efficiency achieved with these components was between 30% and 50%. It can be assumed that most of the loss was mostly due to mode mismatch on the fiber input.

4.1.2 Influence of space-time coupling on the output pulse spectrum

In addition to a constant loss resulting from the beam profile not matching the fiber mode, two other effects have to be considered before transporting shaped pulses through a fiber: spectrally dependent and pulse shape dependent loss. To investigate them, the pulse spectrum was measured in different conditions.

Special care has to be taken while measuring the pulse spectrum after the fiber, because spectral narrowing or broadening caused by SPM can obscure other effects. To avoid that a 10 cm long piece of SF10 glass was placed before the fiber to serve as a stretcher. In this configuration, if nothing was written on the shaper, the output spectrum was the same as the input spectrum, so it can be assumed that the fiber and the coupling optics exhibit no spectrally dependent loss. However, writing a linear chirp on the modulator caused visible narrowing. Examples of spectra measured after the fiber depending on the linear chirp are shown in fig. 4.1. $-5 \times 10^4 \text{ fs}^2$ is roughly the amount of linear chirp that is needed to compensate for the fiber dispersion.

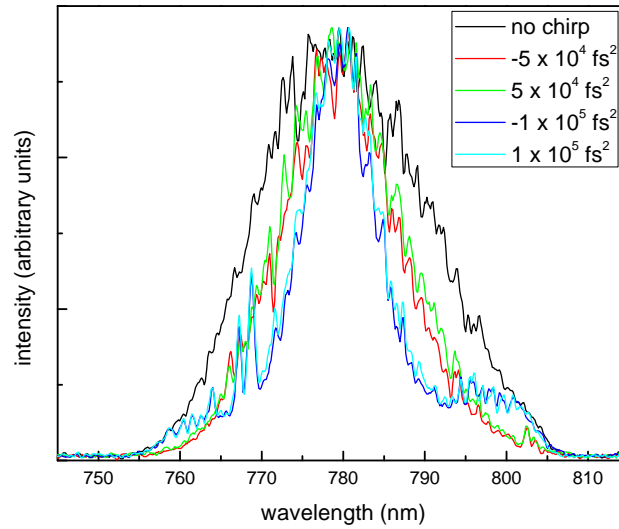


Figure 4.1: The influence of space-time coupling on the spectral amplitude of the pulse coupled into the fiber.

Frei et al. [58] state that if the beam is to be focused after the shaper, the lens should be located one focal length away from the shaper's last grating to minimize space-time coupling. However, the lens used to couple light into the fiber has a very short focal length so this is not practicable. An alternative is to relay image the last grating to the back focal plane of the lens. In the setup used in this work the distance between the last grating and the fiber was approximately 2 m, so I tried to improve the coupling by placing a relay imaging telescope consisting of two focusing lenses with 50 cm focal length after the shaper. However, contrary to the theoretical predictions there was no noticeable improvement in the coupled spectrum, so the telescope was removed.

It should be noted that the loss caused by space-time coupling means that a chirped pulse transported through the fiber has a slightly smaller (by about 10%) pulse energy than the unshaped pulse. Because the pre-chirp was applied in most of the measurements presented in the following chapters, the pulse energies given in the text will correspond to these of the pre-chirped pulses unless otherwise noted.

4.2 Polarization properties

Once the beam is optimally coupled into the fiber, the next step is to verify the output polarization. In spite of its name, a perfect single-mode fiber actually supports two orthogonally polarized modes. The fiber in use has no birefringence introduced on purpose, so theoretically the polarization state of the pulse should not be affected by the propagation as long as the pulse energy is low enough to avoid nonlinear effects. In practice, all fibers exhibit some birefringence because of unintentional variations in the core shape and anisotropic stress along the fiber length. Moreover, the degree of birefringence and the axes orientation can change randomly on a length scale of several meters [1]. However, it can be shown that even then there exist two orthogonal polarization states that propagate through the fiber unchanged [68]. Mathematically, these are the eigenstates of the Jones matrix describing the fiber and are referred to as principle states of polarization.

The principle states of polarization of a fiber are in general elliptical. It would be much more convenient to find linear polarization states that remain linear during propagation. It can be shown that such states must exist if the Jones matrix is unitary, that is if the fiber does not exhibit polarization dependent loss. If this is the case, then the fiber is equivalent to combination of a rotator

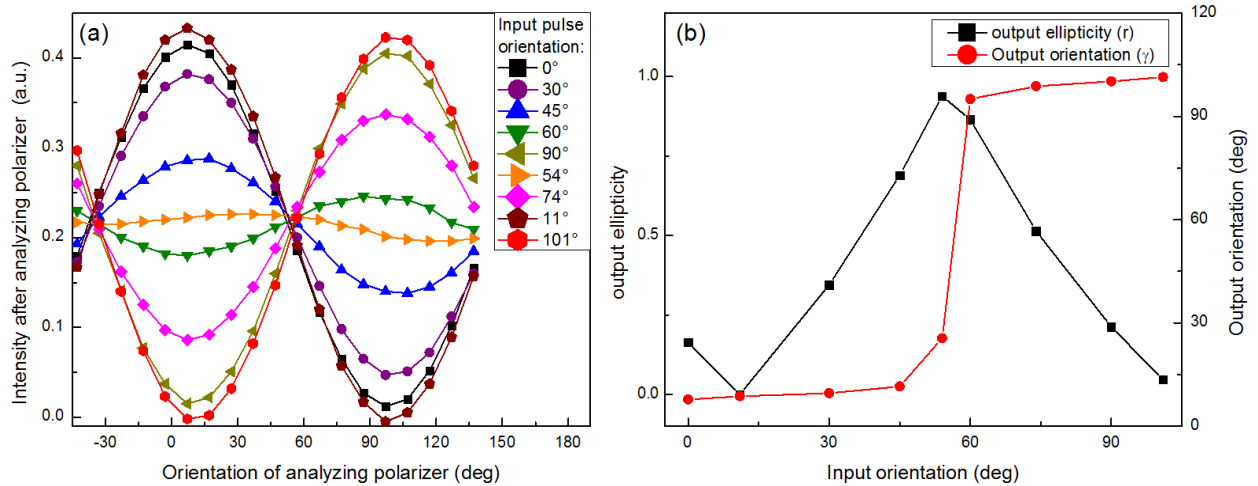


Figure 4.2: Polarization after the fiber for linearly polarized input pulses with different orientations. (a) Intensity after an analyzing polarizer depending on its angle for different input orientations. (b) Retrieved output orientation and ellipticity depending on the input pulse orientation.

and a retardation plate with a certain retardance and orientation [35]:

$$\mathbf{J}_{fiber} = \mathbf{J}_{rot}(\alpha)\mathbf{J}_{rot}(\beta)\mathbf{J}_{ret}(\phi)\mathbf{J}_{rot}(-\beta). \quad (4.2.1)$$

The two linear polarization states oriented at β and $\beta + \frac{\pi}{2}$ to the horizontal remain linear after transformation by this matrix. They are rotated by the angle α and acquire phases differing by ϕ .

To confirm that this is a good description of the fiber that was used in the experiment, the dependence of the output on the input polarization state has to be characterized. In the first measurement, linearly polarized pulses with different orientations, obtained by passing the beam through a rotating half wave plate, were coupled into the fiber and the output polarization state was characterized using an analyzing polarizer and a photodiode. The results are presented in fig. 4.2. The dependence of the output polarization on the input orientation is consistent with the model described above for the values $\alpha = -61^\circ$, $\beta = 11^\circ$ and $\phi = (2n + 0.48)\pi$. The latter is slightly surprising. The birefringence of a fiber is usually described in terms of polarization beat length $L_b = 2\pi L/\phi$, where L is the fiber length and ϕ the acquired phase difference between two orthogonal modes. Even if $n = 0$, $\phi = 0.5\pi$ corresponds to a beat length of about 4 m, while the value given by the producer of the fiber is 100 m. Possible reasons for this large birefringence can be additional mechanical stress induced by the FC connectors or torsion caused by an unintentional twist of the fiber.

In the majority of experiments presented in this work linearly polarized pulses were used. Before coupling into the fiber, they were rotated with a HWP to coincide with the principal axes of the phase retarder, for simplicity called fiber axes in the following.

A further measurement was performed to prove that it is possible to obtain arbitrarily oriented linearly polarized pulses after the fiber by applying an opposite polarization transformation before coupling the light into the fiber. This measurement was made especially easy by the fact that the retardance of the fiber corresponded to the retardance of a quarter wave plate (QWP) which was readily available in the lab (otherwise a wave plate specially designed for this purpose would have to be used). First, the beam passed through a QWP rotated by θ . Then a HWP rotated it by the angle $\beta - \theta$ so that the principal axes of the polarization ellipse coincided with the principal axes of the fiber. As the retardances introduced by the fiber and the QWP cancel each other, the result is a rotation by an angle $\alpha + \beta - \theta$.

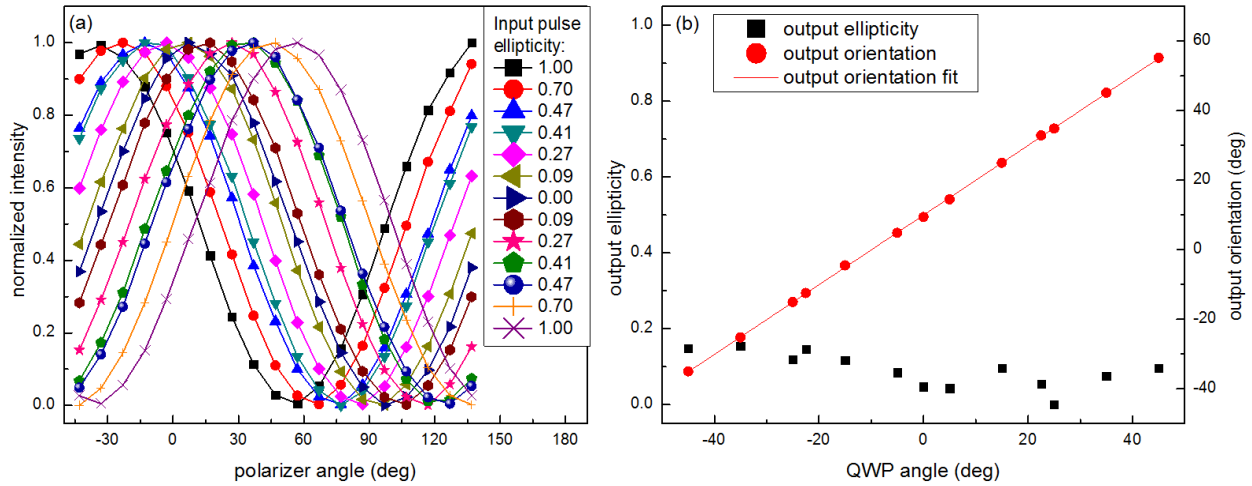


Figure 4.3: Polarization after the fiber for elliptically polarized input pulses with principal axes parallel to the fiber axes and different ellipticity obtained by changing the QWP angle. (a) Intensity after an analyzing polarizer depending on its angle for different input orientations. (b) Retrieved output orientation and ellipticity depending on the QWP angle.

Results of this measurement are shown in fig. 4.3. As expected, the output pulses are close to linearly polarized and their orientation depends linearly on the QWP orientation. This is a promising result. It leads to expect that it should be possible to control the polarization after the fiber with a set of variable phase retarders. Several experiments demonstrating such capability were performed by me and my coworkers Fabian Weise and Georg Achazi [69, 70]. I will present some examples in section 4.4. A more comprehensive description can be found in the doctoral thesis of Fabian Weise [39].

4.3 Chromatic dispersion and nonlinear effects

4.3.1 Pulse width and duration measurements

To get an idea about the influence of the fiber dispersion and nonlinear refractive index on the pulse shape a series of measurements was performed. Oscillator pulses with 23 nm spectral width centered at 780 nm were used. The pulse energy was varied by placing neutral density filters before the fiber. The maximal pulse energy achievable in this configuration was 0.46 nJ. The linear chirp was varied with the shaper. All measurements were performed with linearly polarized pulses rotated with a HWP so that they remained linear during the propagation.

In fig. 4.4 the dependence of the output pulse spectral width on the input pulse linear chirp is shown. As expected, there is a significant change in the spectral width in two regions. For linear chirp close to zero, corresponding to a short pulse at the fiber input, spectral broadening can be observed. On the other hand, for values around -50000 fs^2 a significant narrowing is visible. It can be supposed that this value corresponds to a short pulse at the fiber output. This behavior is consistent with predictions in sec. 2.4.3. Of course, for chirp values between 0 fs^2 and -50000 fs^2 self-phase modulation takes place as well, but in this regime the pulse spectrum experiences first narrowing and then, as it acquires a quadratic spectral phase due to the fiber dispersion, broadening, so the net effect of SPM on the spectral width is small. Outside this range the pulse remains long during the whole propagation, so only a little or no spectral width change is expected. This is,

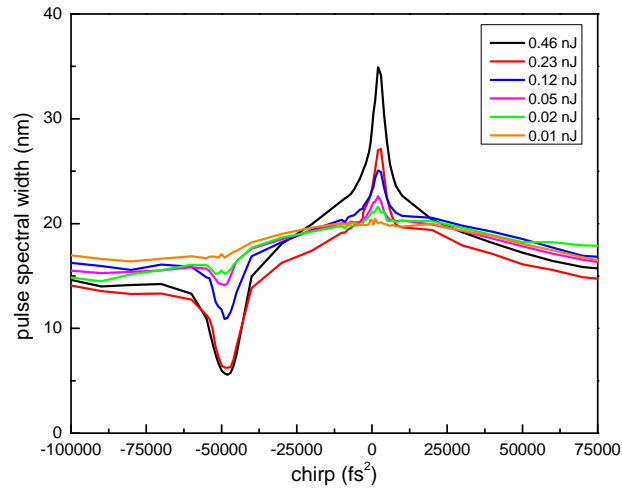


Figure 4.4: Measured output spectral width for different pulse energies depending on the chirp of the input pulse.

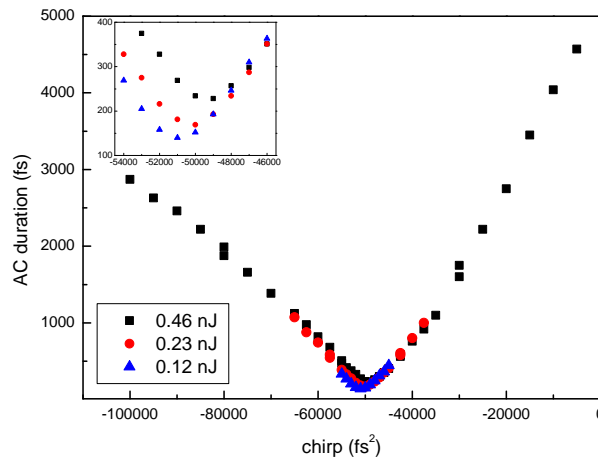


Figure 4.5: Measured output autocorrelation width for different pulse energies depending on the chirp of the input pulse (inset: magnification).

however, not exactly the case: even for the smallest pulse energy the input spectral width of 23 nm is never achieved. This can be attributed to the space-time coupling.

Next, a series of autocorrelation measurements was performed. The results are presented in fig. 4.5. Due to the limited sensitivity of the autocorrelator the measurements could not be performed for all pulse energies. In addition, as the pulse energy was decreased, only the shorter pulse durations corresponding to the higher peak powers could be measured. However, one can still make some observations. First of all, the autocorrelation measurements confirm that the linear chirp of -50000 fs^2 corresponds to a short pulse after the fiber. Secondly, the influence of the SPM on the pulse spectral phase is visible. As the pulse energy increases, the minimum position shifts.

4.3.2 Simulations and fiber dispersion measurement

Parallel to the measurements a series of simulations was performed to check not just the qualitative, but also the quantitative agreement with the theory.

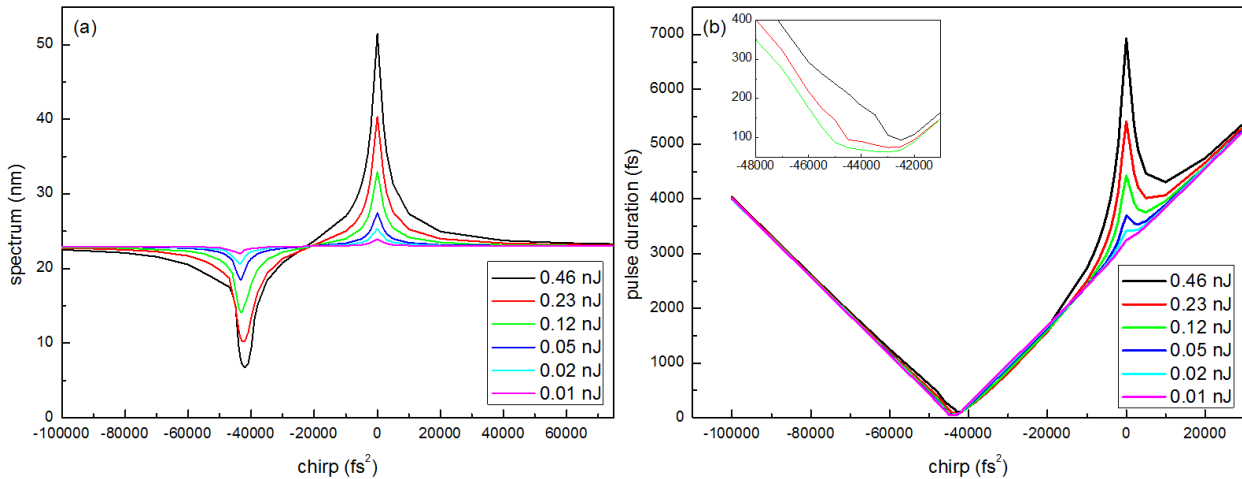


Figure 4.6: Simulation of the influence of the fiber dispersion and nonlinear effects on (a) the pulse spectrum and (b) duration depending on the input pulse chirp. The simulation was performed using the parameters for bulk silica.

All fiber propagation simulations in this work were performed using LabVIEW. The split-step routine for simulating the propagation was taken from the Lab2 package [71]. However, in many cases some adjustments, for example of the sampling or phase wrapping, were necessary. This was done by dividing the whole fiber into 20-50 parts of equal length and then using the fiber subroutine (`optical_fiber.vi`) or in some cases, the nonlinear element subroutine (`transparent_nonlinear_medium.vi`) provided by Lab2 in a loop, making adjustments after each iteration if necessary.

The Lab2 package contains a database of the linear and nonlinear properties of the most common optical materials that can be used as input for the simulation. Seeing that the fiber used for the measurements is made of fused silica, I performed a series of simulations using these parameters. The results are presented in fig. 4.6. There is a good qualitative agreement with the measurements presented in figures 4.4 and 4.5. However, a more careful look reveals several differences. First of all, the minima of both spectral width and pulse duration are shifted with respect to the measurement by several thousands fs^2 . Secondly, there is more spectral broadening for the short input pulse.

Moreover, it should be noted that fig. 4.5 shows the autocorrelation duration, while fig. 4.6(b) shows the pulse duration. For a Gaussian temporal shape the ratio between the autocorrelation duration and pulse duration is about 1.4. This means that the measured pulse duration for large chirp values is not well reproduced by the simulation. This is, however, not surprising. As the prechirp is increased, space-time coupling causes spectral narrowing. A spectrally narrow pulse experiences less dispersion and thus less temporal broadening. To improve the results, one would have to measure the dependence of the spectral width on the prechirp (using a strong neutral density filter and preferably a glass block as stretcher as well) and then repeat the simulation assuming a different spectral width for each point.

Space-time coupling cannot explain the discrepancies in the spectral width simulation and measurement. There can be several reasons for them. Such a high error in the shaper calibration is unlikely - it would show up in other measurements as well, particularly polarization shaping. More likely, the input parameters are not equal to the actual fiber parameters.

First of all, as explained in 2.1.3, the chromatic dispersion of a fiber contains a waveguide contribution which is obviously not contained in the database entry for fused silica. Calculations

wavelength (nm)	measurement		bulk fused silica	
	β_2 (fs ² /mm)	β_3 (fs ³ /mm)	β_2 (fs ² /mm)	β_3 (fs ³ /mm)
780	46.7	137	37.8	27.0
805	41.0	153	35.8	27.8

Table 4.1: The results of the dispersion measurements for the SM750 fiber compared to the values for bulk fused silica.

[72, 73] as well as the measurement for a similar fiber included in [74] indicate that in the near infrared this contribution has the same sign as the material dispersion. This means that more chirp is required to obtain a short pulse after the fiber than after a block of fused silica of the same length. This is consistent with the measurements.

To my knowledge there is no exact data for the fiber used in this experiment so I decided to measure the dispersion of the fiber myself using a method first described in [74]. In this method the spectral phase of a pulse entering the fiber is shaped so that the pulse length after propagation through the fiber is minimized. The pulse length can be measured with an autocorrelator, but a simpler and faster method is to maximize the signal from a nonlinear detector such as thin second harmonic generating crystal or, in my case, a GaAsP diode which has no one-photon absorption at 800 nm. The second derivative of the optimal spectral phase obtained in this procedure is related to the GVD of the investigated fiber by the relation $\varphi''(\omega) = \beta''(\omega)L$, where L is the fiber length. β_0 and β_1 cannot be determined by this procedure, but they are not needed for simulating the propagation. The advantage of this method is that dispersion properties are measured exactly in the spectral range that the laser pulse is covering. On the other hand, if the central wavelength of the pulse is changed significantly, the measurement has to be repeated.

Results of the dispersion measurement are presented in Table 4.1. $\beta_2(\omega)$ is expressed using the first two Taylor terms. I verified that by adding further phase terms in the optimization the pulse length is not reduced further, so two terms are enough to describe the pulse phase. For this measurement the pulse energy was reduced using a neutral density filter to suppress nonlinear effects. As expected, the measured GVD is about 10% greater than the value for bulk fused silica which is consistent. Also the TOD is significantly different from this of bulk fused silica.

Next, a new simulation was performed using the measured dispersion values. For this purpose a new subroutine was written that converted $\beta_2(\omega)$ into $n(\lambda)$ required by Lab2. The results are shown in fig. 4.7. Several differences can be seen. First of all, the minimal spectral width is achieved for the same chirp value as in the measurement. Secondly, there is less spectral broadening for pulses with no input linear chirp, which is also consistent with the measurement. A probable reason is that the measured dispersion of the fiber is bigger than that of fused silica, so its influence on the pulse relative to this of SPM is also bigger.

However, the broadening in the new simulation is still greater than in the measurement. One reason for this can be that contrary to the simulation the phase of the pulse in the measurement was not perfectly flat because of experimental imperfections. Another explanation is that the value of the nonlinear refractive index n_2 assumed in the simulation differs from the actual value. This will be discussed in more detail in sec. 6.2.

Another difference is the characteristic feature in the pulse duration plot for the linear chirp about -50000 fs^2 . It can be explained by the TOD. In the simulation only the GVD was compensated, so the pulse with prechirp roughly equal to the quadratic phase shift caused by the fiber will have only a small quadratic phase, but a large third-order phase after the fiber. In this case wings appear in the temporal profile of the pulse and the FWHM is not a good measure of the pulse du-

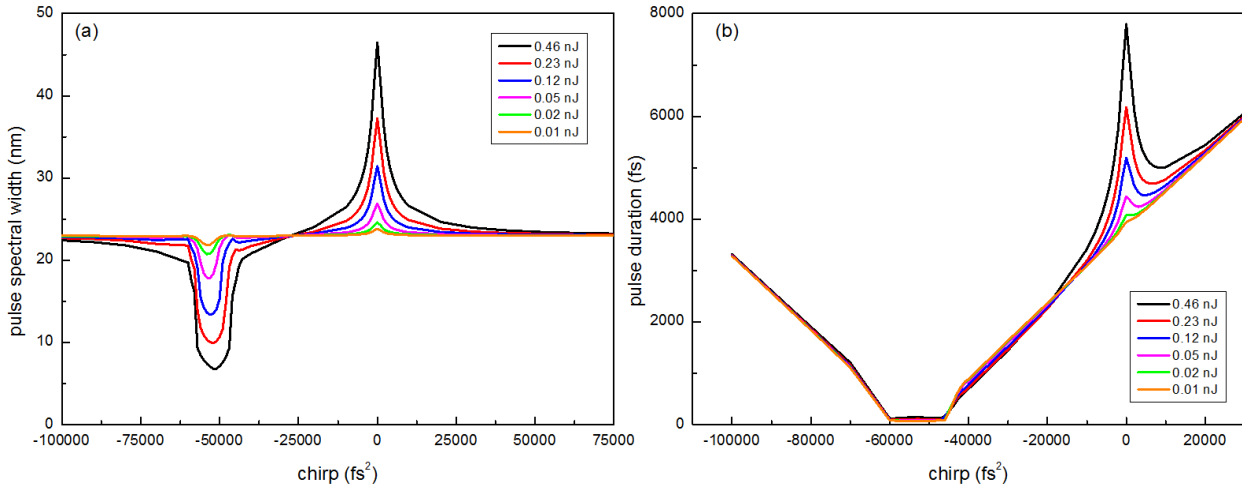


Figure 4.7: Simulation of the influence of the fiber dispersion and nonlinear effects and the pulse spectrum and duration depending on the input pulse chirp. The simulation was performed using dispersion values determined with a measurement.

ration anymore. A more suitable quantity would be for example square root of the second central moment, or simply speaking the standard deviation of the intensity distribution from the central wavelength. The standard deviation (not shown) behaves qualitatively the same as the measured autocorrelation, that is increases and shifts towards smaller values of chirp with increasing pulse energy.

4.4 Parametrically shaped pulses in the linear regime

Before attempting to transport shaped pulses through the fiber in the nonlinear regime, the capability of transporting shaped pulses in the linear regime should be verified. In order to do that, a series of experiments were performed with two shaper setups: the two-shaper setup capable of phase, amplitude and restricted polarization shaping shown in fig. 3.5 on page 28 and the three-shaper setup capable of full polarization shaping described in [39]. In this section some examples of measurements made with the first of these two setups are presented as full polarization shaping is not the focus of this work. For a more detailed description of the measurements done with both polarization shaping setups see [39].

In all measurements presented in this section the spectral width of the pulse was 23 nm (limited by the size of the SLM-128 shaper) and the pulse energy was 10 pJ. As can be seen in fig. 4.4, for this pulse energy the nonlinear effects are negligible.

4.4.1 Short pulse

In this section the capability of generating single short pulses after transmission through the fiber is demonstrated. Fig. 4.8 illustrates the importance of dispersion compensation. In fig. 4.8 (a) the cross-correlation trace of a pulse with no dispersion compensation is shown. After propagation through the fiber the pulse is stretched to about 3.5 ps. In fig. 4.8 (b) the relative importance of the second and third order dispersion can be seen. The pulse with only second order dispersion (or linear chirp) compensation is already quite short. However, the asymmetric temporal shape

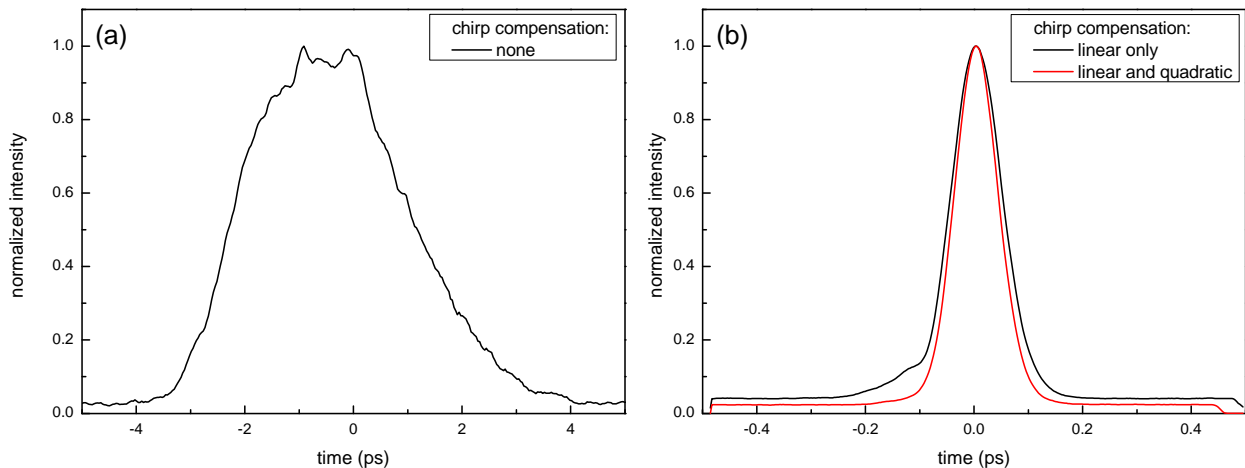


Figure 4.8: Cross-correlation of the pulse after the fiber (a) without dispersion compensation and (b) with compensation for linear chirp (black) and linear as well as quadratic chirp (red).

indicates that higher order dispersion is present. If a quadratic prechirp is applied as well, the pulse becomes symmetric as the cross correlation length is 95 fs.

In section 4.2 I have already shown that it is possible to obtain linearly polarized light after the fiber. The next step is to verify that a combination of dispersion and birefringence compensation indeed yields short pulses with controllable ellipticity. First, the fiber retardance was determined again, this time using the pulse shaper. This was done by generating a circularly polarized pulse. The value that was found in this measurement, 0.42π , is in quite good agreement with the value 0.48π found by the measurement presented in 4.2 on page 39. In all subsequent experiments presented in this chapter 0.42π was used as the birefringence compensation.

In the two shaper setup the polarization is controlled by the second modulator. The mechanism is the same as in the case of a single modulator described in sec. 3.2.1. The only difference is that in 3.2.3 on page 23 the phase retardances of the first modulator φ_a and φ_b have to be replaced with the phase retardances of the second modulator φ_c and φ_d .

Fig. 4.9 shows a series of short pulses with varying ellipticity characterized using three dimensional XC. In fig. 4.9(a) a linearly polarized pulse is shown, in fig. 4.9(b) an elliptically polarized pulse and in 4.9(c) a circularly polarized pulse. For the measured ellipticity values see the figure caption. The coordinate system is rotated by -61° with respect to the horizontal axis which is visible in the measured orientations of the linear and the elliptical pulse. Finally, all pulses have a Gaussian temporal envelope corresponding to a pulse duration of about 70 fs which is close to transform limited.

4.4.2 Complex pulse trains

In the last section single polarization shaped pulses generated by phase shaping and adding a polarization offset were shown. Here I will demonstrate that it is also possible to obtain after propagation through the fiber complex pulse sequences with shaped phase, amplitude and polarization. Like before, the pulses were characterized using three dimensional XC.

In fig. 4.10 a systematic ellipticity control of one pulse in a two pulses sequence is shown. While the second pulse stays horizontally polarized, the polarization of the first one is varied from vertical through elliptical with one helicity to horizontal and then again through elliptical with the opposite helicity to vertical. Here, difference retardance $\Delta\varphi$ is shown instead of helicity. The two are connected by the relation (analogous to expression 3.2.3 on page 23):

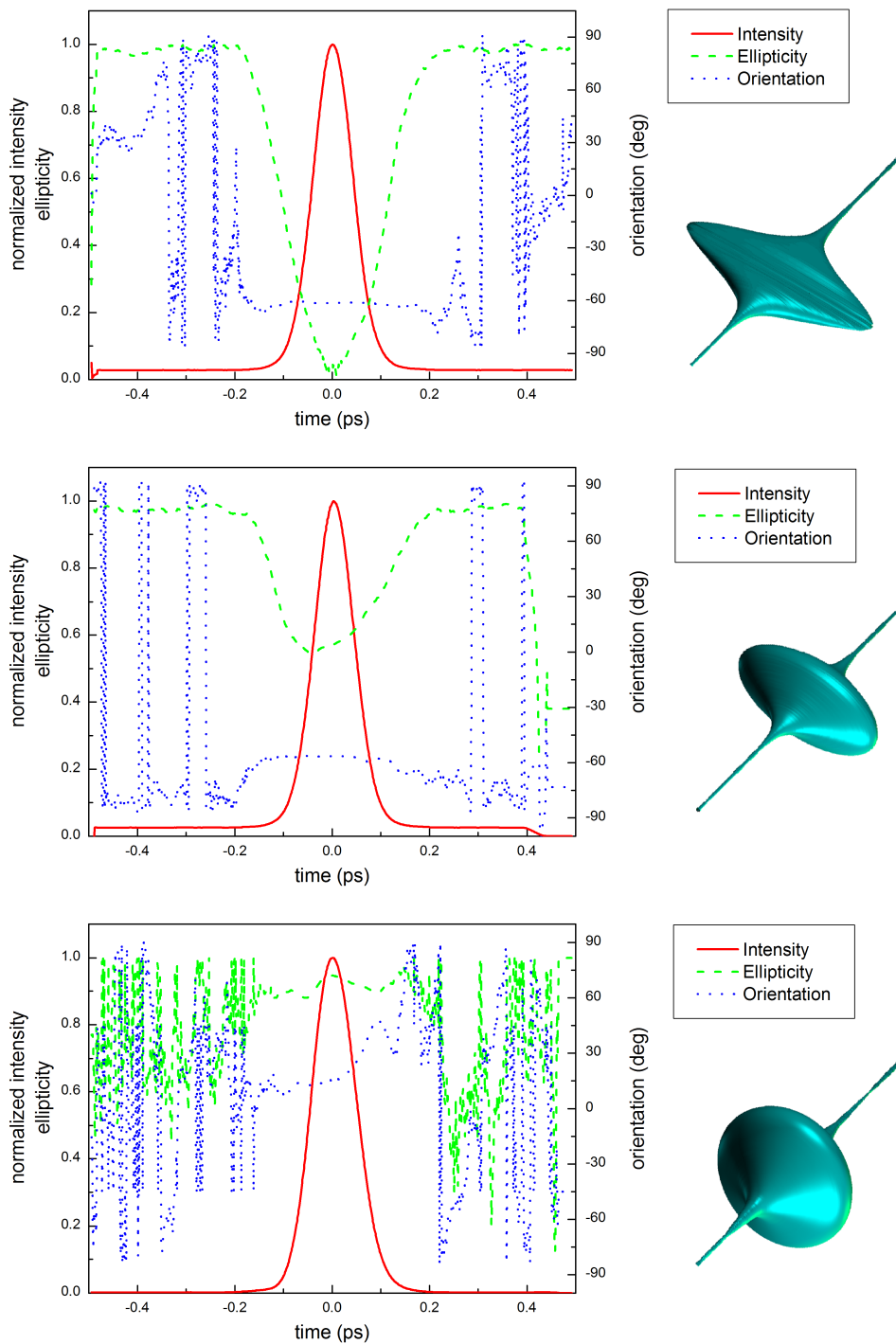


Figure 4.9: Short polarization shaped pulses after the fiber. On the left, the time-dependent normalized intensity (red), ellipticity (green) and orientation (blue) are plotted. On the right, a three-dimensional representation of the pulse is shown. (a) A linearly polarized pulse (set $r = 0$, measured $r = 0.04$), (b) an elliptically polarized pulse (set $r = 0.5$, measured $r = 0.55$) and (c) a circularly polarized pulse (set $r = 1$, measured $r = 0.94$) are shown (note that the parameters vary with time - the given values are for $t = 0$; the measurement error is estimated to be $\Delta r = \pm 0.03$ [39]).

$$r = \min(\tan(\Delta\varphi/2), \cot(\Delta\varphi/2)). \quad (4.4.1)$$

The set and measured parameters (fig. 4.10(a)) are in good agreement and the pulses remain short (fig. 4.10(a), (b) and (c)).

In fig. 4.11 more complex pulse sequences are presented. Here not only the ellipticity, but also distance, energy and chirp of the subpulses in three pulses sequences are varied. There are too many control parameters to vary them all systematically, but the examples presented here are enough as a proof of principle and give a good idea about the capability of the method.

In the presented examples some of the limitations of the shaper setup can be seen as well. In some cases unintended side pulses appear. In the three pulse sequences with equal set pulse energy the central subpulse has in fact a slightly higher intensity which is a result of the shaping window. Some deviations from the intended ellipticity values are also visible.

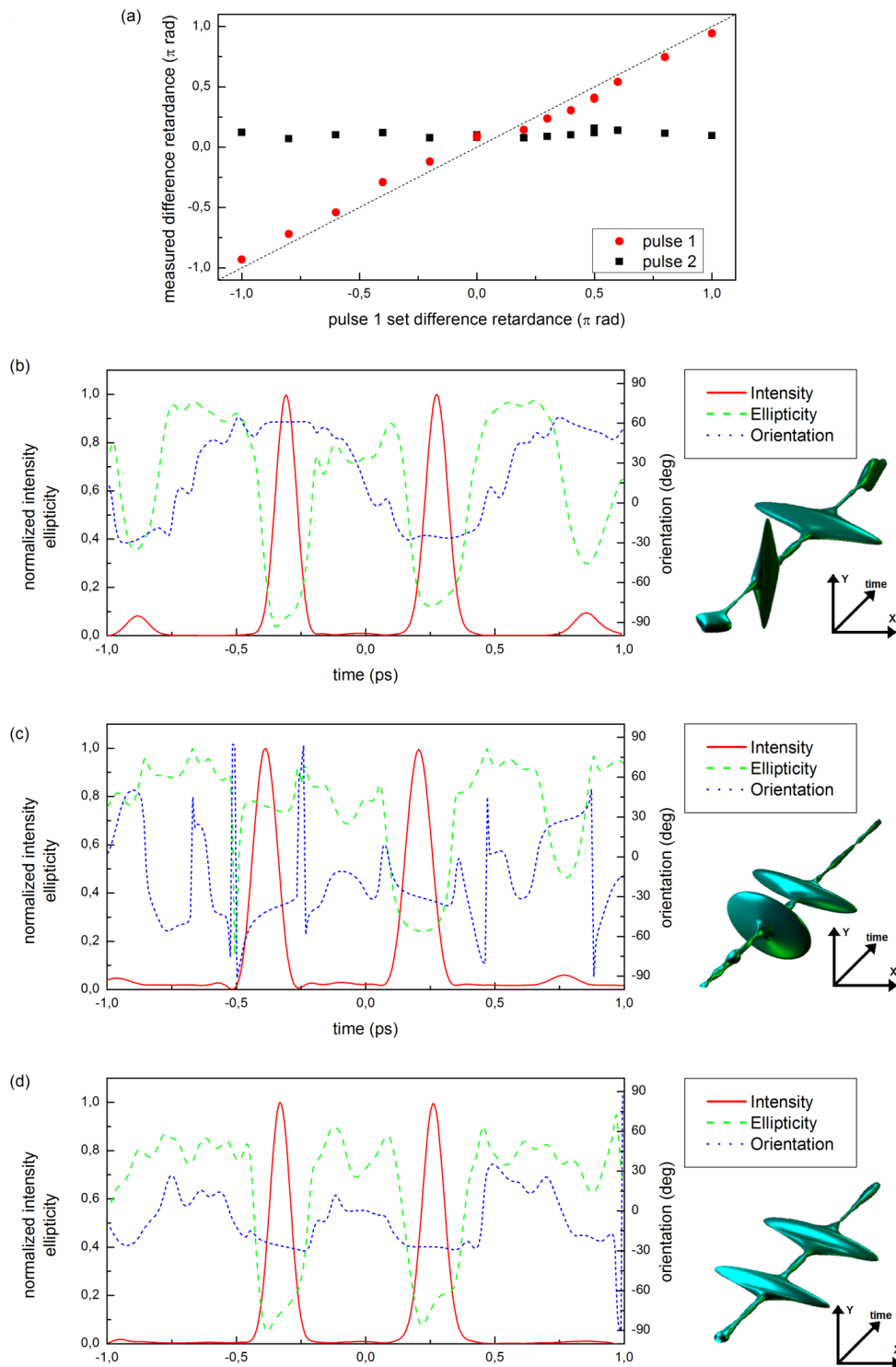


Figure 4.10: Control of polarization in a double pulse sequence. The ellipticity of the first subpulse is varied while the second subpulse stays linearly polarized. In (a) measured difference retardance of both subpulses is shown. (b), (c) and (d) show examples of characterized pulses. On the left the time-dependent intensity, ellipticity and orientation are plotted and on the right reconstructed three-dimensional representation of the pulse is shown. The set difference retardance of the first subpulse is 1.0π (linear vertical polarization) in (b), 0.5π (circular, right-handed) in (c) and 0.0π (linear horizontal) in (d).

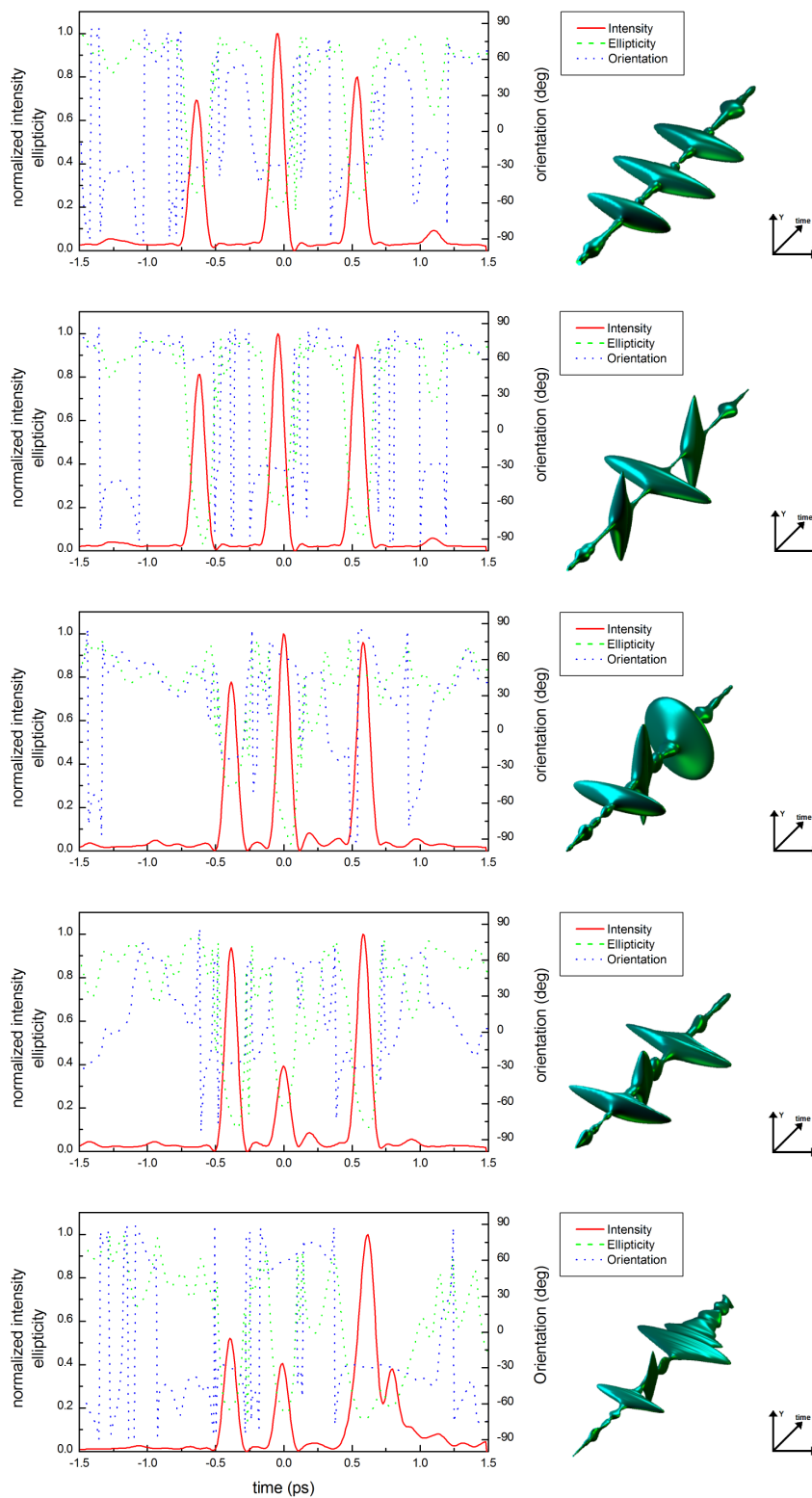


Figure 4.11: Examples of complex pulse sequences: (a) three subpulses separated by 600 fs, (b) same as (a), but the first and the third subpulses are now vertically polarized, (c) distances changed to 400f and 600 fs and the last subpulse is circularly polarized, (d) the energy of the central subpulse reduced by one half and (e) the last subpulse has a quadratic chirp of $8 \times 10^5 \text{fs}^3$ and three times larger energy than the other two.

Coherent control of two-photon transitions

5

In section 2.3.3 I have explained how narrow two-photon (TP) transitions can be efficiently excited not only with transform limited, but also with phase-shaped pulses. In this chapter I will investigate the possibility of generating such phase-shaped pulses that after transmission through an optical fiber in the nonlinear regime can still efficiently and selectively excite TP transitions.

The experimental setup for measurements presented in this chapter is shown in fig. 5.1. It consists of elements already described in chapters 3 and 4: a laser system generating pulses centered at 780 nm, a $4f$ setup with one SLM, a step index fiber and BBO crystals. As described in section 3.4.1, the measurements were performed with two different BBO crystals, a thick one (corresponding to a narrow transition) and a thin one (corresponding to a broad transition). A dichroic mirror was used to separate the SH signal from the fundamental. The pulse energy was between 0.15 nJ and 0.7 nJ. A HWP and a polarizer were placed before the fiber to regulate the intensity of the beam. For this the orientation of the polarizer was fixed and the HWP was rotated to adjust the fraction of the beam intensity rejected by the polarizer. The advantage of this method is that day-to-day changes of the laser intensity can be compensated for by slightly changing the wave plate angle which is difficult to do with a set of neutral density filters.

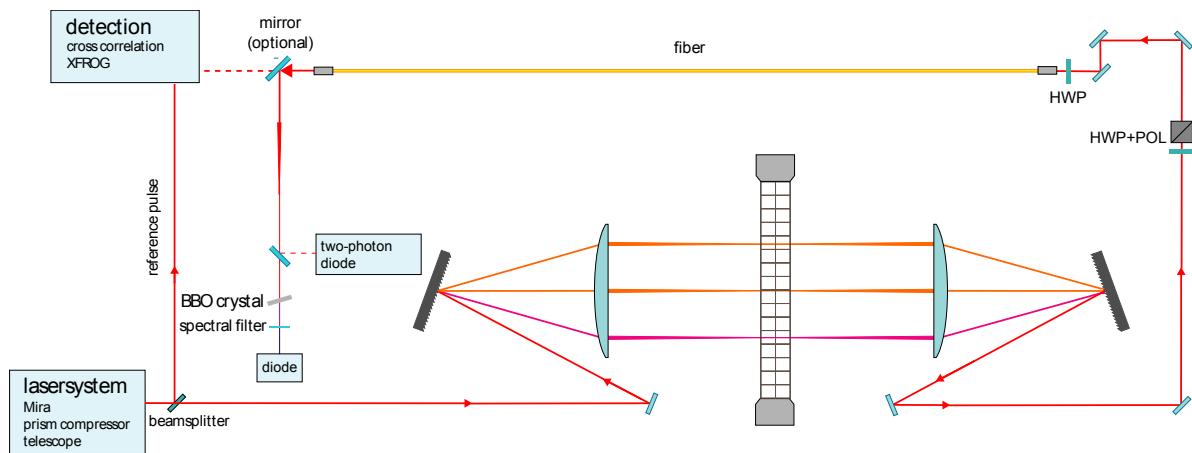


Figure 5.1: Experimental setup for coherent control of TP transitions with pulses transported through the fiber: the laser beam passes the shaper setup, a HWP and a polarizer (POL) are used to regulate the intensity and a second HWP rotates the polarization so that it coincides with an optical axis of the fiber. After the beam passes through the fiber the efficiency of SHG in a BBO crystal is measured with a photodiode.

5.1 Preliminary measurements

5.1.1 Measurements without fiber

The experiments in this chapter concern coherent control with shaped pulses that experience additional phase and amplitude modulation due to self-phase modulation in an optical fiber. To

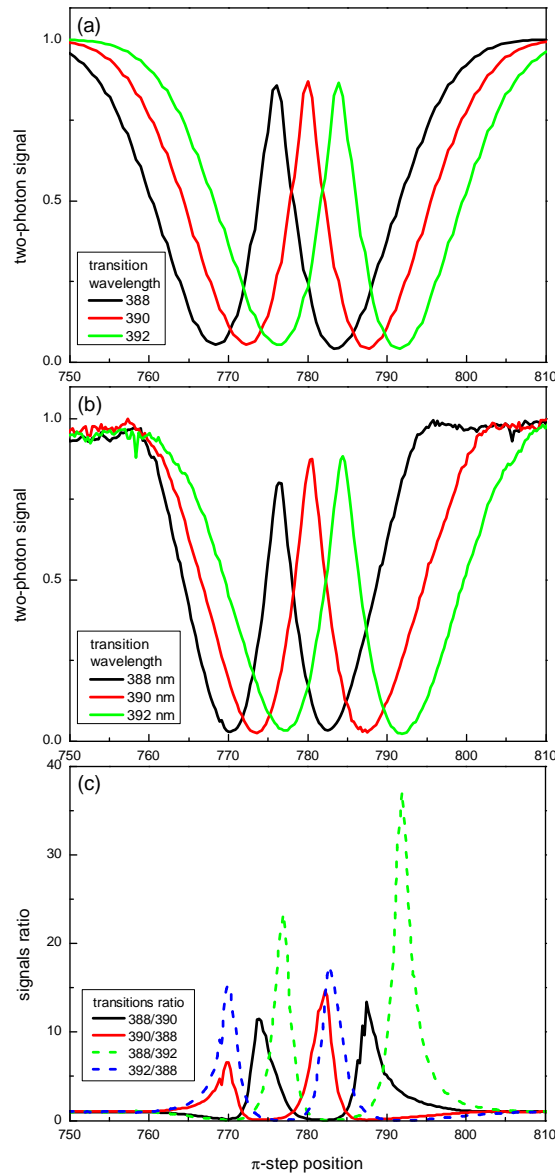


Figure 5.2: Control of narrow transitions using pulses with a phase with shifting π step (without fiber). (a) Simulated and (b) measured SH intensity for different transition wavelengths depending on the π step position. (c) Ratios of measured signals.

understand the influence of the nonlinear effects on the results of the experiment, it is necessary to get an idea about the limitations caused by other factors. For this purpose reference measurements without the fiber were performed first. The results are presented in this section.

First, coherent control of SHG in a thick crystal with pulses with a π step spectral phase according to the principle explained in sec. 2.3.3 is demonstrated. The simulated (fig. 5.2(a)) and measured (fig. 5.2(b)) second harmonic intensity is shown depending on the position of the π step. To test the capability of selective excitation of a chosen transition, the signal was measured for three second harmonic frequencies, one coinciding with the doubled central frequency of the pulse and two slightly detuned, obtained by rotating the crystal. The signal is normalized with the short pulse signal for the respective transition. Without the normalization the signal for the detuned transitions is lower than the one for 390 nm, simply because there are less possible photon pairs in the pulse spectrum that have the right total energy. Fig. 5.2(c) shows the ratios between

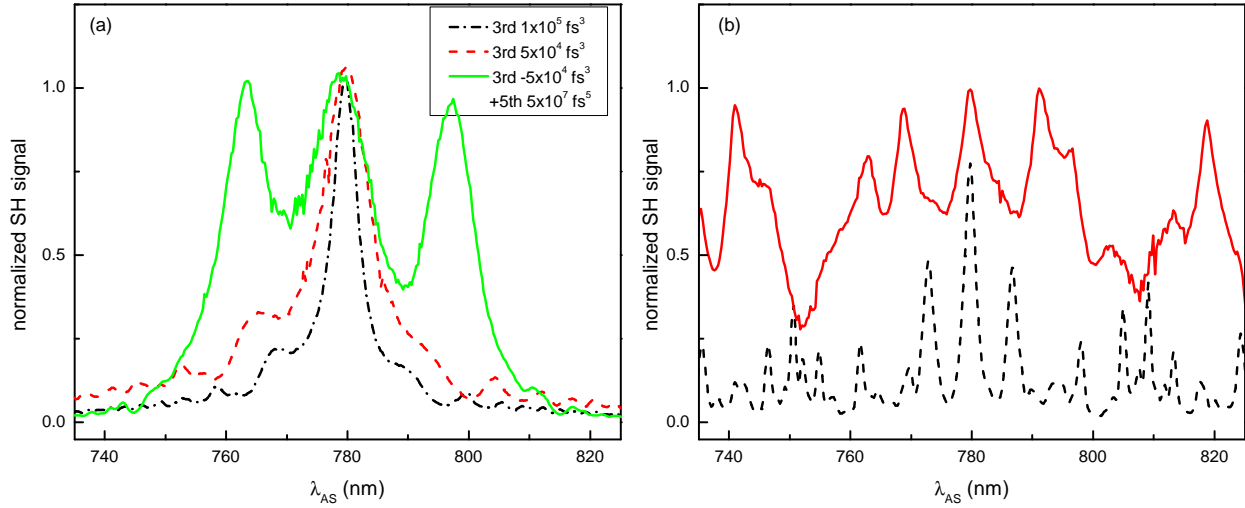


Figure 5.3: Measured SH intensity for $\lambda_T = 390 \text{ nm}$ obtained with pulses with spectral phase anti-symmetric around λ_{AS} . The signal dependence on λ_{AS} is shown for (a) three different polynomial phase functions and (b) two different randomly generated antisymmetric phase functions.

different signals (for clarity, only four out of six curves are shown). Because of the normalization the ratio for a short pulse (π step outside the pulse spectrum) is one.

The selectivity of the excitation of two transitions can be described by the contrast factor defined as

$$\Gamma = \frac{R_{max} - R_{min}}{R_{max} + R_{min}}, \quad (5.1.1)$$

where R_{max} and R_{min} are the biggest and the smallest achieved ratios of absorption (or emission, depending on which is the observable in the experiment). The values of Γ lie between zero and one, zero meaning no contrast (both transitions equally efficiently excited) and one maximal contrast (only one of the two transitions excited). Because Γ is defined as a ratio of linear combinations, it is independent from signal normalization. For all the transition pairs in fig. 5.2(c) Γ is at least 0.98, which means that almost perfect selectivity can be achieved. This is possible due to the existence of dark pulses (see sec. 2.3.3).

The π step is just an example of an antisymmetric function that can be used to excite a TP transition; some other are presented in fig. 5.3. In all cases the phase function is antisymmetric around a certain wavelength λ_{AS} . The SH signal is measured depending on λ_{AS} and reaches a maximum when λ_{AS} is exactly twice the transition wavelength λ_T , that is, when the phase is antisymmetric around $2\lambda_T$. In fig. 5.3(a) some examples of polynomial phase functions are shown. For $\lambda_{AS} = 2\lambda_T$ all three functions result in the same excitation efficiency as the TL pulse. One thing to note is the influence of the phase shape on the efficiency of excitation if $\lambda_{AS} \neq 2\lambda_T$: the steeper the function, the faster the signal decreases. The limit is mostly technical - at some point the slope of the phase will become too steep for generating it with the pulse shaper. This is an important observation if the purpose of phase shaping is selective excitation. Finally, 5.3(b) shows the signal obtained with two randomly generated phases. Again there is a maximum at $2\lambda_T$.

Another way of testing the effects of pulse shaping on TP transitions is to look at the second-order spectrum of the electric field as defined by eq. 2.3.16. Experimentally this corresponds to observing the second harmonic spectrum generated in a thin crystal. If the influence of phase matching is negligible, the SH spectrum depends only on the pulse phase.

Fig. 5.4 shows the spectrum of SH generated in a thin BBO crystal. As before, a π step spectral phase was used. It can be seen how the maximum of the SH spectral amplitude shifts with the π step position.

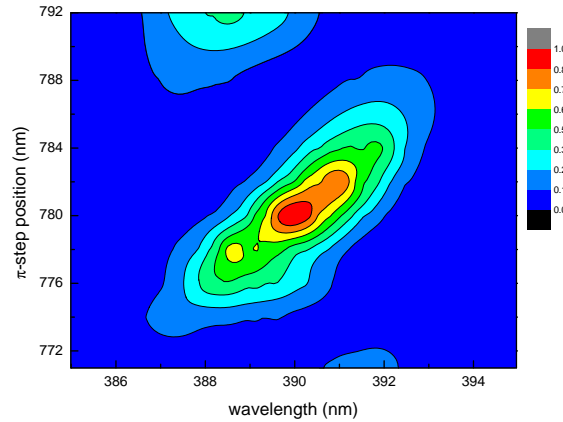


Figure 5.4: SH spectrum from a thin crystal corresponding to the second-order spectrum of the pulse depending on the π step position.

5.1.2 Antisymmetric phase after nonlinear propagation: proof of principle

In the previous section coherent control of SHG with pulses with antisymmetric spectral phase was demonstrated. The next question that I will answer is: are such pulses still capable of efficient excitation of two-photon transitions after their phase and amplitude was distorted during nonlinear propagation?

The measurements presented in fig. 5.5 on the facing page confirm that this is the case. The graphs show the normalized SHG efficiency for pulses with a π step spectral phase transported through the fiber. The measurement was repeated for two different pulse energies, 0.33 nJ and 0.66 nJ. As indicated by the measurements presented in sec. 4.3.1, for such pulse energies nonlinear effects play a significant role during the propagation in the fiber. Nevertheless, the results of the phase scan are qualitatively similar to those in fig. 5.2 on page 52: as the π step position changes, the signal first decreases and then increases again when the doubled transition wavelength is reached. To confirm that this behavior is (at least partly) due to the spectral phase shape, the normalized TP diode signal is shown as well. Indeed, the TP diode signal has no maximum at $2\lambda_T$. However, amplitude modulation plays a role as well. I will discuss it in more detail in the next section.

Although the pulse with a π step spectral phase is capable of exciting the narrow transition efficiently, the signal does not exceed one, that is the excitation efficiency is not greater than that of the short pulse. It would be more interesting to find such phase shaped pulses that after nonlinear propagation achieve a higher TP signal than the short pulses. The possibility of generating such pulses will be investigated in the next sections.

5.2 Optimization of the spectral phase

In this section I will present some experiments aimed at finding, by the use of genetic optimization algorithms, optimal pulses that excite two-photon transitions after transmission through the fiber.

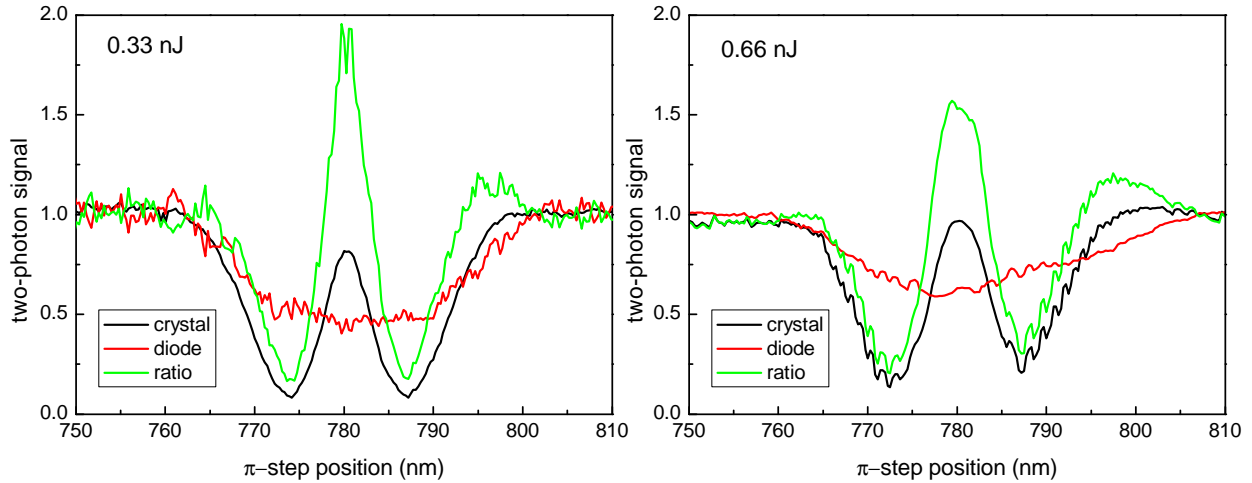


Figure 5.5: Excitation of a narrow (thick crystal tuned for SHG at 390 nm) and broad (diode) TP transition with pulses with a π step spectral phase after propagation in the nonlinear regime. In addition, the efficiency ratio is shown. The pulse energy was 0.33 nJ in (a) and 0.66 nJ in (b).

First I will focus on optimizing the excitation of a transition that coincides with the doubled central frequency of the pulse using single- and multi-objective algorithms. Then I will present some results concerning detuned transitions.

5.2.1 Single-objective optimization

Before searching for more complex pulse shapes, an offset phase yielding a TL pulse that can be used as a reference is needed. In the linear regime this is straightforward. As already explained in sec. 4.3.2, the required prechirp is the fiber dispersion multiplied by the fiber length.

In the nonlinear regime one has to compensate for the nonlinear dispersion as well, so the prechirp yielding a short pulse after the fiber has to be determined for each pulse energy separately. However, if a TP diode is used as a feedback signal, it is not a priori clear that there is a unique solution. The spectral amplitude of the output pulse depends on the phase of the input pulse, so one can imagine that for a given pulse energy it is possible to obtain different output pulses with slightly different spectral amplitudes yielding the same TPA signal. To exclude this possibility, the optimization was repeated many times to gather enough statistics. I have found that for the investigated pulse spectrum and energies there was always only one optimum. The results are shown in table 5.1.

Table 5.1: Prechirp yielding the shortest pulse for different pulse energies

pulse energy nJ	linear chirp fs^2	quadratic chirp fs^3
0.39	-5.39×10^4	1.81×10^5
0.59	-5.44×10^4	2.20×10^5
0.79	-5.32×10^4	2.18×10^5

Next, the thick crystal was set in the beam and rotated to generate second harmonic at the wavelength 390 nm and a series of optimizations of the SH signal was performed. Several phase

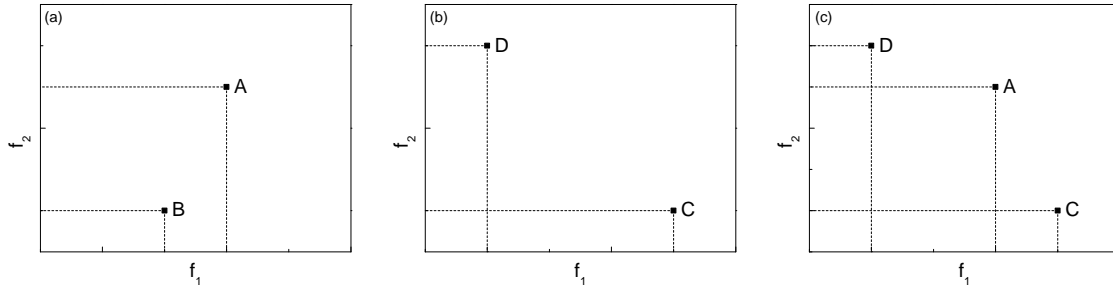


Figure 5.6: Forming the Pareto-optimal front out of solutions A, B, C and D: (a) A is better than B, (b) C and D are equally good, (c) so A, C and D lie on the Pareto-optimal front.

functions were used: a step with varying position and amplitude, a polynomial phase consisting of odd powers of the frequency, a linear combination of these two, and a sinus function with varying phase, amplitude and frequency. Each time the offset from table 5.1 was added. However, no solutions with higher SHG efficiency than the short pulse were found. This may mean that such solutions do not exist, but another possibility is that they are simply difficult to find because the efficiency is not significantly higher than that of the short pulse.

5.2.2 Multi-objective optimization

To investigate more systematically whether solutions performing better than the short pulse exist, another series of optimizations was done. This time the optimization goal was formulated differently: to find spectral phase functions that maximize the SHG in the thick crystal but do not correspond to short pulses, or in other words - do not maximize the efficiency of a broad TP transition simultaneously with a narrow transition. Technically it was done by dividing the beam after the fiber with a beamsplitter and measuring simultaneously two signals: the SH intensity and the TP photodiode signal that is inversely proportional to the pulse duration (see 3.3.4).

One thing that has to be considered before doing this kind of experiment is the optimization algorithm. At the first glance it seems that one can simply take a function of two signals s_1 and s_2 , for example the ratio s_1/s_2 , and use it as the fitness function in a single objective algorithm. For a single objective optimization the choice of fitness function is not so important; if $F(x)$ is a suitable fitness function, then any function $G(x)$ satisfying $F(x_1) \leq F(x_2) \Leftrightarrow G(x_1) \leq G(x_2)$ should work as well, although one has to remember that not all functions are equally robust in presence of noise. However, for multiple objectives there is, for example, a whole class of functions of the form

$$F(s_1, s_2) = s_1 s_2^{-w}, \quad (5.2.1)$$

where w is the relative weight of the two signals, $w = 1$ corresponding to the simple ratio. All these functions have the same goal, simultaneously maximizing s_1 and minimizing s_2 , but in general the optimization algorithm yields different solutions for different values of w .

The experiment described above is a typical multi-objective optimization problem. Such problems are found in many fields and numerous approaches to them are known. Describing them is beyond the scope of this work. I will concentrate on one - Weighted Sum Approach - and summarize it briefly. A more detailed description can be found in the doctoral thesis of Stefan Weber [75], who applied this method together with an evolutionary algorithm to coherent control of alkali dimers [76, 77].

The Weighted Sum Approach belongs to the class of so-called Pareto methods. The central concept in these methods is Pareto optimality, illustrated in fig. 5.6. Let us consider a two-dimensional search space consisting of two optimization goals, f_1 and f_2 , that should be maximized simultaneously. If a given point A in space is better than a given point B in both f_1 and f_2 , then B is dominated by A (see fig. 5.6(a)). On the other hand, if point D is better than point C in one dimension, but worse in the other, none of them is dominated (fig. 5.6(b)). The aim of the method is to find a set of solutions that are not dominated by any others. This set constitutes the Pareto-optimal front (fig. 5.6(c)).

In the Weighted Sum Approach with two goals, a general fitness function F is a sum of the partial fitness functions f_1 and f_2 with a weight w :

$$F(x) = f_1(x) + w f_2(x). \quad (5.2.2)$$

If the Pareto-optimal front is concave, each value of w will produce a different solution belonging to it, so by repeating the optimization for different values of w the whole front can be found [75].

To see how the Pareto-optimal fronts describing pulses that optimize excitation of a narrow transition with respect to a broad transition change with the pulse energy, a series of optimizations was performed. The fitness function had the form

$$F(s_1, s_2) = \log s_1 - w \log s_2, \quad (5.2.3)$$

where s_1 was the SH signal generated in the thick crystal and s_2 the two-photon diode signal. The search space consisted of polynomial functions of the form

$$\varphi(\omega_r) = b_1 \omega_r + \frac{1}{2} b_2 \omega_r^2 + \frac{1}{6} b_3 \omega_r^3 + \frac{1}{5!} b_5 \omega_r^5 + \frac{1}{7!} b_7 \omega_r^7 + \frac{1}{9!} b_9 \omega_r^9 + \frac{1}{11!} b_{11} \omega_r^{11}, \quad (5.2.4)$$

where $\omega_r = \omega - \omega_0$ is the relative frequency. Eq. 5.2.4 describes an antisymmetric function with a small symmetric correction proportional to b_2 . The correction was added to compensate for the nonlinear dispersion that depends on the peak power and so it is different for each pulse energy.

The results are summarized in fig. 5.7. The axes are chosen in such a way that the solution with maximal fitness lies in the upper right corner. Each point corresponds to one value of w . The measurements show clearly that with increasing pulse energy the Pareto-optimal fronts shift in the direction of the lower left corner which means that it becomes more and more difficult to reach the goal.

To sum up, in the investigated pulse energy range no phase shaped pulses that excite the 390 nm transition more efficiently than the short pulse were found. Moreover, the direction in which the Pareto-optimal fronts shift does not indicate that such pulse shapes exist for larger pulse energies.

5.2.3 Optimization for different transition wavelengths

Although the solutions found by the optimization algorithm are not better than the short pulse, they are significantly different. This was confirmed by checking how well a shaped pulse optimized for a certain narrow TP transitions excites other transitions.

In order to do this, the pulse spectral phase was optimized using the standard single-objective algorithm for each crystal angle separately. The search space for the optimizations was the same as in the previous section, but with the coefficient b_1 in expression 5.2.4 equal to zero (this should have no influence as b_1 corresponds to the temporal shift of the pulse). For statistics each optimization was repeated three times and the best one was selected.

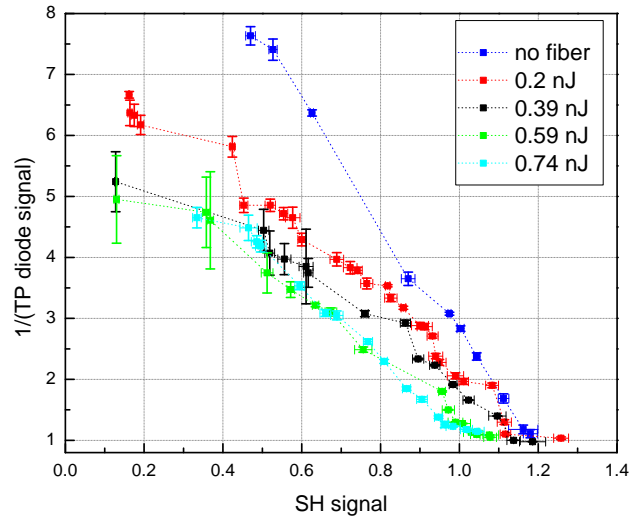


Figure 5.7: Optimization results: Pareto-optimal fronts for different pulse energies.

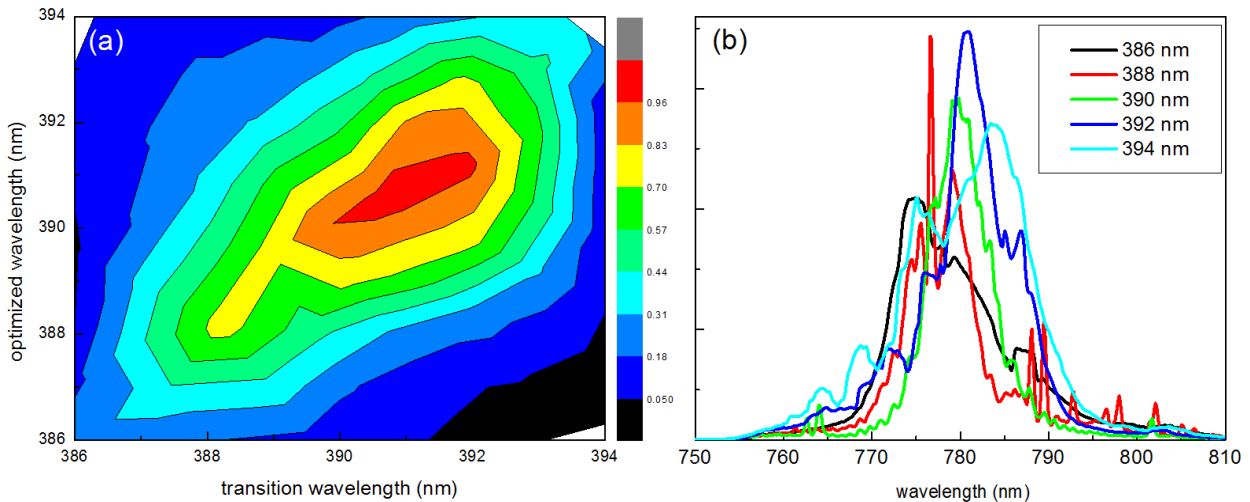


Figure 5.8: Excitation of other TP transitions with pulses optimized for a specific transition. (a) SH signal with pulses optimized for different transitions depending on the SH wavelength. (b) Pulses spectra after the fiber.

The results are shown in fig. 5.8(a). If the algorithm always converged to a nearly TL pulse, the signal would not depend on which SH wavelength was used as a fitness. However, this is clearly not the case. The pulses optimized for other wavelengths always perform worse than the pulse optimized for the given wavelength. This is promising for using phase-shaped pulses transported through a fiber for selective excitation, for example in microscopy.

Interestingly, in this case the selectivity is achieved not only by shaping the spectral phase, but also by an indirect modulation of the spectral amplitude. This is illustrated in fig. 5.8(b). It shows the spectra of the optimized pulses after transmission through the fiber. The maximum of the spectral intensity distribution shifts in the direction in which the two-photon transition is detuned and the amount of shift is roughly equal to the doubled detuning. The phase is not shown, as it is not possible to measure it with the spectrometer, but one can suppose that it also plays a role.

The effect discussed above leads to a question whether it is possible to design a spectral phase that would cause the pulse spectrum to shift due to nonlinear effects in the fiber. However, by

integrating the expression 2.4.14 on page 19 that describes the frequency shift caused by SPM one obtains that the frequency shifts sum to zero. The shape of the spectrum might change, but the spectral centroid (or the "center of mass") does not shift. This can be explained intuitively by energy conservation. If SPM is the dominating effect, then the nonlinear propagation can be explained by many three-photon processes and each time the total energy of the three photons stays the same. An actual shift of the spectrum is possible when Raman processes are involved as then a part of the energy is transferred to the lattice vibrations [1].

However, for controlling TP transitions it is not the pulse spectrum that matters but instead the two-photon spectrum as defined by eq. 2.3.16 on page 13. If one assumes for simplicity that the pulse emerging after the fiber has a flat phase, then what counts for the TP excitation is the centroid of $I^2(\omega)$ rather than $I(\omega)$. This can be indeed shifted (by 1 or 2 nm for the energies of the order of 1 nJ) by applying an appropriate spectral phase before the pulse propagates through the fiber. However, all my simulations indicate that in this case the pulse after the fiber does not have a flat phase, but, on the contrary, a phase that shifts the TP spectrum in the opposite direction than the squared amplitude is shifted. The resulting TP is a compromise between the two effects.

5.3 Selective excitation

The results presented in sections 5.1.2 and 5.2.3 indicate that it is possible to transport through the fiber in the nonlinear regime pulses capable of selective excitation of two-photon transitions. An optimization of the excitation ratio would require two identical thick crystals set at different angles, which were not available at the time of the measurement. Instead a different, more systematic approach was chosen. Different spectral phase functions were tested to find those that lead to efficient excitation only of selected transitions. The best results are presented in the following sections along with some simulations that explain why certain phase functions perform well in spite of modulation during nonlinear propagation.

5.3.1 Measurements with pulses with a π step spectral phase

In this section results obtained with the already mentioned π step spectral phase are presented. The π step was shifted pixelwise so that the wavelength λ_{AS} with respect to which the phase function was antisymmetric changed. Each measurement was repeated for three different BBO crystal angles and two different pulse energies.

The results are presented in fig. 5.9. Like in fig. 5.3 on page 53, each scan is normalized by the short pulse signal. The simulation in fig. 5.9(a) was performed in two steps. First the shaped pulse was propagated through the fiber as described in sec. 4.3.2, using the fiber dispersion determined experimentally. Then the efficiency of SHG (including phasematching but assuming negligible depletion and crystal GVD) for the output pulse was calculated. This was repeated for each π step position (about 100 steps). The simulation shows a good agreement with the measurement presented in fig. 5.9(b). The visible differences are due to experimental inaccuracies. In addition, the ratios between the measured signals for different SH wavelengths are shown in fig. 5.9(c).

Several differences between these measurements and those presented in fig. 5.3 can be seen. For the 390 nm transition the shaped pulse does not achieve the same efficiency as the TL pulse. However, for the detuned transitions the situation is different: for the pulse energy of 0.6 nJ the shaped pulse outperforms the TL one. A probable explanation is that the shaped pulse experiences less spectral narrowing. Another difference is that the dark pulses are less pronounced. This in turn causes a slight decrease of the contrast, which nevertheless stays above 0.9.

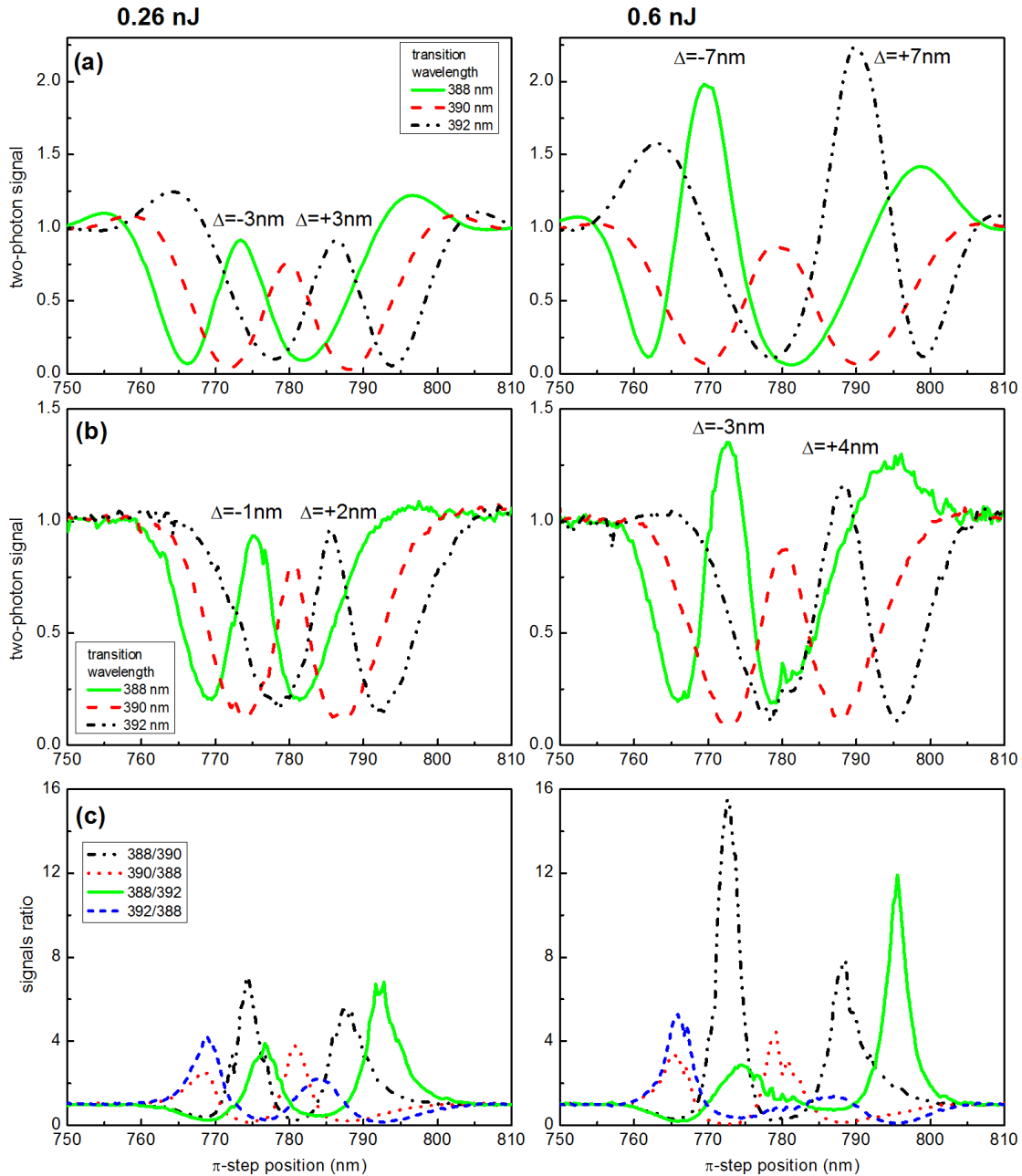


Figure 5.9: Excitation efficiency of narrow TP transitions with pulses with shifting π step in the spectral phase depending on the π step position for pulse energy 0.26 nJ (left column) and 0.6 nJ (right column) (a) Simulation. (b) Measurement. (c) Ratios of measured signals.

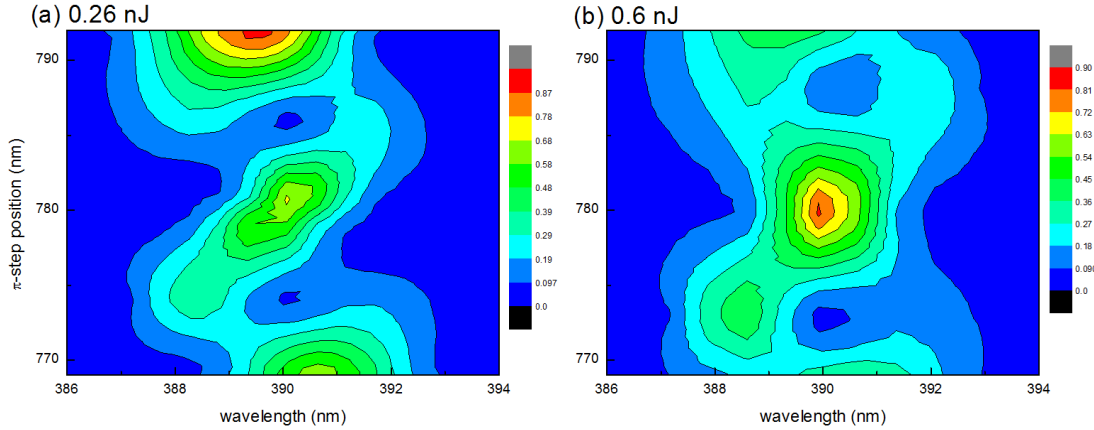


Figure 5.10: SH spectrum of a broad transition corresponding to the pulse TP spectrum depending on the π step position.

Finally, an interesting effect is visible: for a detuned transition at the wavelength λ_T the efficiency maximum does not lie at $\lambda_{AS} = 2\lambda_T$ but instead shifts outwards. The same effect can be seen if one looks at the minima instead of the maxima: they also shift outwards with pulse energy. This is apparent already in fig. 5.5 on page 55 which shows only the 390 nm signal. This apparent broadening can be explained intuitively by the SPM. Originally the π step is positioned at a certain wavelength $\lambda_{AS} \neq 2\lambda_T$ but moves towards the central wavelength of the pulse due to spectral narrowing and after propagation through the fiber the equality is satisfied. This simple picture is confirmed by simulations presented in the next section.

The SH spectra generated in the thin BBO crystal, representing second-order spectra, are presented in fig. 5.10. They show a similar behavior as the scans in fig. 5.9. The shape stays qualitatively similar as in fig. 5.4 on page 54 which shows the second-order spectra that are not influenced by nonlinear effects, but it gets deformed and the contrast worsens.

For measurements with oscillator pulses 0.7 nJ was the upper limit of the pulse energy in the experimental setup used in this section. To test the limits of selective excitation of TP transitions with pulses distorted by the SPM, a series of measurements with amplified pulses was performed. The pulses, centered at 792 nm, were attenuated with a neutral density filter so that the pulse energy in the fiber was 0.9 nJ. This is only a 30% increase of the pulse energy, but the efficiency of a three-photon process such as SPM scales with the third power of peak intensity, so for 0.9 nJ pulses the nonlinear effects in the fiber will be about twice as strong as for 0.7 nJ pulses.

As shown in 5.11(a), π step position scans were again performed for three narrow transitions, one corresponding to the SH of 792 nm and two detuned by 2 nm in each direction. Qualitatively the scans are similar to those performed with weaker pulses, but the central maxima and the dark pulses are much less pronounced. The values of contrast calculated from signal ratios shown in 5.11(b) are 0.63 for the transitions pair 394 nm and 396 nm and 0.8 for the pair 394 nm and 398 nm which is still quite good.

5.3.2 Propagation simulation for the π step spectral phase

The simulations of TP excitation presented in the previous section consist of two steps. First, the phase shaped pulse (with the offset phase for dispersion compensation added) is propagated through the fiber. Then the SHG efficiency for the output pulse and a given crystal angle is calculated. More insight into why selective excitation with these pulses is possible in spite of nonlinear

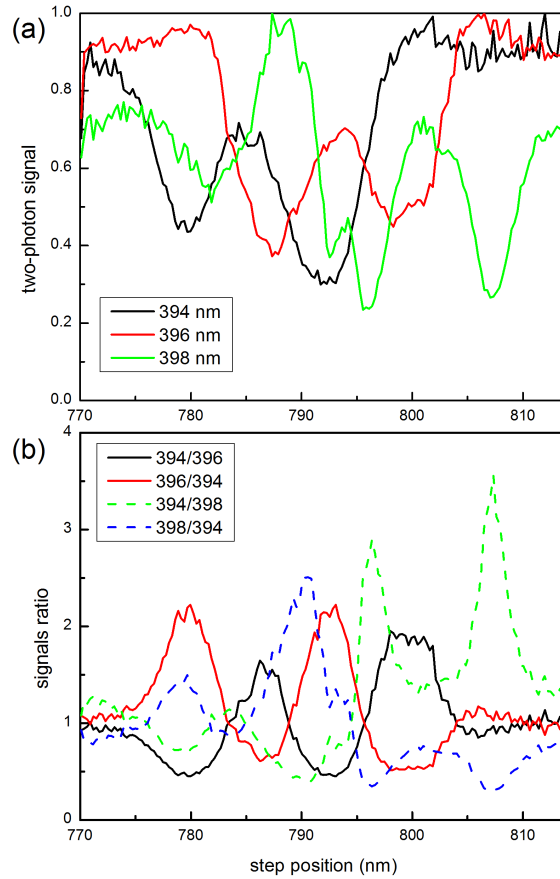


Figure 5.11: Excitation efficiency of narrow TP transitions with amplified pulses centered at 792 nm for 0.9 nJ pulse energy: (a) signal for different SH wavelengths, (b) signal ratios.

effects modulating the phase can be gained by taking another look at the results of the first step, that is pulse shapes after nonlinear propagation. Several examples are shown in fig. 5.12 where the pulse spectral phase and amplitude for three different pulse energies is shown before (dashed line) and after (solid line) the nonlinear propagation.

In fig. 5.12(a), the π step is at the central wavelength of the pulse. In the linear regime (pulse energy 0.01 nJ) the spectral amplitude remains almost unchanged. The spectral phase is slightly distorted but it remains antisymmetric around the central wavelength. As the pulse energy increases, the spectral amplitude is more and more narrowed and modulated and the spectral phase acquires a quadratic component which can be attributed to the nonlinear dispersion. However, the spectral phase remains nearly antisymmetric. This explains why the scans for the 390 nm transition shown in fig. 5.9 on page 60 have a maximum for a π step at 790 nm.

One can ask whether it is possible to understand intuitively why a π step in the spectral phase survives nonlinear propagation. One way to explain it is that, although the changes caused by the SPM can be significant, they are continuous due to the continuous nature of the propagation equations, so there is no way for a discontinuity such as a π step to appear - or disappear.

Next, pulses with λ_{AS} detuned from the central wavelength by about 5 nm are considered. The pulse shapes are shown in fig. 5.12(b). As expected, the modulated spectral amplitude becomes asymmetric. Again, a hole in the spectrum appears at the phase jump position (which is consistent with the measurements of the pulse spectrum after the fiber shown in fig. 5.15). In addition, by comparing the spectral phase before and after propagation through the fiber one sees clearly that the phase step shifts towards the central wavelength which confirms the intuitive picture mentioned

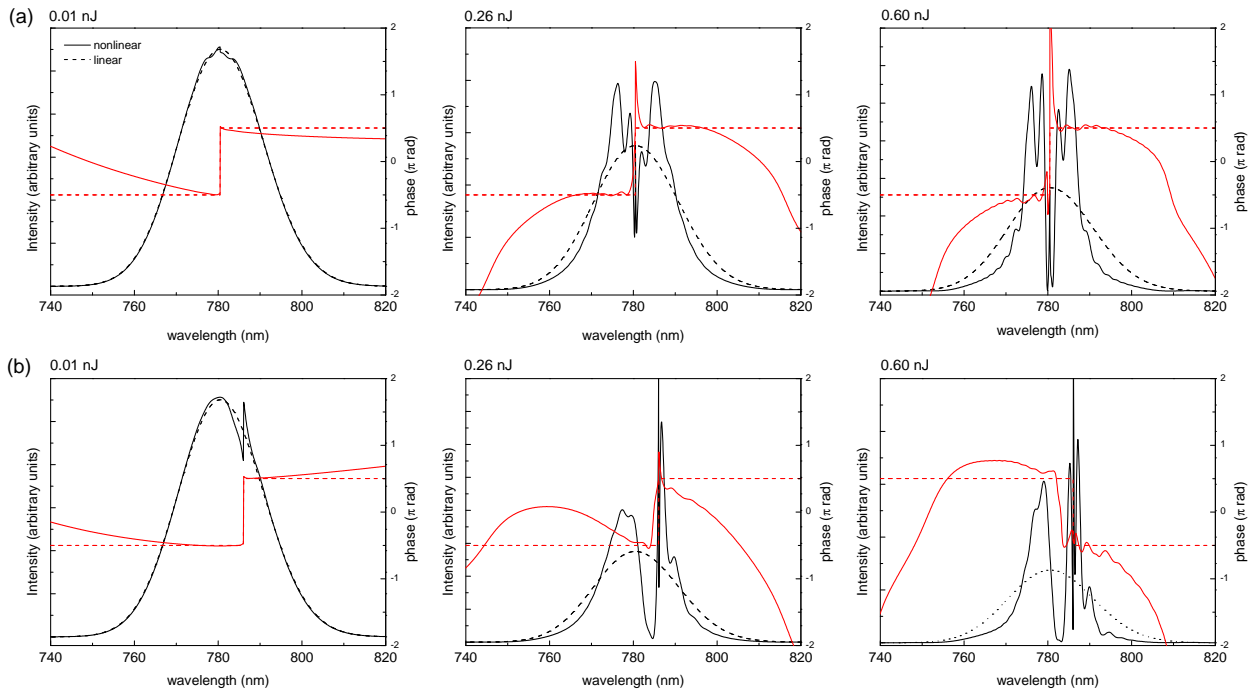


Figure 5.12: Simulation of nonlinear propagation of phase shaped pulses with energies 0.01 nJ, 0.26 nJ and 0.6 nJ. Pulses with a Gaussian spectral amplitude (black dashed line) and π step phase (red dashed line) with π step at (a) 780 nm and (b) 785.5 nm (shifted by 20 pixels) are shown. Amplitude and phase of the output pulses are plotted as black and red solid lines respectively.

in the previous section. Strikingly, the phase stays nearly antisymmetric around a certain point even for 0.6 nJ pulses.

The simulation presented in this section explains - at least qualitatively - all effects seen in the measurement. There are some quantitative differences between the simulation in 5.9 on page 60(a) and the measurement in 5.9 on page 60(b). Most probably they can be attributed to experimental noise and inaccuracies such as the pulse spectral amplitude not being perfectly Gaussian or a deviation of the fiber parameters used for the simulation from the actual parameters. For this simulation experimentally determined dispersion and bulk fused silica nonlinear refractive index were assumed. As will be shown in the next chapter, the latter is not strictly correct.

5.3.3 Other phase functions

Apart from the π step phase discussed in the previous sections I also tested other antisymmetric functions, a third-order polynomial and a sinus. In this section I will present the results obtained with the third-order polynomial phase centered around a frequency ω_{AS} :

$$\varphi(\omega) = \frac{1}{6}b_3(\omega - \omega_{AS})^3. \quad (5.3.1)$$

Strictly speaking, this spectral phase corresponds to a purely quadratic chirp only if ω_{AS} equals the central frequency of the pulse ω_0 ; otherwise it is a combination of quadratic and lower-order chirp. However, for simplicity I will call it “shifting quadratic chirp”. In addition, for consistency the results are presented as a function of λ_{AS} rather than ω_{AS} .

First, the value of b_3 has to be chosen. As shown in fig. 5.13, the optimal value is a compromise between higher signal for smaller b_3 and better selectivity (narrower peak) for bigger b_3 . For the

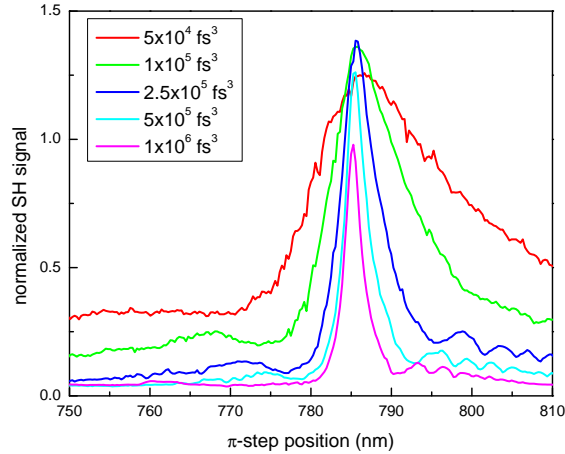


Figure 5.13: Excitation efficiency of a narrow TP transition at 392 nm with pulses with shifting quadratic chirp depending on the amount of chirp.

subsequent measurements two values that enable the best selectivity, $5 \times 10^5 \text{ fs}^3$ and $1 \times 10^6 \text{ fs}^3$, were chosen.

The results of λ_{AS} scans for different narrow transitions are shown in fig. 5.14 on the next page. As before, the signals are normalized by the short pulse signal for each pulse energy. Although the ratios are not shown, it is easy to see that this phase function is suitable for selective excitation.

It is interesting to consider the differences in the mechanism of selective TP excitation with pulses with a π step and a third-order polynomial phase. A direct result of applying a third-order phase centered around ω_{AS} is that lower and higher frequencies come later (or earlier, depending on the sign) than the frequency ω_{AS} , so the selectivity of the excitation can be explained very easily: at each point in time only photons with two frequencies $\omega_{AS} + \Omega$ and $\omega_{AS} - \Omega$ arrive, so the only TP transition that can be accessed is the one at $2\omega_{AS}$. As the shaped pulse propagates through the fiber, the nonlinear dispersion is not enough to change the temporal shape of the pulse significantly (the linear dispersion is compensated for with the offset phase). Indeed, shifting of the SH intensity maximum with increasing pulse energy that was clearly visible in fig. 5.9 on page 60 is not present here. This is confirmed by simulations (which I do not show here).

Another difference is the influence of the SPM on the spectral amplitude of the phase shaped pulse. Several examples are shown in fig. 5.15 on the next page. As already seen in the simulation shown in fig. 5.12, for pulses with the π step spectral phase (fig. 5.15(a)) a hole in the spectrum appears at the step position. This means that it is indeed the relative phase between the low and the high frequency components that plays the deciding role. In contrast, the spectra of the pulses with third-order phase (fig. 5.15(b)) have a single distinct peak that shifts with λ_{AS} which undoubtedly influences the efficiency of the TP excitation.

Further results concerning the TP excitation of broad transitions (that is, TPA in dyes) with phase-shaped pulses transported through the fiber will be presented in chapter 7.

5.4 Polarization shaped pulses

In the previous sections excitation of two-photon transitions with linearly polarized shaped pulses was described. If the considered transition is two-photon absorption in randomly oriented or isotropic atoms or molecules, the polarization of light does not matter. However, as discussed in section 2.3.1, the second harmonic generation process is polarization dependent. This property

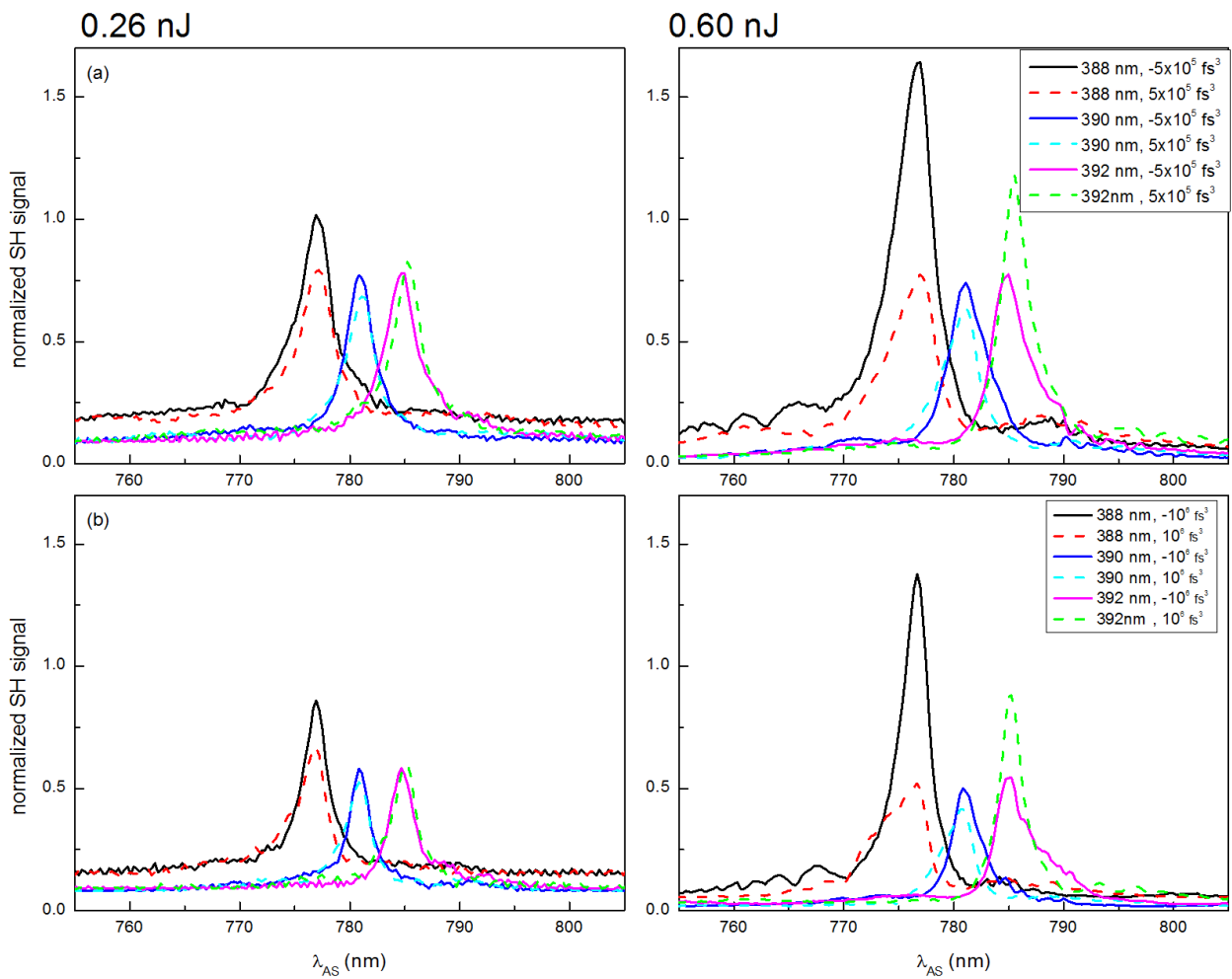


Figure 5.14: Excitation efficiency of a narrow TP transitions with pulses with 0.26 nJ (left column) and 0.6 nJ (right column) energy and (a) $\pm 5 \times 10^5 \text{ fs}^3$ and (b) $\pm 1 \times 10^6 \text{ fs}^3$ quadratic chirp.

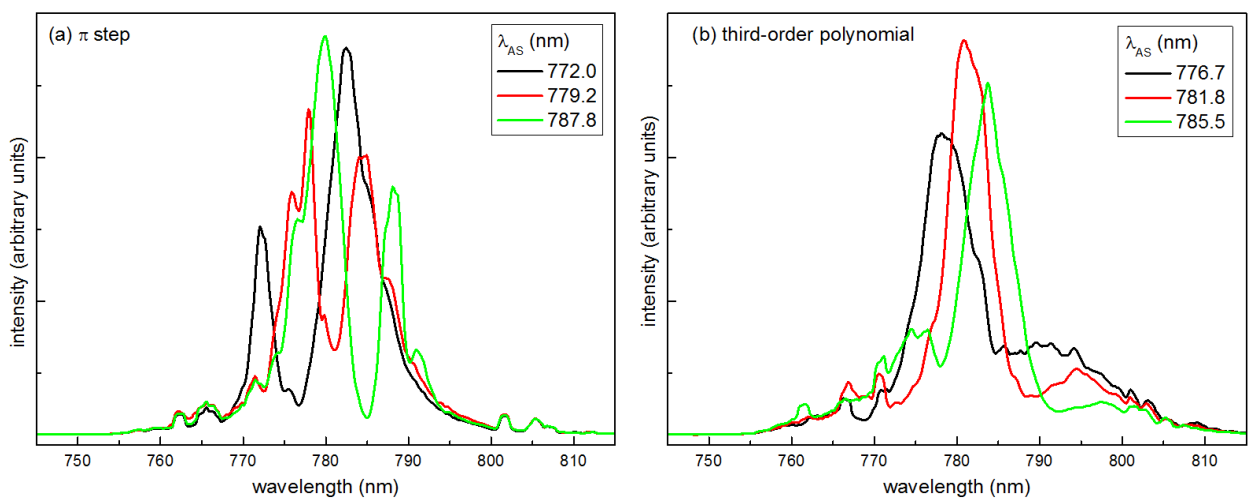


Figure 5.15: Pulses spectra after the fiber for pulses with (a) π step and (b) third-order polynomial spectral phase for different λ_{AS} .

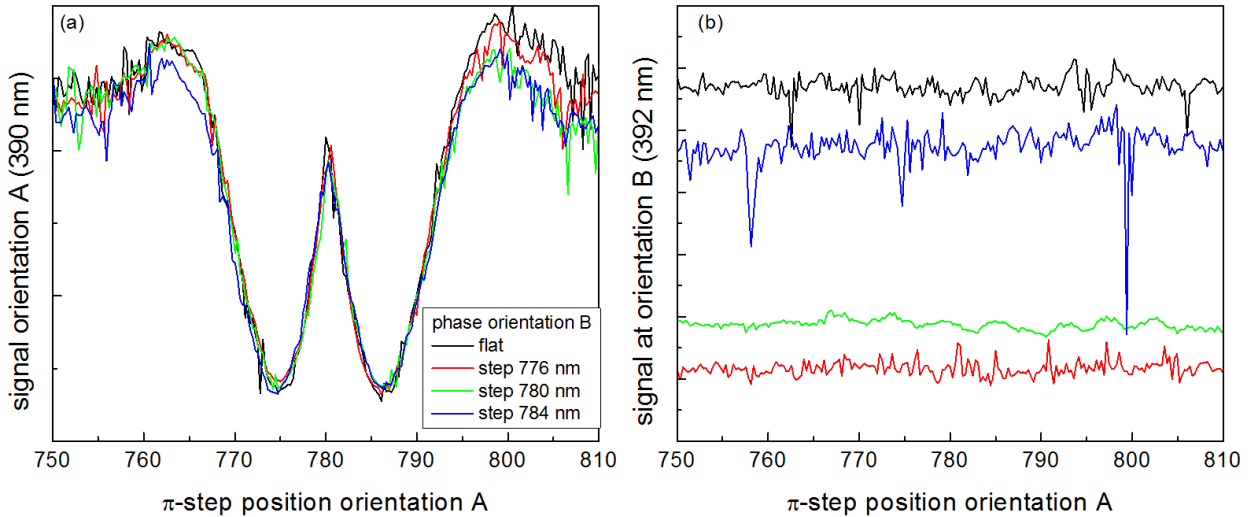


Figure 5.16: SH signal at both polarization orientations while scanning phase of the subpulse with orientation A, for four different phase patterns at orientation B.

is used in nonlinear microscopy imaging to deduce orientation of ordered structures such as collagen fibers [78]. Phase and polarization shaped pulses have been applied to structural contrast [79]. Also a compact fiber-optic SHG microscope capable of polarization anisotropy measurements has been demonstrated [80].

In this section I discuss one class of phase and polarization shaped pulses that can be applied to polarization dependent imaging. The pulses consist of two perpendicular subpulses with different spectral phases. The principle of generating such pulses was described in section 3.2.4, but there is one additional technical detail to consider.

If the subpulses are perfectly linearly and orthogonally polarized, the time delay between them does not matter. However, in practice the subpulses can be slightly elliptical or at an angle different from 90° because of setup imperfections such as the two modulator arrays not being perfectly perpendicular. As a result, the “unwanted” component of one subpulse interferes with the other subpulse. This effect explains the dependency of the excitation with one subpulse from the phase of the orthogonal subpulse that could be seen already in the preliminary measurements without the fiber (not shown).

The simplest solution is to delay the two subpulses so that they do not overlap in time. This way the “unwanted” components still contribute to the signal, but their own contribution is very small, and the more significant interference term vanishes.

To test this, a series of measurements was performed where the phase of one subpulse was kept constant (which corresponds to a constant voltage pattern on one of the LC arrays) and the phase of other was scanned as in the measurements in section 5.3. The delay between subpulses was 400 fs. Both π step and third-order polynomial phase functions were tested, but in this case the results obtained with the third-order phase were much worse, possibly because these pulses are longer and require more temporal shift to stop interfere.

Typical results obtained with the π step phase are shown in fig. 5.16. At orientation A, the SHG efficiency at 390 nm was measured depending on the position of the π step in the spectral phase of the pulse with polarization A. The measurement was repeated four times for different spectral phases of the pulse with polarization B: a flat (constant) phase and a π step at the positions corresponding the the signal maximum and both dark pulses for the 390 nm transition respectively. As can be seen in fig. 5.16(a), the spectral phase of pulse B does not influence the measurement at

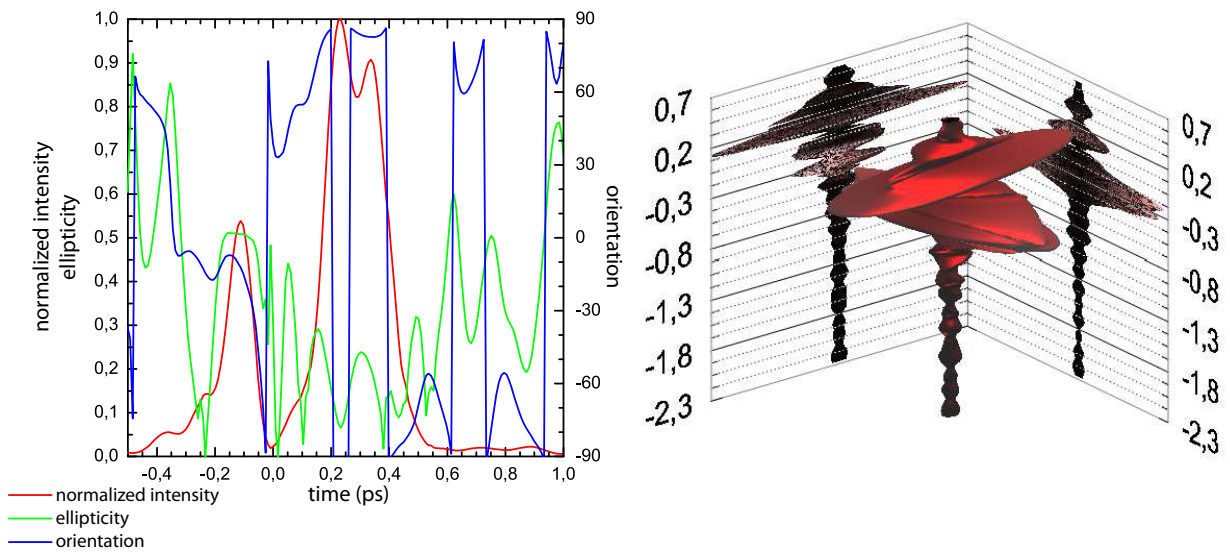


Figure 5.17: An example of a phase and polarization shaped pulse with a π step at 780 nm for polarization A and 786 nm for polarization B after transmission through the fiber. Left: the time-dependent normalized intensity, ellipticity and orientation. Right: a three-dimensional representation of the pulse.

orientation A. In addition, as the spectral phase of pulse A is scanned, the SH signal at orientation B, as shown in 5.16(b) for the 392 nm transition, remains constant and depends only on the phase of the pulse B. This measurement proves that the method presented here is capable of polarization-selective excitation of TP transitions, which is promising for the applications mentioned at the beginning of this section.

Finally, fig. 5.17 shows an example pulse, representing one point on the graph in fig. 5.16, characterized using the three-dimensional XC method described in section 3.3.3. As in the measurements presented in section 4.4.1, on the left the time-dependent normalized intensity, ellipticity and orientation are plotted and on the right a three-dimensional representation of the pulse is shown. In this measurement the spectral phase of the pulse is not directly visible but what can be seen is its influence on the temporal profile.

Reverse propagation

In the previous chapter I have shown how a certain class of phase-shaped pulses can be used for coherent control of two-photon transitions even though the pulse experiences self-phase modulation (SPM) during propagation through the fiber. However, a more general scheme for counteracting the nonlinear effects in the fiber would be desirable. In this chapter I will present the method of reverse propagation that can be used to generate arbitrarily shaped pulses after transmission through the fiber in the nonlinear regime. In the next chapter an application of this method to selective TPA will be demonstrated.

6.1 Method description

6.1.1 Motivation and previous work

One common approach to coherent control is first to find an optimal pulse that achieves the desired goal and then characterize it to draw conclusions about the investigated process. However, this often defeats the purpose of using an optical fiber in the first place. The fiber is useful to transport optical pulses to places which are otherwise difficult to access; the best example are endoscopic devices. In this case it is not practical or even not possible to place a bulky pulse characterization setup after the fiber. Instead, one needs a method to obtain an arbitrary pulse shape after transmission through the fiber. In the linear regime this task is straightforward. One has to determine an offset phase for dispersion (and birefringence if required) compensation and simply add it to the phase that yields the desired pulse without a fiber. The spectral amplitude is not affected by the linear propagation. Examples of complex shaped pulses obtained this way were presented in section 4.4. However, if the shaped pulse propagates in a nonlinear medium such as an optical fiber this approach is not valid anymore.

Most attempts to transport ultrashort pulses through optical fibers concentrate on obtaining a pulse that is as short and as broad as possible. In [81] a pulse shaper was used for the first time to compensate for both GVD and TOD of a few kilometers long fiber, but the pulses were too weak for nonlinear effects to play a role. In [82] a setup consisting of two pieces of fiber and a sequence of prisms in between was presented. The negative GVD of the prisms reversed the sign of the linear chirp of the pulse so that spectral broadening in the first fiber was approximately balanced by narrowing in the second fiber and with a 70 fs pulse with 0.5 nJ energy was obtained. However, the spectral and temporal compression was limited by uncompensated TOD.

If a prechirped pulse propagates through a fiber, nonlinear effects take place mostly during the last stage of propagation as the pulse gets shorter and the peak power higher. If instead the final temporal compression takes place e.g. in a piece of glass where the beam diameter is much higher than in the fiber, the pulse distortion caused by nonlinear effects can be significantly reduced [83]. Larson and Yeh [84] noted that for broadband pulses (100 nm FWHM) the dispersion of microscope optics in a typical fiber-based nonlinear microscope is sufficient to recompress them from the duration of 1.5 ps - which for 1 nJ pulse is too long for SPM to take place - to sub-10 fs.

Yet another possibility is to use photonic crystal fibers that have either a large mode area [85] or an air-filled core [86] and thus smaller nonlinear parameter. This does not eliminate nonlinear effects, but extends the energy range in which shaped pulses can propagate without being distorted by them.

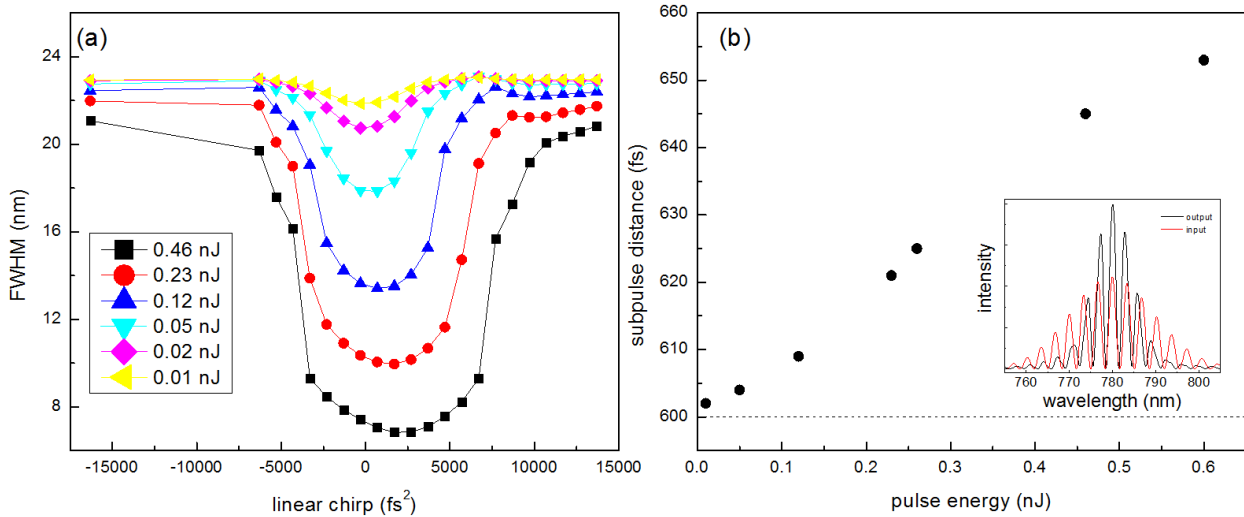


Figure 6.1: Simulation of the influence of SPM on the pulse shape for different pulse energies (a) FWHM dependence on linear chirp (b) temporal distance of two subpulses initially 600 fs apart. Inset: the spectrum of a double pulse before and after the fiber.

Most of the methods described above work by avoiding nonlinear effects instead of actually compensating for them. The only exception is the setup described in [82], but it has several drawbacks. Most of all, it is not possible to avoid losses in the negative GVD stage which makes the fluence in the second fiber lower than in the first. The authors compensate for that by using a fiber with a smaller core and thus higher nonlinearity, but this solution additionally complicates the experimental setup.

If one is not too concerned about the spectral narrowing, the simplest method of obtaining a short pulse after the fiber is applying a prechirp that compensates for the linear and nonlinear phase shift as I did in chapter 5. However, this method is not suitable for generating arbitrarily shaped pulses. First of all, the amount of spectral narrowing depends on the pulse energy. Furthermore, if the linear chirp of the pulse is varied the amount of narrowing changes as well (see fig. 6.1(a)). More generally this means that any spectral amplitude modulation applied to the pulse is modified by SPM. Let us consider a pulse consisting of two identical subpulses with distance t . It is generated by applying a $\cos^2(\omega\Delta t/2)$ modulation to the spectral amplitude. As the spectral envelope experiences narrowing by SPM, the period of the interference fringes decreases and as a result the distance between the subpulses increases (see fig. 6.1(b)).

Several schemes have been proposed to actually compensate for the modulation caused by dispersion and nonlinear effects. One class of schemes, considered principally for application in telecommunication, relies on modifying the pulse midway in between two identical pieces of fiber so that the distortions introduced in the first part are somehow compensated for by the distortions in the second part. The first of those methods, optical phase conjugation, dates back to 1979 [87]. It enables compensating for GVD as well as SPM, which is the lowest order and thus dominating nonlinear effect [88]. However, important effects such as loss, TOD and self-steepening are not taken into account. A more general scheme that requires time reversal in addition to the temporal phase conjugation but has less limitations has also been proposed [89]. Both methods are presented schematically in fig. 6.2. The biggest difficulty in these schemes seems to be the experimental realization of the conjugation. Most of the work that has been done until now are numerical simulations, with the exception of one experiment that uses four wave mixing [90].

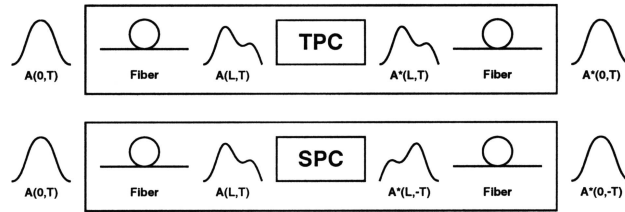


Figure 6.2: Schemes for dispersion and nonlinearity compensation: temporal phase conjugation (TPC) and spectral phase conjugation (SPC) (figure taken from [89])

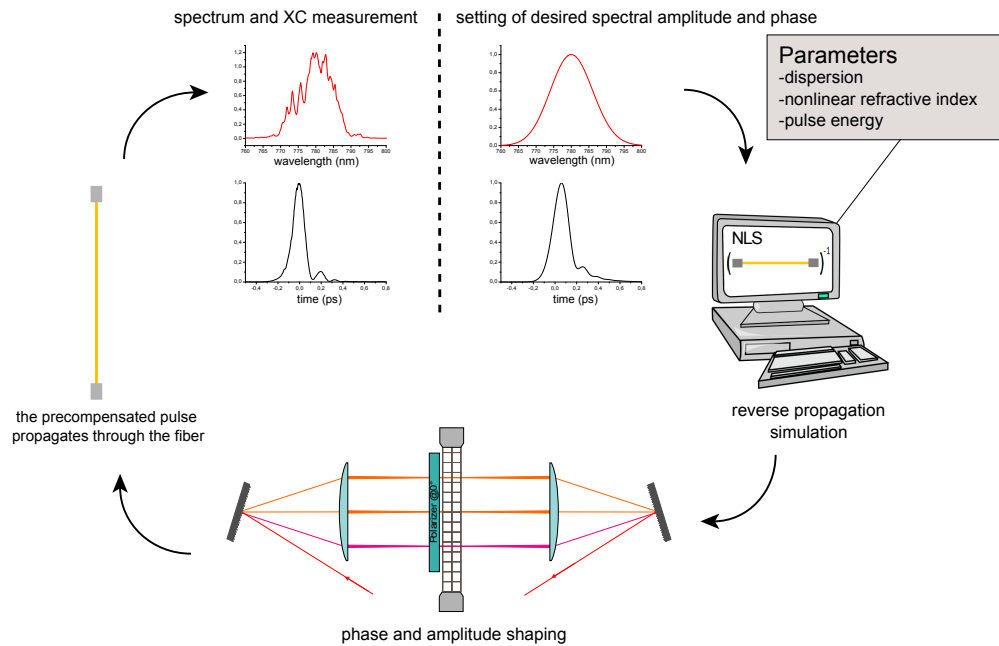


Figure 6.3: Generating arbitrarily shaped pulses by reverse propagation. The desired pulse shape is numerically propagated backwards through the fiber. The resulting pulse is generated by the shaper and propagates forwards through the fiber. An example of assumed (right) and actually measured (left) pulse temporal (black) and spectral (red) amplitude is shown.

6.1.2 The principle of reverse propagation

A general and relatively straightforward method for dispersion, loss and nonlinearities compensation has been proposed by Tsang et al. [91]. As shown in fig. 6.3, the method relies on simulating the propagation of the desired pulse shape through the fiber backwards and then generating the required input pulse shape with the help of a pulse shaper.

Backwards propagation can be understood by taking another look at the equation 2.4.15 on page 19. The term that describes the propagation is the spatial derivative on the left hand side. Reversing the direction of the propagation corresponds to reversing the sign of the spatial coordinate z which causes a minus sign to appear on the left hand side of the equation. Mathematically this is equivalent to changing the signs of the parameters on the right hand side: β_2 , β_3 and γ . Solving the equation with the changed signs corresponds to simulating the propagation of a pulse backwards through the fiber. Usually this means that the same code which is used for numerical forward propagation can be also used for reverse propagation.

The authors of [91] demonstrated the validity of this approach experimentally by characterizing the output pulse, simulating its reverse propagation and then comparing the simulated pulse to the

actual characterized input pulse. They also suggested, without performing the experiment, that a pulse shaper can be used to generate the input pulse shape required to obtain an arbitrary output pulse. Further work was done in the field of optical communication, where it has been proposed to apply reverse propagation (also known as digital backwards propagation) to compensate for nonlinear distortions in fiber-optic transmission systems [92, 93]. As a part of my work I have developed a method based on the idea from [91] and tested it in a series of experiments that are presented in this chapter.

6.1.3 Algorithm

If reverse propagation is to be applied to generating arbitrary pulse shapes, the propagation simulation has to be combined with a procedure for calculating phase and transmission patterns that yield the desired pulse shapes. For the measurements presented in this and the next chapter reverse propagation was integrated with the existing LabVIEW program that was used e.g. for parametric pulse shaping demonstrated in sec. 4.4. The split-step routine for simulating the propagation was taken from the Lab2 package [71] with modifications described in sec. 4.3.2.

However, there is one additional thing to consider. In general, the result of reverse propagation of a given output pulse is an input pulse with a different spectral amplitude than the available laser pulse. The required spectral amplitude can be obtained by amplitude shaping, but then the pulse energy changes and the performed simulation is not valid anymore. To use exactly the right energy as a parameter for the calculation one would have to know the spectral amplitude - which is the result of the simulation - before performing this simulation.

One possible solution to this problem is repeating the simulation and reaching the correct pulse energy iteratively. Instead, I assume a fixed loss due to amplitude shaping (or in other words a fixed overall shaper transmission) and use a modified pulse energy value for the simulation. The obtained transmission profile is then scaled down to fit the assumed total transmission. An example of a transmission profile calculated by this method is presented in fig. 6.4. If there is a need for scaling up the spectral intensity - which is not possible with a shaper - the program indicates an error. In some cases this approach leads to unnecessary loss, but is useful if one wants to obtain a series of pulses with changing spectral phase but constant energy.

The main advantage of the “assumed transmission” approach described above is that it is faster than the iterative method. On a standard PC a few seconds are needed for each simulation run, so an iterative method would require up to one minute per pulse shape. If faster switching is required or the same measurement repeated many times, it is possible to calculate the set of pulses that will be used in the measurement beforehand and then load the patterns that have to be written on the modulator from a file. In this case the only limitation is the modulator switching time and the runtime of the reverse propagation algorithm is not so important. On the other hand, if many different pulse shapes have to be calculated, e.g. during genetic optimization, the faster method is preferred.

6.2 Determination of the simulation parameters

Contrary to adaptive optimization, which can produce desired pulses after the fiber with no or very little knowledge of the fiber properties, reverse propagation requires precise knowledge of the parameters that appear in equation 2.4.15 on page 19, that is β_2 and β_3 , describing dispersion, and the nonlinear refractive index n_2 contained in the nonlinear parameter γ (see relation 2.4.8 on page 18). The other parameter needed to calculate γ , the effective mode diameter, was taken

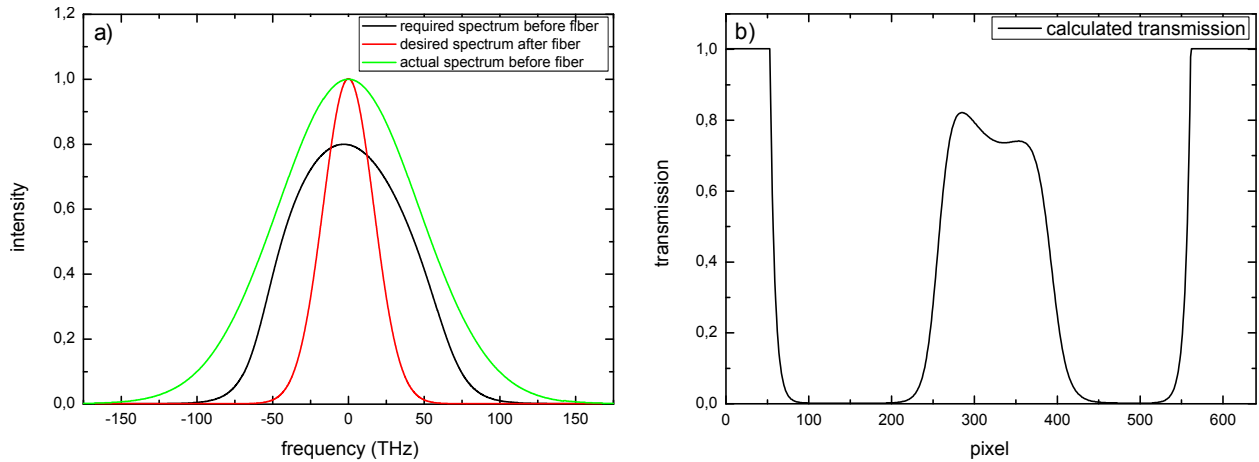


Figure 6.4: Transmission calculation in the reverse propagation procedure. (a) The desired pulse (red) is propagated backwards. The obtained pulse (black) is then compared to the available laser pulse (green). (b) Transmission that should be applied on the shaper is the ratio of the spectral intensities of the calculated and the actual pulse.

from the fiber datasheet. In addition, the initial value of the complex function $A(z)$ describing the slowly varying envelope of the pulse has to be known. Measurements of these quantities will be discussed in this section.

6.2.1 Chromatic dispersion

The method for measuring the chromatic dispersion of the fiber was already described in section 4.3.2. The results for central two wavelengths, 780 nm and 805 nm, are presented in table 4.1 on page 43. These values were subsequently used for the experiments in this and the next chapter.

It should be noted that the particular property of the used method for dispersion measurement - determining dispersion within the bandwidth of the pulse - in actually a limitation from the point of view of reverse propagation. In principle, reverse propagation is capable of describing spectral broadening as well as narrowing, but no measured dispersion values for the broadened pulse are available. For a small broadening extrapolated values can be used, but their uncertainty grows with the distance from the pulse central frequency.

6.2.2 Nonlinear refractive index

Although the dispersion of fused silica is well known, it cannot be used for simulating pulse propagation in the optical fiber because of the non-negligible waveguide contribution. In the case of nonlinear refractive index there is no waveguide contribution but it still turns out that if no value for the particular type of fiber is given, measuring it is a better solution than using the literature value for fused silica.

Many results for n_2 of fused silica obtained with different methods have been published [94], but results for femtosecond pulses at 800 nm central wavelength are scarce. In addition, one has to remember that the nonlinearity of a material is a result of several processes with different timescales, so the values obtained with CW lasers cannot be used directly for femtosecond lasers, as they contain contributions that are negligible at the femtosecond timescale, notably excitation of acoustic waves through electrostriction (Brillouin scattering), which for pulses longer than 10 ns attains its maximum value of 18% of the nonlinear refractive index [1].

Moreover, even values measured for femtosecond pulses cannot be always relied upon. It has been found that the nonlinearity of different samples of fused silica from different fabrication processes can differ by as much as 30% [95]. For these reasons I found it necessary to determine the nonlinearity of the fiber by measurement instead of relying on the values for bulk fused silica found in literature.

The method for determining n_2 used in this work relies on simulating spectral narrowing for negatively chirped pulses. More precisely, the spectrum after the fiber is measured and then the simulated input spectrum obtained by reverse propagation is compared to the actual input spectrum.

Alternatively, one could couple a transform limited pulse into the fiber and then compare the resulting broadened spectrum to the simulation. This method is simpler but it requires the knowledge of fiber dispersion in a broader spectral range, at least as broad as the modulated spectrum. As explained in the previous section, this would require a different method of dispersion measurement.

The obtained value is $n_2 = 2.6 \times 10^{-20} \text{ m}^2\text{W}^{-1}$, which is consistent with previous measurements [95]. The uncertainty of this measurement results from uncertainties of the other parameters used in the simulation of spectral narrowing, that is fiber dispersion as well as the intensity, spectral width and phase of the pulse. However, as far as the measured intensity concerned, if the same power meter is used all along and SPM is the only considered nonlinear effect, a systematic error of intensity measurement has no influence on the pulse shaping because the parameter determining the strength on nonlinear effects is in fact the product of n_2 and pulse intensity.

6.2.3 Laser pulse parameters

The fiber parameters considered above are sufficient to calculate the input pulse shape that yields the desired output shape. In order to determine the shaper modulation function - the transmission and phase filters - required to generate the calculated shape the spectral amplitude and phase of the available laser pulse must be known.

When measuring the spectral amplitude one has to keep in mind losses during coupling into the fiber. As discussed in section 4.1.2 space-time coupling limits the spectral bandwidth that can be coupled into the fiber as soon as a phase offset is applied. For the measurements presented in this chapter it was assumed that the bandwidth loss is constant and a Gaussian pulse with an appropriately reduced spectral width was used to calculate the transmission function. Finally, to obtain the spectral amplitude in physical instead of arbitrary units, overall intensity was measured with a power meter.

The spectral phase of the input pulse was not measured but instead the pulse was compressed at the fiber input by shaping the phase with the pulse shaper to maximize the TP diode signal (see sec. 3.3.4). The optimization was repeated several times to ensure that the global maximum was found. Finally, autocorrelation of the pulse after the shaper was measured to ensure that the pulse is transform-limited and therefore the phase is flat. The phase yielding the TL pulse determined in this procedure was treated as an offset that was subsequently added to all the calculated phase patterns.

6.3 Examples of parametrically shaped pulses

To demonstrate that the described method can be used to obtain arbitrary pulse shapes after nonlinear transmission through a fiber I generated and characterized several series of parametrically

shaped pulses with systematically varied parameters. Selected measurement results are presented in the following sections. The pulse shapes were chosen for their relevance for coherent control. Single chirped pulses can be used for example to control the shape of the vibrational wavepacket in the excited state. Two subpulses with variable delay are commonly used in pump-probe schemes. Finally, as discussed in the previous chapters, pulses with antisymmetric spectral phase are capable of selective excitation of two-photon transitions.

For comparison, I attempted to generate the same pulse shapes by neglecting the nonlinear effects and applying only the phase offset for chromatic dispersion compensation (this procedure is referred to in the following as linear compensation). To make the comparison meaningful, the pulses were attenuated by a factor equal to the assumed transmission used in the reverse propagation procedure.

The first series of measurements was performed with oscillator pulses with central wavelength 780 nm. The pulse energy after the fiber was limited to 0.59 nJ (or even less taking into account the loss caused by amplitude shaping). As far as single, relatively short pulses are concerned, this pulse energy is sufficient to see a significant influence of nonlinear effects on the pulse shape. However, in pulses that are relevant for coherent control the pulse energy might be distributed over longer time or between several distinct temporally separated subpulses, so the peak power is reduced. In addition, pulse sequences with multiple subpulses are generated by spectral amplitude shaping which e.g. for double pulses reduces the total pulse energy roughly by one half. Because of that one needs about four times more intensity to observe the same amount of nonlinear effects as for single pulses. To reach the required intensity amplified pulses with central wavelength 792 nm were used. The beam was attenuated so that in absence of amplitude shaping the maximal total pulse energy was 2.2 nJ. The experimental setup was the same as the one in fig. 5.1 on page 51, only now mostly the detection part instead of the BBO crystal was used (that is, the mirror described as optional was removed and the beam was directed to the XC and XFROG setup).

It must be noted that spectral narrowing is a result of fiber properties and cannot be eliminated by pulse shaping alone. Reverse propagation makes it easier to obtain desired pulse shapes, but it is not possible to generate a pulse shape that could not in principle be obtained with a different method, for example by characterizing the pulse after the fiber and adapting the input pulse shape iteratively. To account for this intrinsic spectral narrowing the spectral width of the desired output pulses has to be chosen appropriately because otherwise the calculated input pulse will be spectrally broader than the available laser pulse. I did this by performing propagation simulations and then choosing an output spectral width that for a given pulse energy was best matched to the input spectral width, that is required the least amplitude shaping.

6.3.1 Oscillator pulses

In this section several examples of single chirped pulses with 10 nm spectral width are presented. The pulses from the oscillator were compressed by the prism compressor so that a short reference pulse for XC measurements was available. In the presented measurements the assumed transmission (see sec. 6.1.3) was 80%, so the energy of the pulses in the fiber was 0.47 nJ.

The XC traces of obtained pulses are shown in the left column in figures 6.5 on the next page and 6.6 on page 77. For each pulse three traces are shown. Two measured traces, one generated with reverse propagation and one with linear compensation only, are compared to simulated traces of the desired pulse obtained by calculating the expected shape of the XC between the desired pulse and a broad TL pulse. The corresponding spectra are shown in the right column.

The temporal and spectral profiles of the linearly compensated pulses show significant deviations from the simulated shapes. Clearly in this pulse energy regime the nonlinear effects cannot

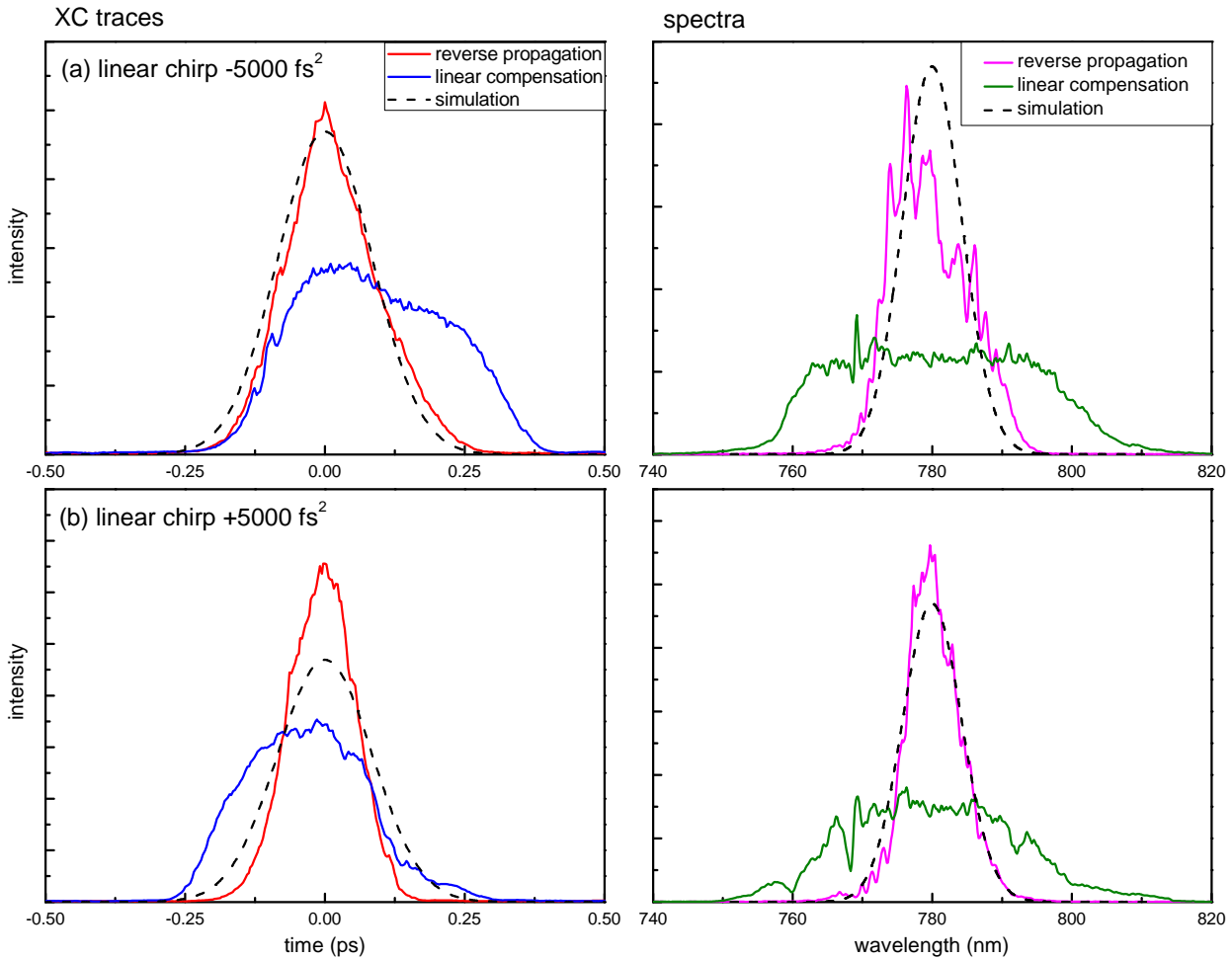


Figure 6.5: Comparison of XC traces (left) and spectra (right) of chirped single pulses obtained by reverse propagation (red and pink solid line respectively) and by linear compensation (blue and green solid line respectively) to theoretical traces (black dashed line) for 10 nm spectral width and linear chirp of (a) -5000 fs^2 and (b) 5000 fs^2 .

be simply neglected. At the same time, pulses generated by reverse propagation fit the simulation quite well which proves that the method works at least for this class of pulse shapes.

Apart from spectra and XC traces also XFROG traces (see section 3.3.2) of the pulses were measured. They contain more information than the other traces, but the complexity makes them more difficult to compare. In fig. 6.7 on page 78 an example set of three XFROG traces (simulation, reverse propagation and linear compensation) for a pulse with 10^9 fs^4 third-order chirp is shown. The pulse generated by reverse propagation does not fit the simulation perfectly, but on the other hand the linearly compensated pulse is so strongly distorted that the desired shape is not recognizable at all.

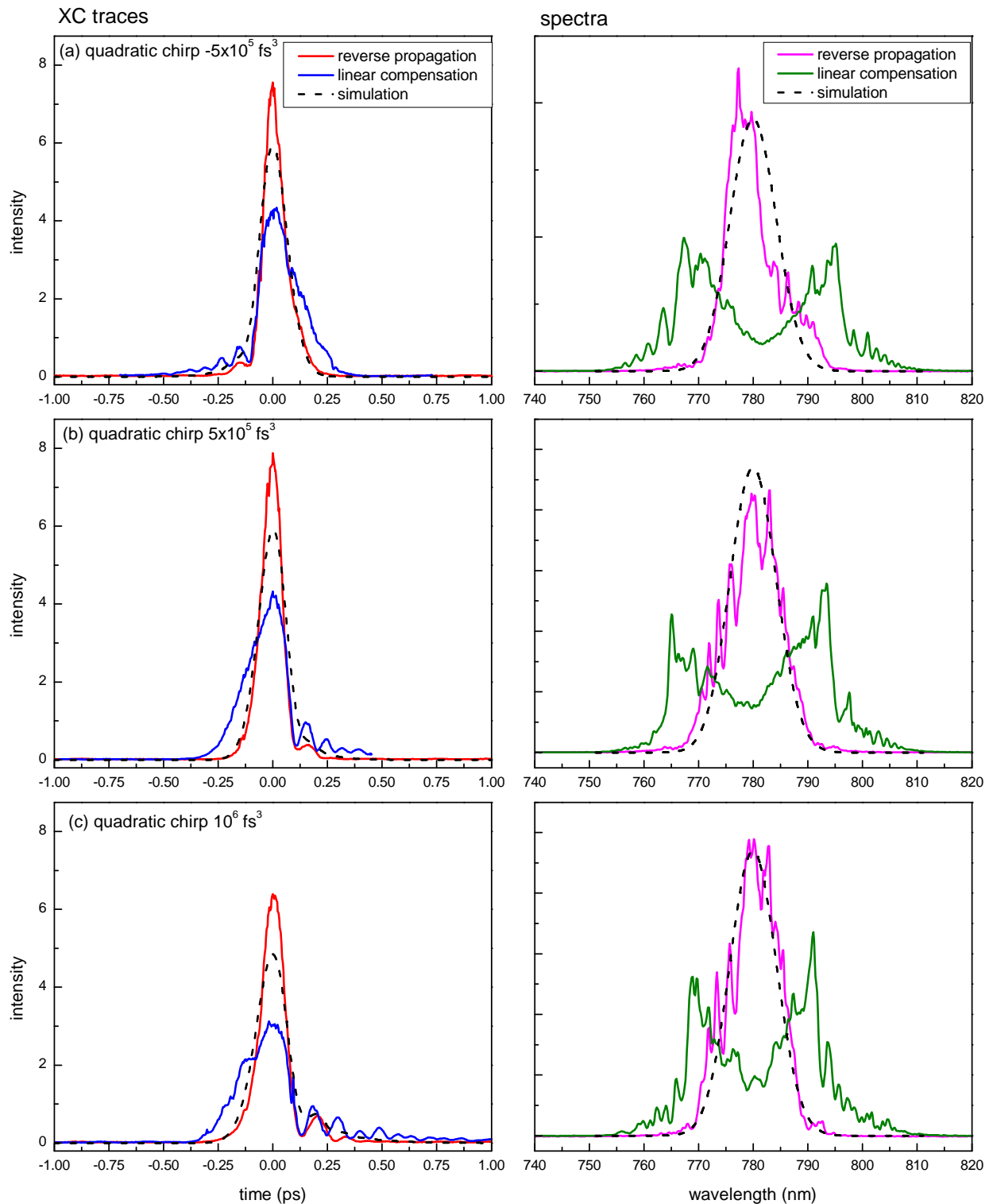


Figure 6.6: Comparison of XC traces (left) and spectra (right) of chirped single pulses obtained by reverse propagation (red and pink solid line respectively) and by linear compensation (blue and green solid line respectively) to theoretical traces (black dashed line) for 10 nm spectral width and quadratic chirp of (a) $-5 \times 10^5 \text{ fs}^3$ (b) $+5 \times 10^5 \text{ fs}^3$ (c) $+10^6 \text{ fs}^3$.

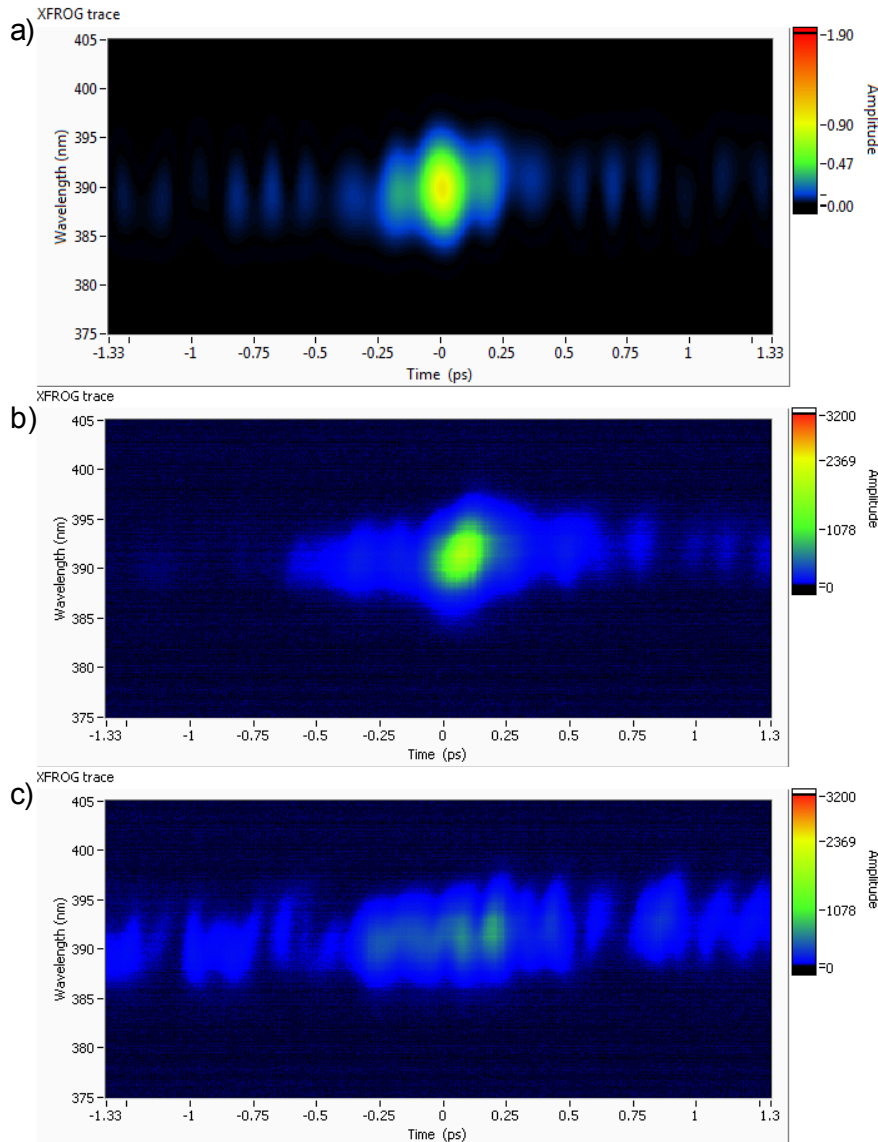


Figure 6.7: Comparison of XFROG traces of a single pulse with third order chirp of 10^9 fs^4 (a) theoretical trace (b) reverse propagation and (c) linear compensation.

6.3.2 Amplified pulses

In this section I will show results obtained with attenuated pulses from the amplifier. Like in the previous section, for each pulse three XC traces, that is the ones for pulses generated with reverse propagation and with linear compensation only and the simulated trace of desired pulse, are presented.

First, a series of single pulses with 7 nm spectral width and 0.9 nJ pulse energy was generated. Examples of XC traces of a short pulse as well as two pulses with a positive and a negative linear chirp are shown in figure 6.8 on the facing page. The corresponding spectra are shown in fig. 6.9.

Next, a series of pulse sequences consisting of two subpulses is presented: two short pulses in fig. 6.10 on page 80 and shaped pulses with individually controlled chirp and pulse energy in 6.11 on page 81 (see captions for more details). During this measurement the beam was attenuated so that the maximal available pulse energy in the fiber was 2.2 nJ. However, when pulse sequences are generated there is intrinsic loss caused by amplitude shaping. As a result, the total pulse energy

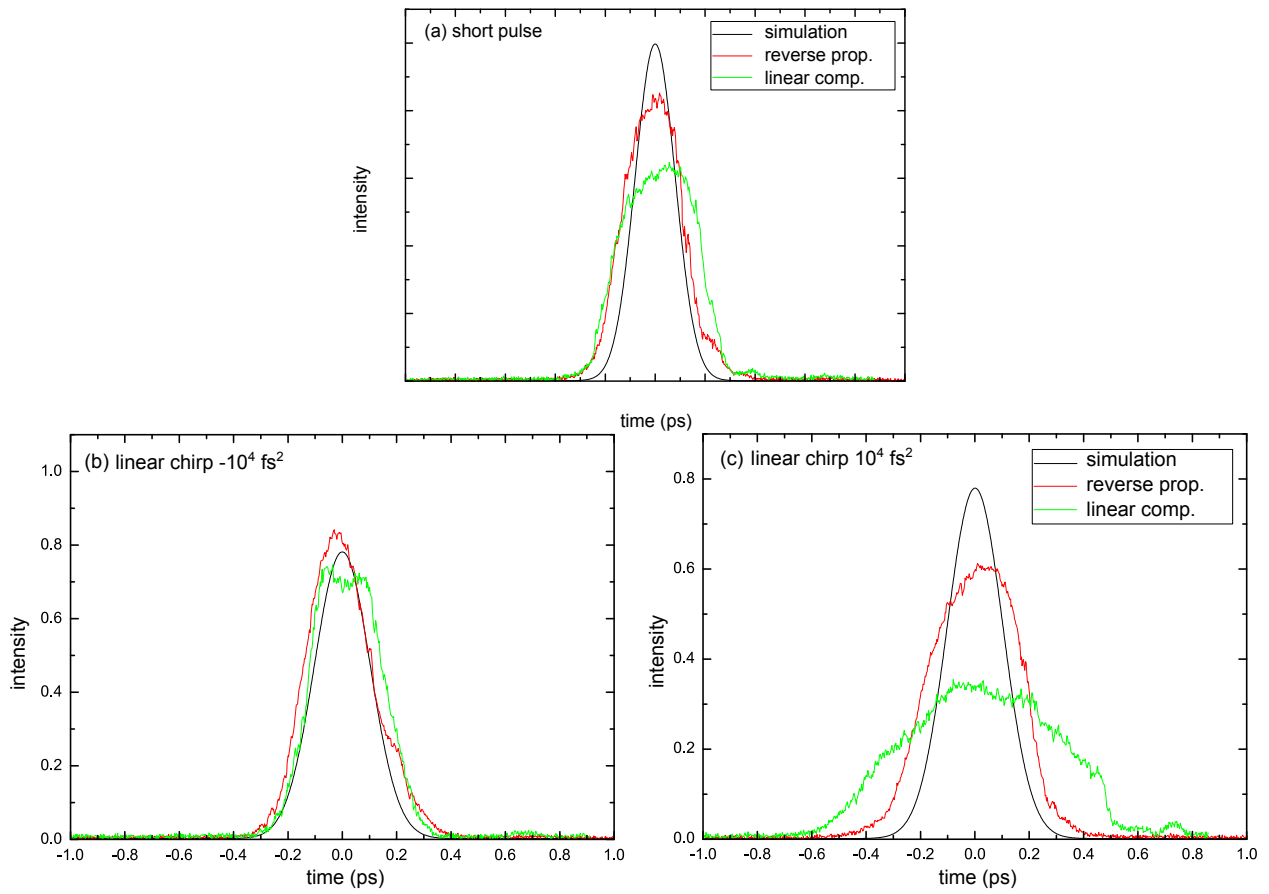


Figure 6.8: Comparison of XC traces of single pulses with 7 nm spectral width and 0.9 nJ pulse energy obtained by reverse propagation (red) and by linear compensation (green) to theoretical traces (black). (a) short pulse (b) linear chirp -10^4 fs^2 and (c) linear chirp $+10^4 \text{ fs}^2$.

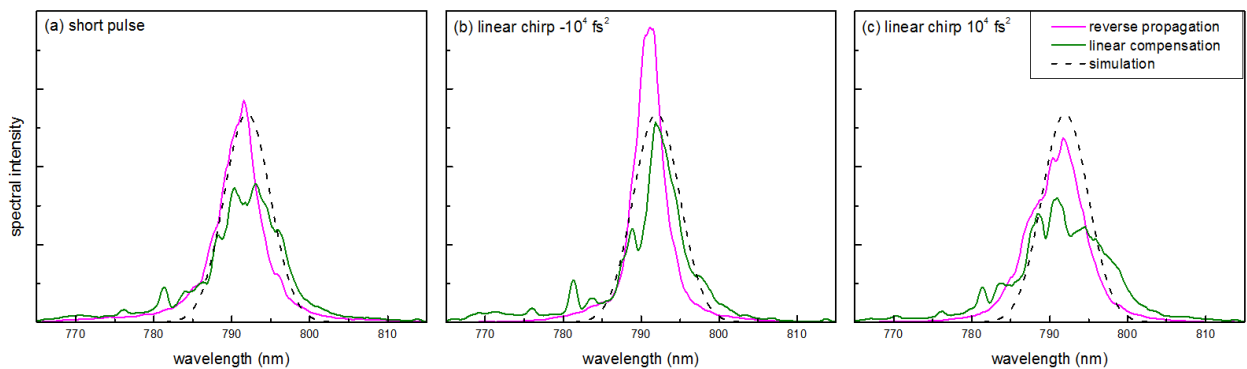


Figure 6.9: Comparison of spectra of single pulses with 7 nm spectral width and 0.9 nJ pulse energy obtained by reverse propagation (pink) and by linear compensation (green) to theoretical traces (black, dashed): (a) short pulse (b) linear chirp -10^4 fs^2 and (c) linear chirp $+10^4 \text{ fs}^2$.

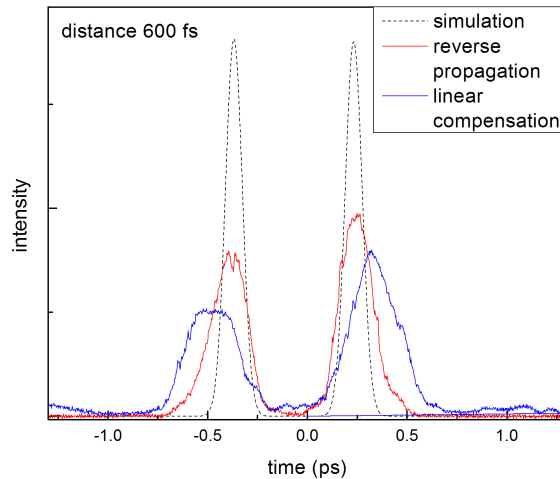


Figure 6.10: Comparison of XC traces of a double pulse with two identical subpulses separated by 600 fs obtained by reverse propagation (red, solid) and by linear compensation (blue, solid) to theoretical traces (black, dashed) for pulse energy about 1 nJ and 10 nm spectral width

was about 1 nJ depending on the pulse shape. This corresponds to about 0.5 nJ pro subpulse. In consequence, the subpulses experience less spectral narrowing than the single 0.9 nJ pulses. Accordingly, spectral width was set to 10 nm.

Like in previous example the pulse sequences obtained by linear compensation deviate more strongly from the theoretical traces than those generated by reverse propagation. Moreover, as predicted by the simulation shown in fig. 6.1 on page 70, the subpulse distance is not correct. This would be especially dangerous if the pulses were to be used in a pump-probe scheme where the subpulse distance is usually the most important variable.

For all the pulses shown here it is still true that the pulses generated by reverse propagation are much closer to the desired pulse shapes than those with linear compensation only. However, the deviations are larger than for the pulses presented in the previous section. This may indicate that the method does not work so well for higher pulse energies. Another possibility is that the differences between the desired and the obtained pulse shape are in fact an artifact of the detection. For amplified pulses the reference pulse was coming directly out of the compressor. The stretcher-compressor setup consists of highly dispersive gratings and so even a very small misalignment causes angular chirp that in turn leads to temporal distortions in focus (see references in section 3.1.3).

Some more insight into this problem can be gained by looking at the XFROG traces. Two examples are shown in fig. 6.12 on page 82. Indeed it appears that the results obtained with both methods share the same systematic error: all traces are tilted to the right. The pulse length after the shaper with only the phase offset written on the modulator was regularly monitored with the autocorrelator, so it is more likely that the source of this tilt is a linear chirp of the reference pulse. Performed simulations (not shown) confirm that the amount of tilt is consistent with about 1000 fs² chirp.

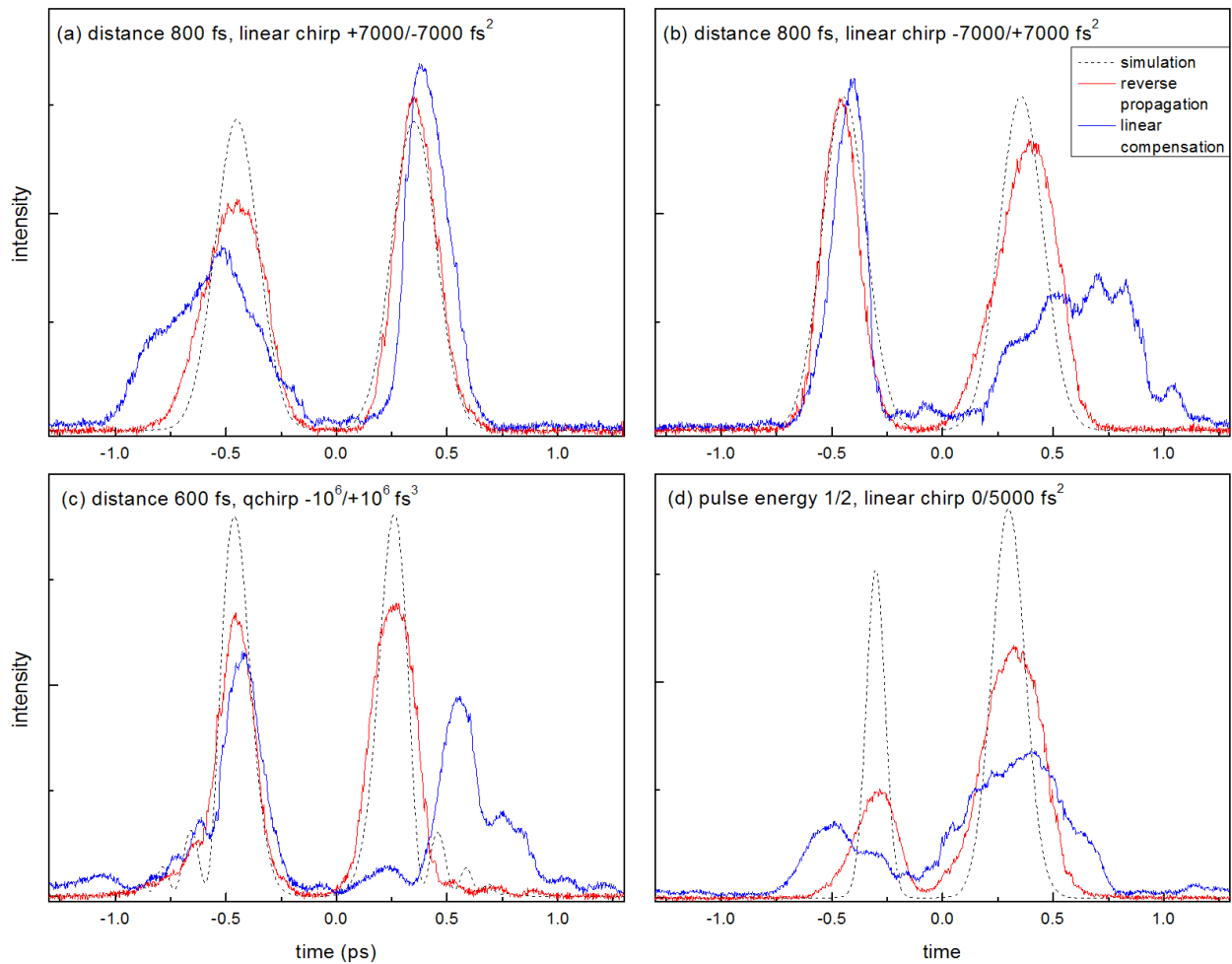


Figure 6.11: Comparison of XC traces of shaped double pulses obtained by reverse propagation (red, solid) and by linear compensation (blue, solid) to theoretical traces (black, dashed) for pulse energy about 1 nJ and 10 nm spectral width. (a) and (b) pulses with linear chirp with opposite signs, (c) quadratic chirp with opposite signs, (d) different pulse energies and linear chirp.

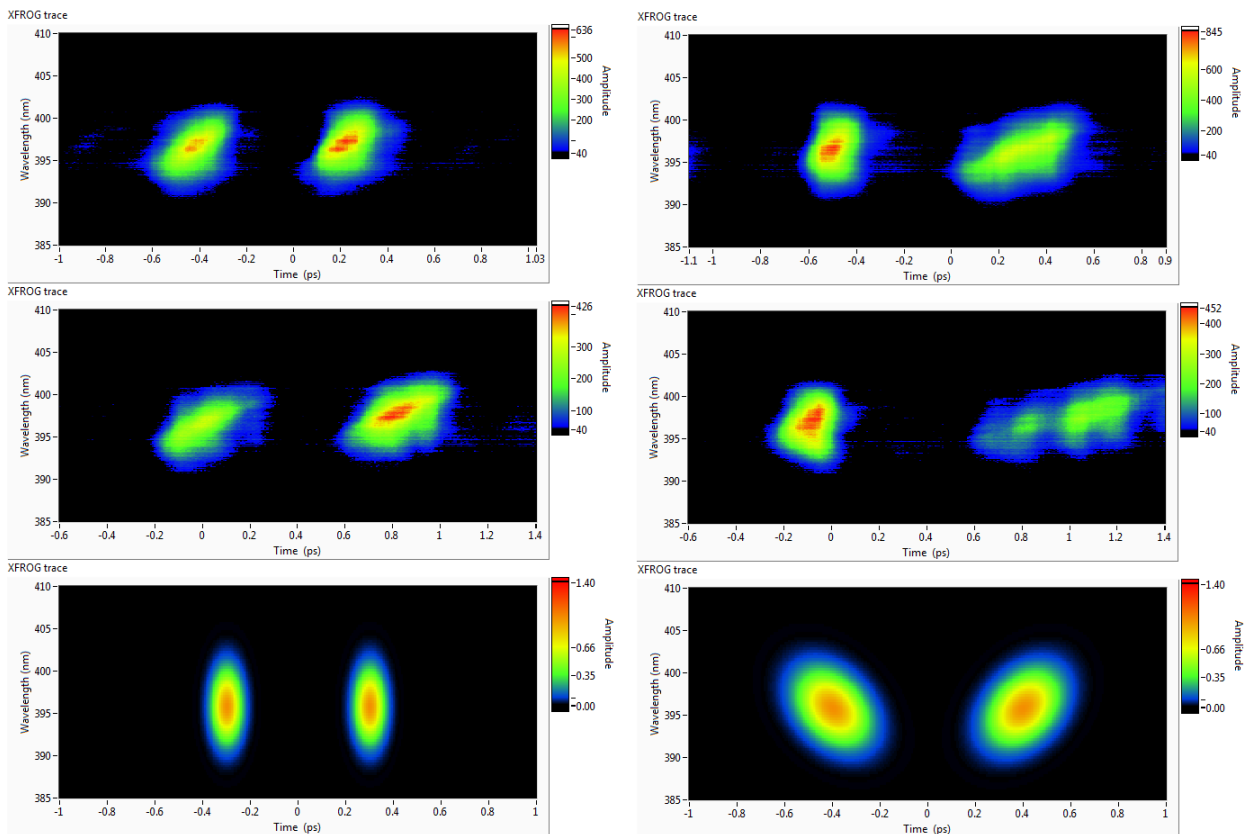


Figure 6.12: Comparison of XFROG traces of chosen double pulses obtained by reverse propagation (upper row) and by linear compensation (middle row) to theoretical traces (lower row). Left: two short subpulses 600 fs apart. Right: pulses with -7000 fs^2 and 7000 fs^2 linear chirp.

6.3.3 Pulses with antisymmetric spectral phase

In the previous chapter I demonstrated coherent control of two-photon transitions with phase-shaped pulses. I have shown that even if the pulse propagates through a fiber in the nonlinear regime, the spectral phase stays antisymmetric to a certain extent and selective excitation of narrow TP transitions is possible. In this section I apply reverse propagation to generating pulses with antisymmetric spectral phase. I compare the results to those obtained with the method described in the previous chapter which is in fact nothing else than linear compensation used in the previous sections.

For these measurements pulses with 780 nm central wavelength, 12 nm spectral width and 0.59 nJ energy were used. The assumed transmission was set to 50% (resulting in a pulse energy of 0.3 nJ). The reason for choosing such a low value is that reverse propagation of pulses with antisymmetric phase results in strongly modulated spectral amplitude.

Like in section 5.3 a series of λ_{AS} scans for different transition wavelengths λ_T was performed. This time each measurement was repeated twice, once using reverse propagation and once with linear compensation only. The results are summarized in fig. 6.13 on the next page.

In fig. 6.13(a) and (b) third-order polynomial phase (see section 5.3.3) was used. The results obtained with both classes of pulses are quite similar. The pulses generated by reverse propagation achieve more signal but on the other hand the peaks are broader which is a disadvantage. Actually these both differences are caused by spectral narrowing. Let us consider a phase function of the form $\varphi(x) = b_3x^3$. Scaling the variable x by a certain factor gives the same result as scaling b_3 by the same factor to the power of 3. This means that the spectral narrowing of a pulse with quadratic chirp leads to an apparent increase of the amount of chirp. Obviously this is a simplified picture that does not explain all effects experienced by such pulses, but it is enough to understand the results shown in this section.

In fig. 6.13(c) excitation with pulses with a π step spectral phase is presented. Like for the pulses with shifting quadratic chirp, the central peak is narrower and excitation efficiency higher because spectral narrowing is accounted and compensated for. However, in the results for the two detuned transitions, especially the one at 388 nm, only a small improvement is visible.

One issue with generating pulses with π step spectral phase by reverse propagation becomes clear at once if one looks at the simulation of forward propagation in fig. 5.12 on page 63. Through SPM the phase jump leads to sharp features in the spectral amplitude. Reproducing those features exactly would require very low assumed transmission (in a pulse shaper a peak can only be created by attenuating all the other wavelengths) and very high spectral resolution of the shaper setup. Because of this I also tested a smoothed version of the π step where instead of jumping by π the phase value changed over a few pixels. The results are shown in fig. 6.13(d). However, no significant difference was observed.

In most of the plots where signal generated by reverse propagation is shown a characteristic feature is visible: for certain wavelengths a sharp peak going almost to zero is visible. To find out whether this is not an artifact of detection - for example a problem with communication with the analog-to-digital converter - the scan was repeated several times, but the features did not disappear. They turned out to be numerical errors of the reverse propagation procedure that happen probably as a result of sharp features in the pulse amplitude leading to singularities in the calculation. In spite of trying several approaches, such as decreasing the step length, increasing the sampling or rewriting the spectral phase between steps in a simpler form, I was not able to solve this problem.

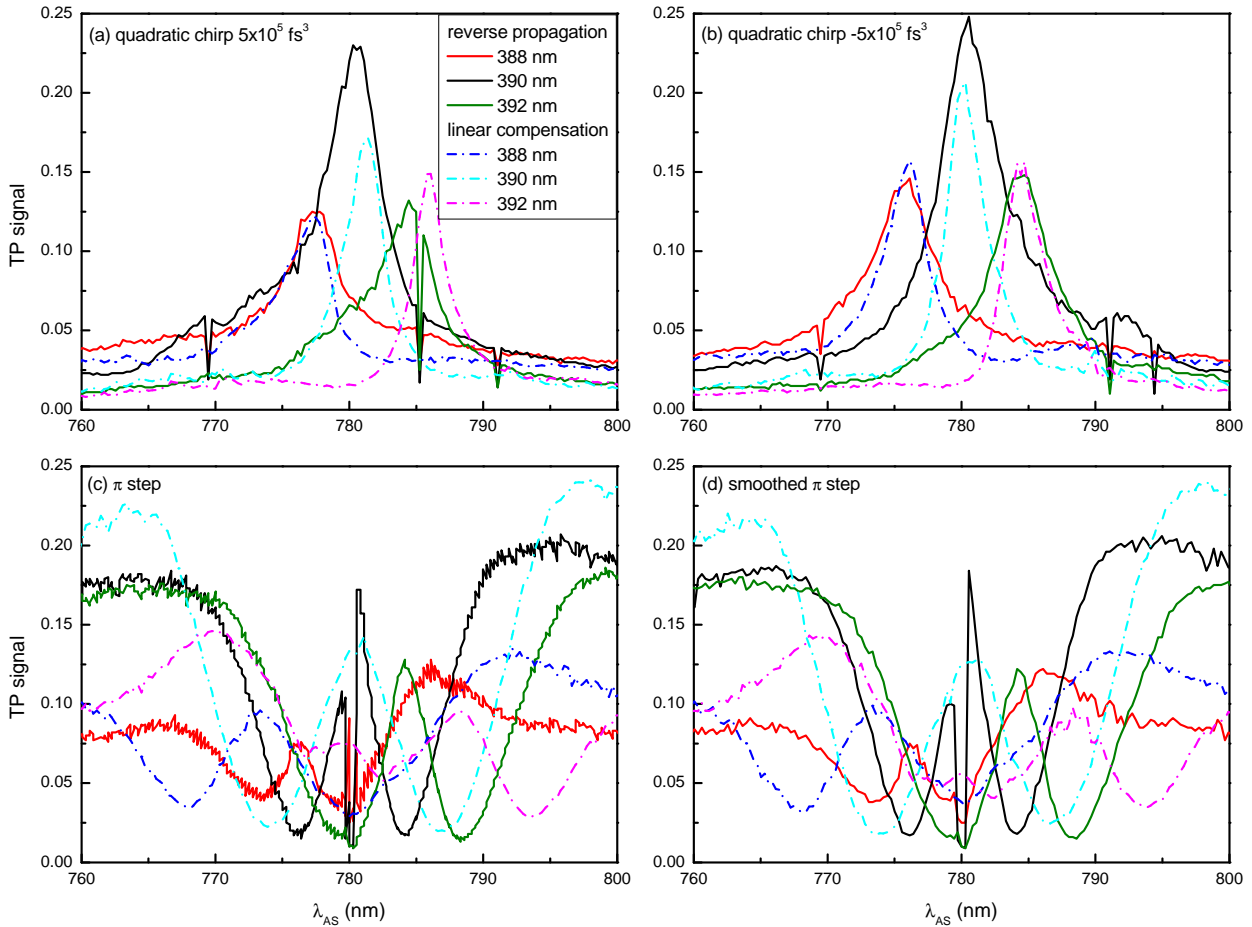


Figure 6.13: Comparison of excitation efficiency of narrow TP transitions with pulses with anti-symmetric spectral phase obtained by reverse propagation (solid lines) and by linear compensation (dash-dot lines).

6.4 Discussion

To sum up, reverse propagation is a suitable method for compensation of nonlinear effects for some classes of shaped pulses, namely single pulses and pulse sequences with individually controlled chirps. Other pulse shapes can also be generated, but due to the SPM a complex spectral phase leads to sharp features in the spectral amplitude. This in turn requires setting the assumed transmission to a low value and makes reverse propagation not practical.

Apart from systematic errors in the pulse characterization setup that were already discussed in section 6.3.2, possible reasons of the observed discrepancies between the desired and the obtained pulse shape are limited resolution of the pulse shaper setup and measurement uncertainties of the input parameters. The shaper resolution limits the complexity and precision of forming the spectral phase and amplitude. Increasing the resolution is also required if a longer fiber is to be used, as higher spectral resolution corresponds to larger temporal window. Alternatively an additional element with constant negative GVD could be combined with the programmable modulator.

Another important issue is the limited knowledge of the input pulse shape. Ideally, the pulse characterization setup should be fiber-coupled to account for the influence of the space-time coupling on the pulse shape. It would also have to be sensitive enough so that nonlinear effects in the detector itself could be avoided.

Extending the method to higher pulse energies should be in principle possible. The most important requirement apart from sufficient shaper resolution is including self-steepening and intrapulse Raman scattering in the propagation simulation. For the latter, the parameter T_R (see eq. 2.4.15 on page 19) must be known.

It would be interesting to test this method for other types of fiber. Low nonlinearity fibers (large mode area or hollow core) are interesting from the point of view of the application. However, for SPM the important parameter is the nonlinear length L_{NL} (defined by relation 2.4.10 on page 18), so one can expect similar results but in a different pulse energy range. A more interesting case would be a fiber with low GVD where the dominating contribution is the TOD. This is actually the case in fibers where the pulse propagates in the vicinity of the zero-dispersion wavelength.

In this chapter I only considered pulses that stayed linearly polarized during the whole propagation. The NLSE and thus reverse propagation can be also applied to a more general case of elliptically polarized light. This would require including additional linear and nonlinear effects, that is birefringence, nonlinear birefringence and cross-phase modulation (XPM). Mathematically this means replacing eq. 2.4.7 with a set of two equations containing coupling terms. A more detailed discussion of XPM is beyond the scope of this work but can be found for example in [1]. It is known that XPM plays a role in optical communications [96]. To compensate for it, an advanced split-step method for the digital backward-propagation that includes XPM has been proposed [97].

Selective excitation of molecules in solution

In this chapter I present the results of selective TPA in laser dyes in solution with shaped pulses transported through the fiber. I compare the results obtained with phase-shaped pulses with anti-symmetric spectral phase, similar to those used in chapter 5, to those obtained with pulses generated by reverse propagation introduced in chapter 6.

The measurements were performed with oscillator pulses at 805 nm central wavelength. To increase the available pulse energy, the prism compressor was removed and the chirp of the laser pulse resulting from the intracavity dispersion was compensated by the shaper. Apart from that, the experimental setup was the same as the one shown in fig. 5.1 on page 51, but the nonlinear crystal was replaced with a cuvette containing the solution. The used laser dyes, solvents and concentrations are listed in section 3.4.2. The efficiency of TPA was not measured directly but instead the intensity of the laser induced fluorescence was detected using the setup shown in 3.10 on page 36.

7.1 Motivaton

One of the fields where ultrashort pulses offer an advantage over other optical techniques is nonlinear optical microscopy and imaging. Due to the involvement of multiphoton processes the signal in nonlinear microscopy depends nonlinearly on the intensity of tightly focused light, so the excitation is possible only in the laser beam focus where the peak intensity is the highest. This enables optical sectioning and reduces detrimental out-of-focus processes such as photobleaching and photoinduced damage. In addition, infrared laser have the advantage of falling into the maximum optical transparency window for most biological systems [98].

Several methods used in these fields utilize two-photon processes such as SHG [99] and two-photon excited fluorescence [100]. It has been known for some time that the efficiency of such processes can be controlled by shaping the spectral phase of the pulse [30]. More recently, shaped pulses have been incorporated into nonlinear microscopy and imaging. The group of Dantus performed a series of experiments where they explored the possibility of applying phase-modulated ultrashort pulses to selective excitation of multiphoton processes in solution, including distinguishing between a two- and a three-photon absorbing species as well as two two-photon absorbing species with different absorption spectra [33, 101]. Later they demonstrated selective two-photon excitation of fluorescent probe molecules under a microscope using phase-only modulated ultrashort 15-fs laser pulses [31]. Other works where selective excitation was achieved directly in a live fluorescently-labeled cell [32] or a significantly simplified setup was used followed [102]. Furthermore, it has been shown that pulse shaping applied to two-photon processes can be used to suppress unwanted three-photon absorption [33] or provide structural contrast [79].

In parallel, compact fiber-based microscopes are being developed. Devices based on both single-mode and photonic fibers enable measurements using various methods utilizing two- and three-photon processes. Imaging is also possible by using fiber bundles or a scanning mechanism such as a piezoelectric element attached to the fiber end [103]. Combining such setups with the coherent control methods mentioned above would allow to extend the capabilities of fiber-based microscopy.

7.2 Measurements without fiber

As in section 5.1.1 measurements with pulses transported through the fiber were preceded by measurements without the fiber. The purpose of those preliminary measurements was to see what degree of selectivity is achievable and to determine what the optimal pulse shapes are.

First, phase-shaped pulses with antisymmetric spectral phase functions were used. Two phase functions were tested. One of them was the third-order polynomial phase already introduced in section 5.3.3 (see equation 5.3.1). For a better comparison with previous work [31,32] a sinusoidal phase function was used as well. In my experiments the sinusoidal phase was defined as

$$\Phi(\lambda) = A \sin [\alpha(\lambda - \lambda_{AS})]. \quad (7.2.1)$$

Strictly speaking, the function has to be antisymmetric in frequencies, so the correct definition is $\Phi(\omega) = A \sin [\delta(\omega - \omega_{AS})]$. This is also how the other authors define the sinusoidal (or cosinusoidal) phase. However, within the relatively moderate bandwidth of the used pulse the relation between frequency and wavelength is almost linear.

The phase-shaped pulses were compared to narrow pulses with shifting central wavelength obtained by amplitude shaping. In the linear propagation regime the pulses were generated simply by attenuating unwanted parts of the spectrum with the pulse shaper, so the pulse energy was significantly reduced. However, the efficiency of TPA depends not on the pulse energy but peak power, so it is a priori not clear whether temporally stretched phase-shaped pulses with a higher pulse energy will generate more two-photon signal than short pulses with less energy.

In figures 7.1 on the next page and 7.2 on page 90 selective excitation in a mixture of Coumarin 1 (C1) and Rhodamine B (RB) is demonstrated. Let us first take a look at the TP signal generated with phase-shaped pulses. In fig. 7.1(a) the fluorescence intensity of C1 is plotted (RB signal is qualitatively very similar as shown in the example in the inset on the right). The first observation is that the signal dependence on λ_{AS} is qualitatively different from that shown in fig. 5.14 on page 65 in section 5.3.3. The reason for that is quite obvious. In section 5.3.3 excitation of narrow TP transitions with different wavelengths λ_T was considered. Accordingly, in fig. 5.14 narrow peaks at $\lambda_{AS} = 2\lambda_T, i$ are visible. On the other hand, the laser dyes have broad absorption spectra, so λ_{AS} can be shifted quite a lot for the second-order spectrum of the pulse to still overlap with the absorption spectrum. Another difference between broad and narrow transitions is that for broad transitions shorter pulses are preferred. A consequence of that is the strong dependence of the signal intensity on the amount of phase modulation (the parameter A for the sinus function and b_3 for the polynomial phase).

As can be seen in the inset in fig. 7.1(a), the C1 absorption spectrum is blue-shifted with respect to the RB absorption spectrum. This is consistent with previous work (see section 3.4.2). The difference is small, but some degree of selectivity should be still possible. As demonstrated in 7.1(b), this is indeed the case. According to the measurements, by shaping the spectral phase of the pulse the fluorescence intensity ratio can be changed by as much as 40%. The highest achieved contrast value was $\Gamma = 0.47$ for quadratic chirp of 10^6 fs^3 . This is comparable to the values obtained in [32]. However, a direct comparison is difficult as in [32] different fluorephores as well as much broader pulses were used.

One important observation is that both for the sinusoidal and the polynomial phase contrast is not maximized by the same pulse shapes that maximize the signal. While higher signal requires shorter pulses, selectivity requires more modulated and thus longer pulses. In the end, the choice of the optimal phase function is a compromise between high signal and high contrast.

For pulses with shifting λ_0 two approaches were tested. First, a measurement with TL pulses with varying spectral width was conducted (7.2(a), left). Next, one spectral width was chosen and

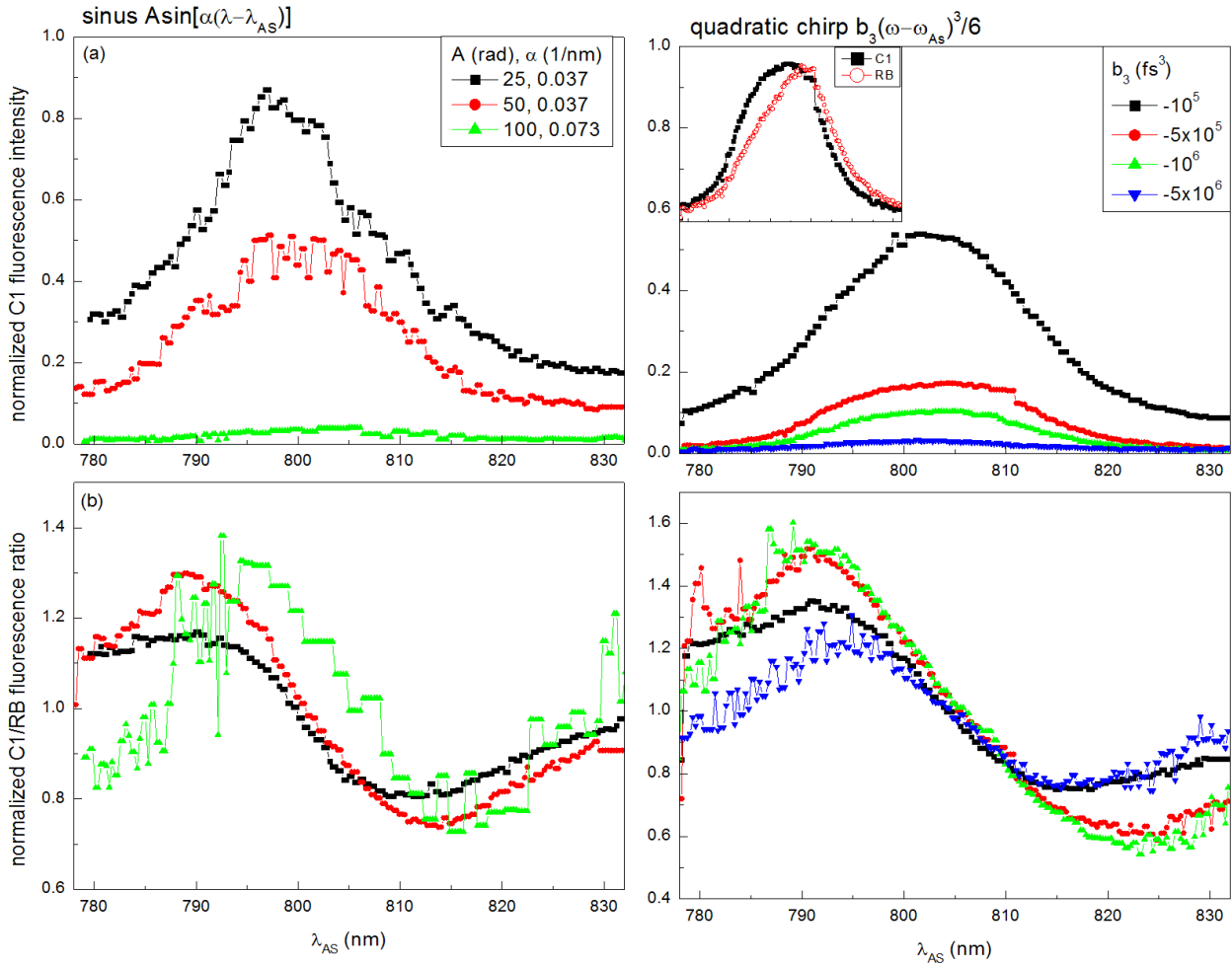


Figure 7.1: Selective excitation of C1 and RB with phase shaped pulses with sinusoidal (left) and third order polynomial (right) phase, without the fiber: (a) normalized fluorescence intensity of C1 and (b) normalized fluorescence ratio. Inset: comparison of C1 and RB fluorescence intensity.

amplitude shaping was combined with a third-order polynomial phase centered at a wavelength shifted with respect to the central wavelength of the amplitude-shaped spectrally narrow pulse.

The dependence of the fluorescence intensity and fluorescence ratio on λ_0 for different $\Delta\lambda$ is shown in the left column in figures 7.2(a) and 7.2(b) respectively. As expected the signal decreases with decreasing spectral width. Interestingly, the contrast stays practically the same which means that all in all the broader pulses are preferred. $\Gamma = 0.52$ which is a little higher than for the phase-only shaped pulses. One thing to note is that it is easier to increase the fluorescence ratio than to decrease it. This is simply a consequence of the chosen spectral range. This can be understood by looking at the inset in 7.1(a): there is a range of wavelengths where C1 fluorescence intensity is significantly higher than that of RB, but not the other way round. Possibly the result could be improved by choosing another central wavelength of the laser pulse. I did not try that because of practical reasons: a change of the central wavelength of the laser requires realigning the shaper setup, finding new offset phases and so on.

In the right column in figures 7.2(a) and 7.2(b) the spectral width of the pulse was kept constant but a quadratic chirp was added. The assumption was that quadratic chirp would change the second-order spectrum of the pulse so that there would be some change in the fluorescence ratio

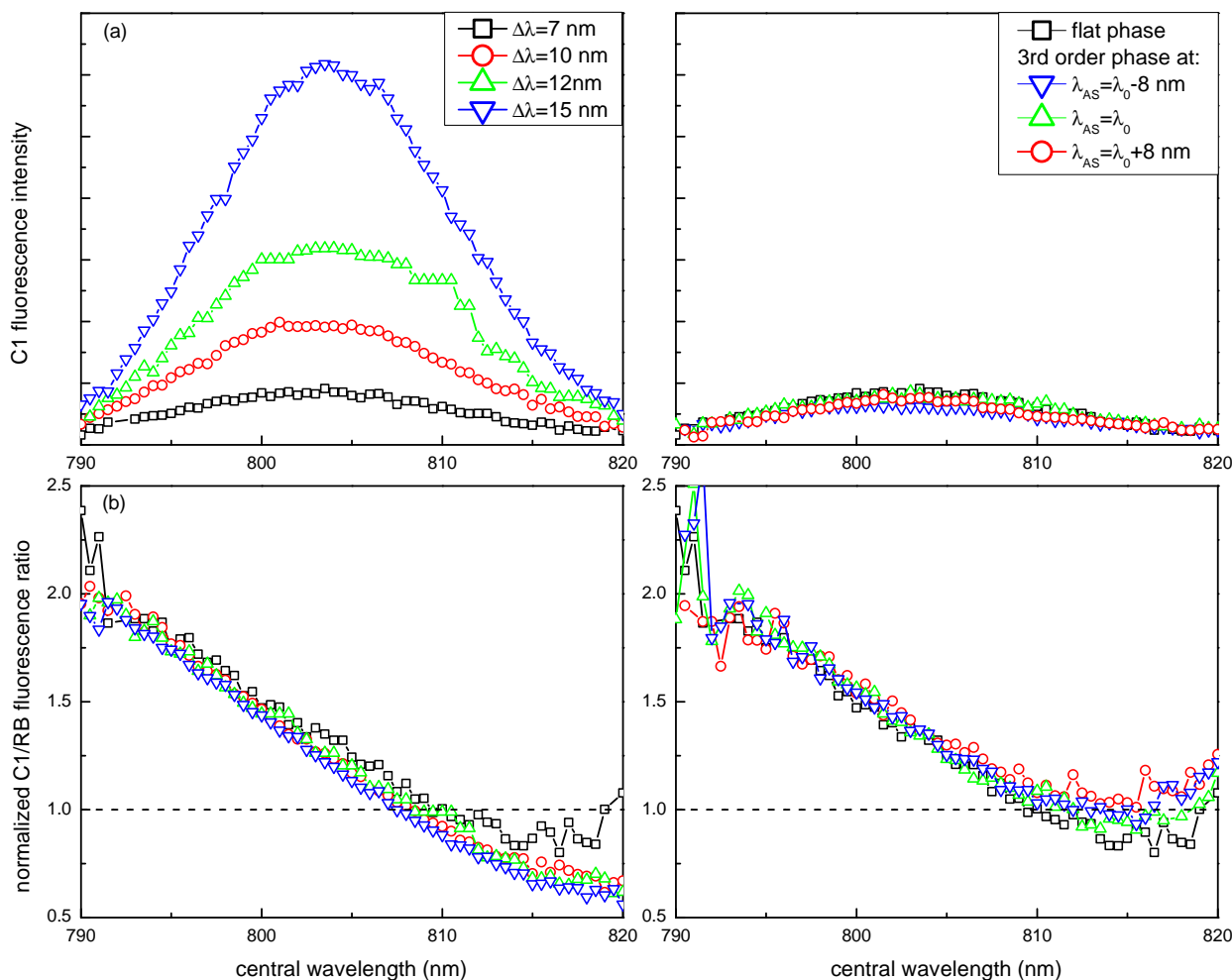


Figure 7.2: Selective excitation of C1 and RB with phase and amplitude shaped pulses with shifting λ_0 for different spectral widths (left) as well as for 7 nm spectral width combined with quadratic chirp shifted with respect to λ_0 (right), without the fiber: (a) fluorescence intensity of C1 and (b) normalized fluorescence ratio.

depending either on the sign of the chirp or its position respective to the central wavelength of the pulse. However, no significant change could be seen in the measurements.

Next, the measurements described above were repeated for the fluorescein (FITC) and Rhodamine B (RB) mixture. The results are presented in figures 7.3 on the facing page and 7.4 on page 92 (it should be noted that the plotted values are not normalized). The pulse parameters were chosen based on conclusions drawn from measurements in the C1 and RB mixture. For example, for the sinusoidal phase $A = 50$ and bigger were not used as they reduce the signal significantly. The combination of amplitude shaping and quadratic chirp was omitted completely as it has been found that it offers no improvement comparing to TL amplitude shaped pulses.

Qualitatively the results obtained in the FITC and RB mixture are very similar to those in C1 and RB. However, the achieved selectivity is much worse. The best obtained values of Γ are 0.11 for the sinusoidal spectral phase, 0.16 for the third order polynomial phase and 0.2 for the pulses with shifting central wavelength. This can be understood by looking at the inset in fig. 7.4(a), where fluorescence intensity of both dyes is compared. First of all, apparently the chosen concentration ratio was not optimal as the FITC fluorescence signal is lower than that of RB.

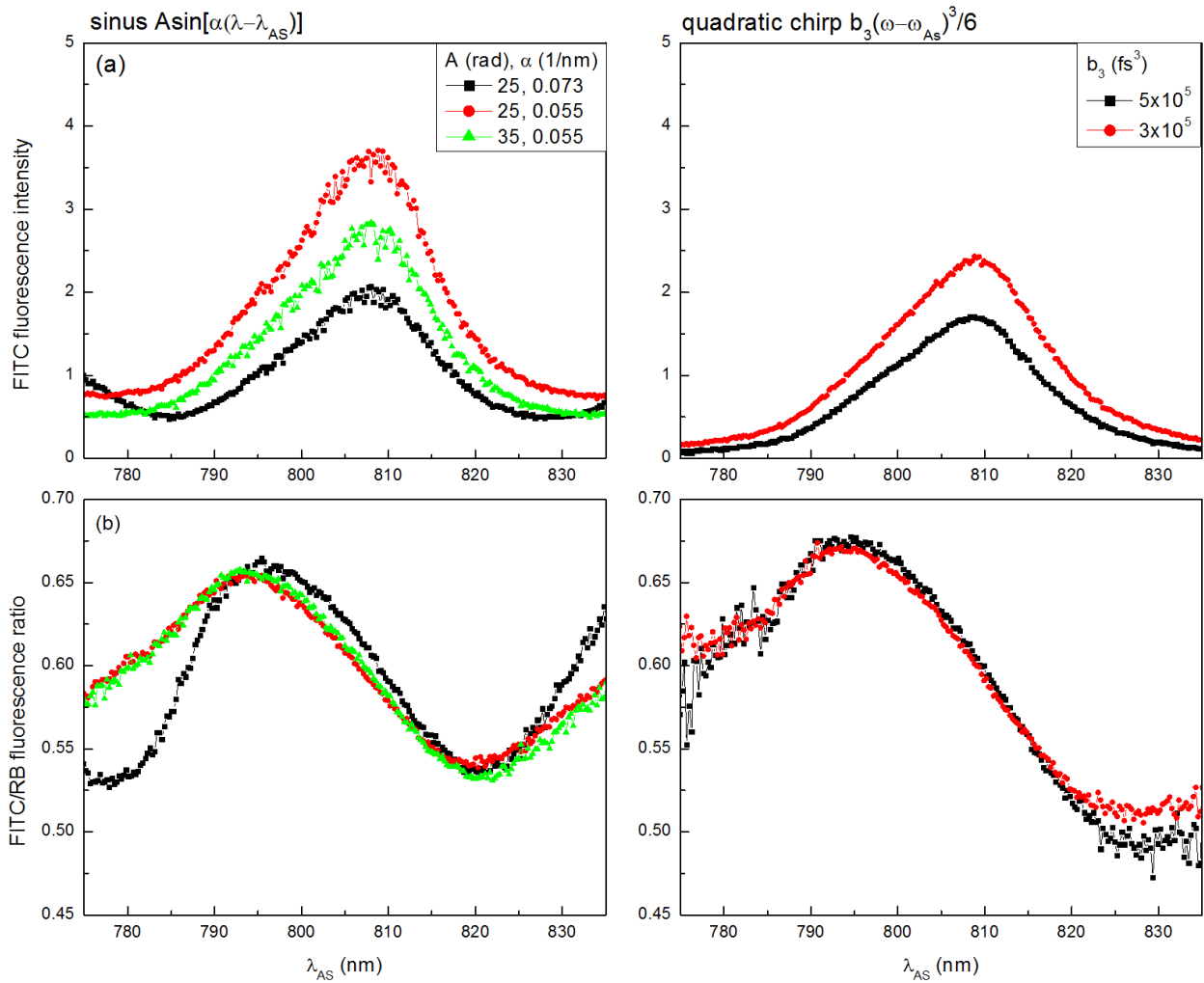


Figure 7.3: Selective excitation of FITC and RB with phase shaped pulses with sinusoidal (left) and third order polynomial (right) phase, without the fiber: (a) fluorescence intensity of FITC and (b) fluorescence ratio.

Secondly, the signals are very similar which means that in the investigated spectral range the TP absorption spectra of the two dyes in the chosen solvent are also similar.

All the measurements in the FITC and RB mixture were performed on the same day, so it is possible to directly compare the fluorescence intensity after the excitation with the two classes of pulses. The highest contrast is achieved by the phase-shaped pulses with 5×10^5 fs³ quadratic chirp as well as amplitude-shaped pulses with 15 nm spectral width. Out of those two pulse series, the amplitude-shaped pulses yield a few percent more fluorescence signal despite having less energy.

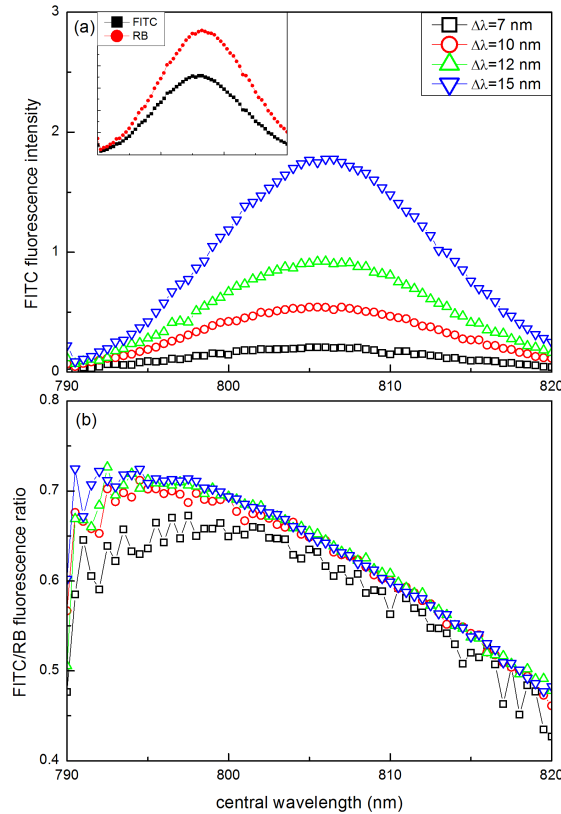


Figure 7.4: Selective excitation of FITC and RB with amplitude shaped pulses with shifting λ_0 for different $\Delta\lambda$, without the fiber: (a) fluorescence intensity of FITC and (b) fluorescence ratio. Inset: comparison of FITC and RB fluorescence.

7.3 Phase shaped pulses

In the previous section I have demonstrated selective excitation of laser dyes with both phase-only and phase- and amplitude-shaped pulses. I have checked what contrast can be achieved if the shaped pulses are not narrowed and distorted by nonlinear propagation in an optical fiber. Here I will show results obtained with phase-shaped pulses after propagation through the fiber. These measurements can be seen as an application of the method of coherent control of TP transitions with phase-shaped pulses transported through the fiber presented in chapter 5.

In fig. 7.5 on the facing page selective excitation in the C1 and RB mixture with phase-shaped pulses transported through the fiber is demonstrated. The normalized C1 fluorescence intensity is shown in fig. 7.5(a) and the normalized C1 to RB fluorescence ratio in 7.5(b). Qualitatively the results are quite similar to those obtained without the fiber. The achieved contrast is $\Gamma = 0.25$ which is worse than without the fiber, but still acceptable. Like before, the optimal pulse phase has to be chosen as a compromise between signal and contrast.

The same measurements were repeated for the FITC and RB mixture. The results are shown in fig. 7.6 on page 94. Here some change of the ratio is visible, but the degree of selectivity is very poor - Γ does not exceed 0.1. This is not very surprising seeing that even without the fiber the value obtained with phase shaped pulses was only 0.16.

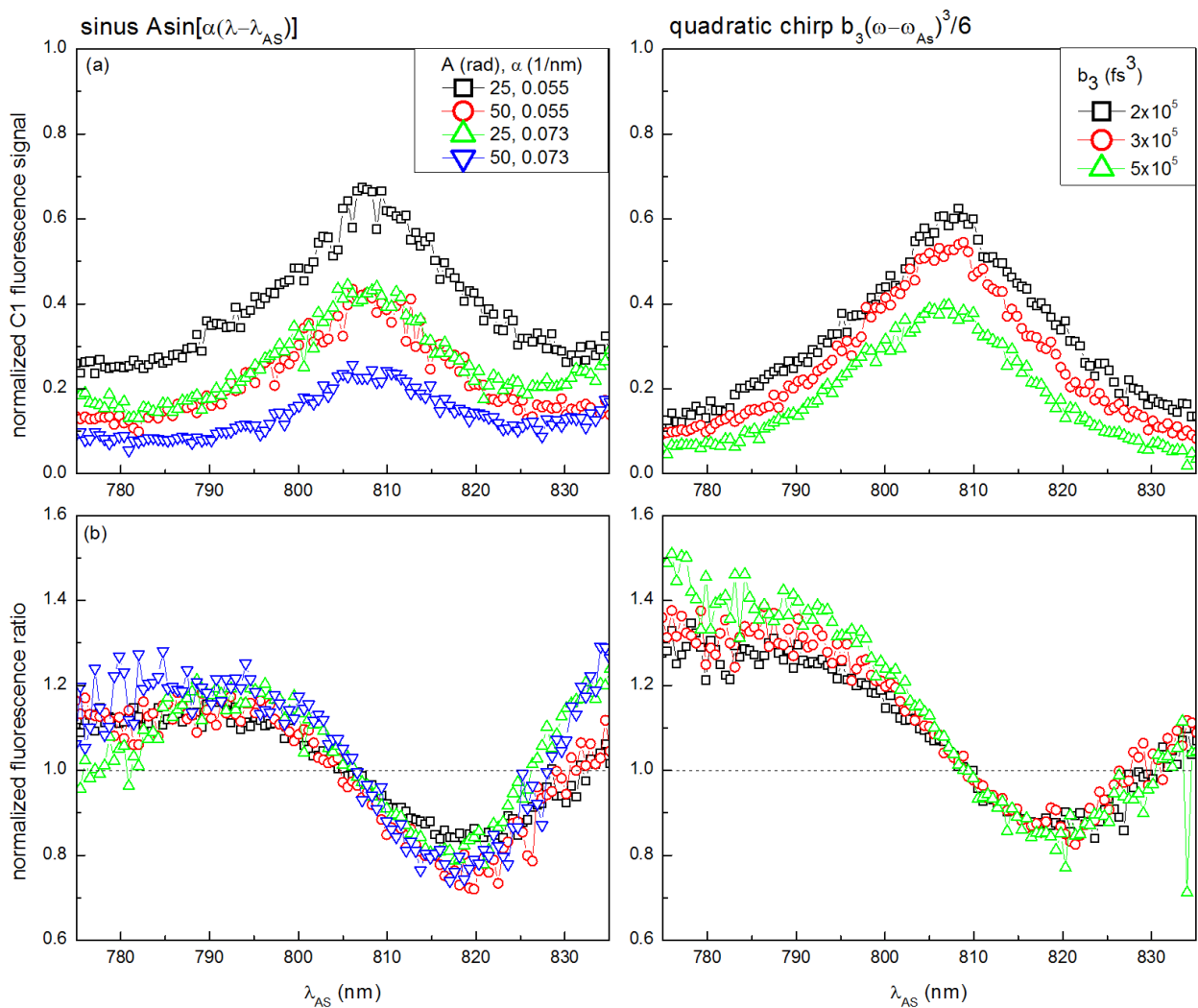


Figure 7.5: Selective excitation of C1 and RB with phase shaped pulses with sinusoidal (left) and third order polynomial (right) phase, with fiber: (a) normalized C1 fluorescence intensity and (b) normalized ratio between C1 and RB fluorescence.

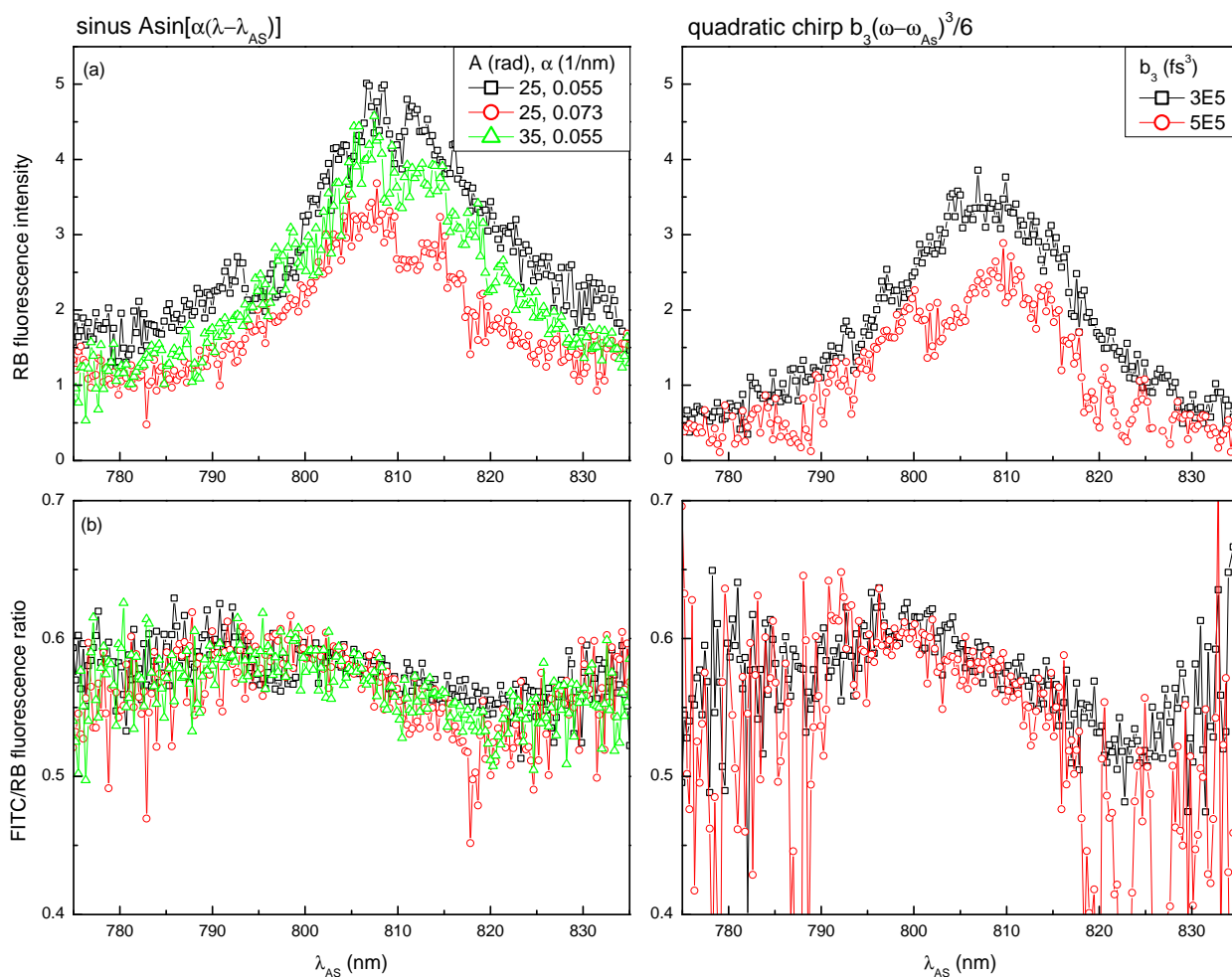


Figure 7.6: Selective excitation of FITC and RB with phase shaped pulses with sinusoidal (left) and third order polynomial (right) phase, with fiber: (a) RB fluorescence intensity and (b) ratio between FITC and RB fluorescence

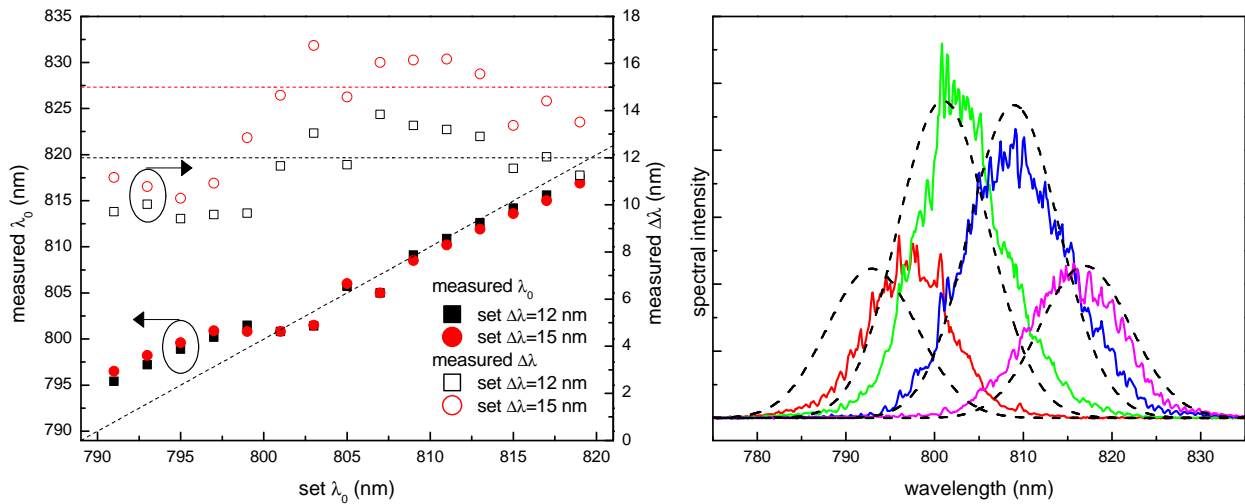


Figure 7.7: Short pulses with changing central wavelength obtained with reverse propagation. (a) Measured central wavelength λ_0 (solid symbols) and spectral width $\Delta\lambda$ (open symbols) for pulses with spectral width set to 12 nm (black squares) and 15 nm (red circles). Set λ_0 and $\Delta\lambda$ are marked with dashed lines. (b) Measured spectra after propagation through the fiber for $\Delta\lambda = 12$ nm and central wavelengths: 793 nm, 801 nm, 809 nm and 817 nm (solid line) compared to expected spectra (dashed line).

7.4 Phase and amplitude shaped pulses

In this section I present selective excitation with spectrally narrow short pulses with shifting central wavelength. The pulses are generated by amplitude shaping of the initial laser pulse and then transported through the fiber. I compare the results for pulses generated using the reverse propagation method described in chapter 6 and pulses with dispersion compensation only.

7.4.1 Pulses with variable central wavelength generated by reverse propagation

If a spectrally narrow pulse is generated by simply blocking parts of the spectrum of a broader pulse, its energy will vary depending on how much its central wavelength is detuned from the central wavelength of the initial pulse. In consequence, the amount of spectral narrowing during nonlinear propagation through the fiber will vary as well. Reverse propagation can account for that and enable generation of a series of pulses with shifting central wavelength but constant spectral width. To ensure that the pulses are generated correctly, their central wavelength and spectral widths were measured and compared to the desired values. The results are summarized in fig. 7.7. In fig. 7.7(a) systematic variation of the central wavelength for two spectral widths: 12 nm and 15 nm is shown. In fig. 7.7(b) examples of measured spectra are presented. There is some deviation from the desired spectral amplitude for the blue-detuned pulses but apart from that the measured spectra are close to the desired spectra. This is yet another proof that reverse propagation works well in this pulse energy regime.

7.4.2 Selective excitation results

The pulses described in the previous section were subsequently applied to selective TP excitation. For comparison, the same measurements were repeated with pulses with shifting central wave-

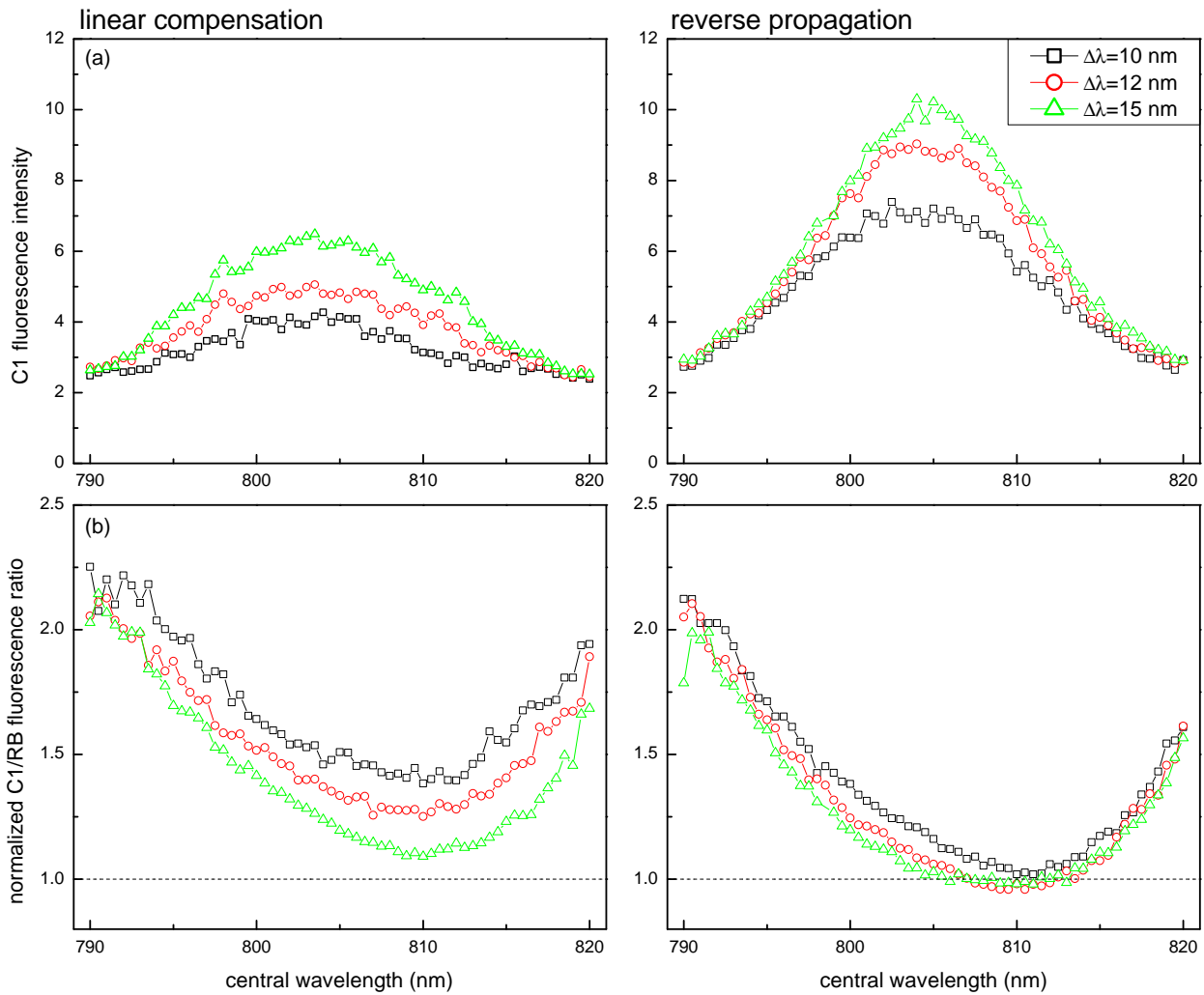


Figure 7.8: Selective excitation of C1 and RB with amplitude shaped pulses with shifting λ_0 and varying spectral width obtained by linear compensation (left) and reverse propagation (right): (a) fluorescence intensity of C1 and (b) normalized fluorescence ratio.

length generated by linear compensation, that is, ignoring the influence of nonlinear effects and only adding a phase offset compensating for the fiber dispersion.

Fig. 7.8 shows results obtained in the C1 and RB mixture and fig. 7.9 on the next page in the FITC and RB mixture. As in section 7.2, the measurement was repeated for different spectral widths. As expected, the fluorescence intensity depends strongly on the spectral width. In particular, $\Delta\lambda = 7$ nm was omitted because the signal was too low. Similarly to the measurements without the fiber, the fluorescence ratio shows only a weak dependence on the pulse width, so again the conclusion is that broader pulses yielding more signal are preferred.

In measurements presented here the pulses generated by reverse propagation result in a few times higher fluorescence intensity than the pulses obtained by linear compensation only. To confirm that the comparison is done correctly, the pulse energy for both series of pulses was measured directly after the fiber using a standard photodiode. In fig. 7.10 an example for $\Delta\lambda = 12$ nm is presented. Fig. 7.10(a) shows again the RB fluorescence intensity, much higher for the reverse propagation pulses, and 7.10(b) the photodiode signal, nearly identical for both series of pulses. The same was found for other $\Delta\lambda$. This shows clearly that the difference is in fact a consequence of the pulse shape and not simply pulse energy.

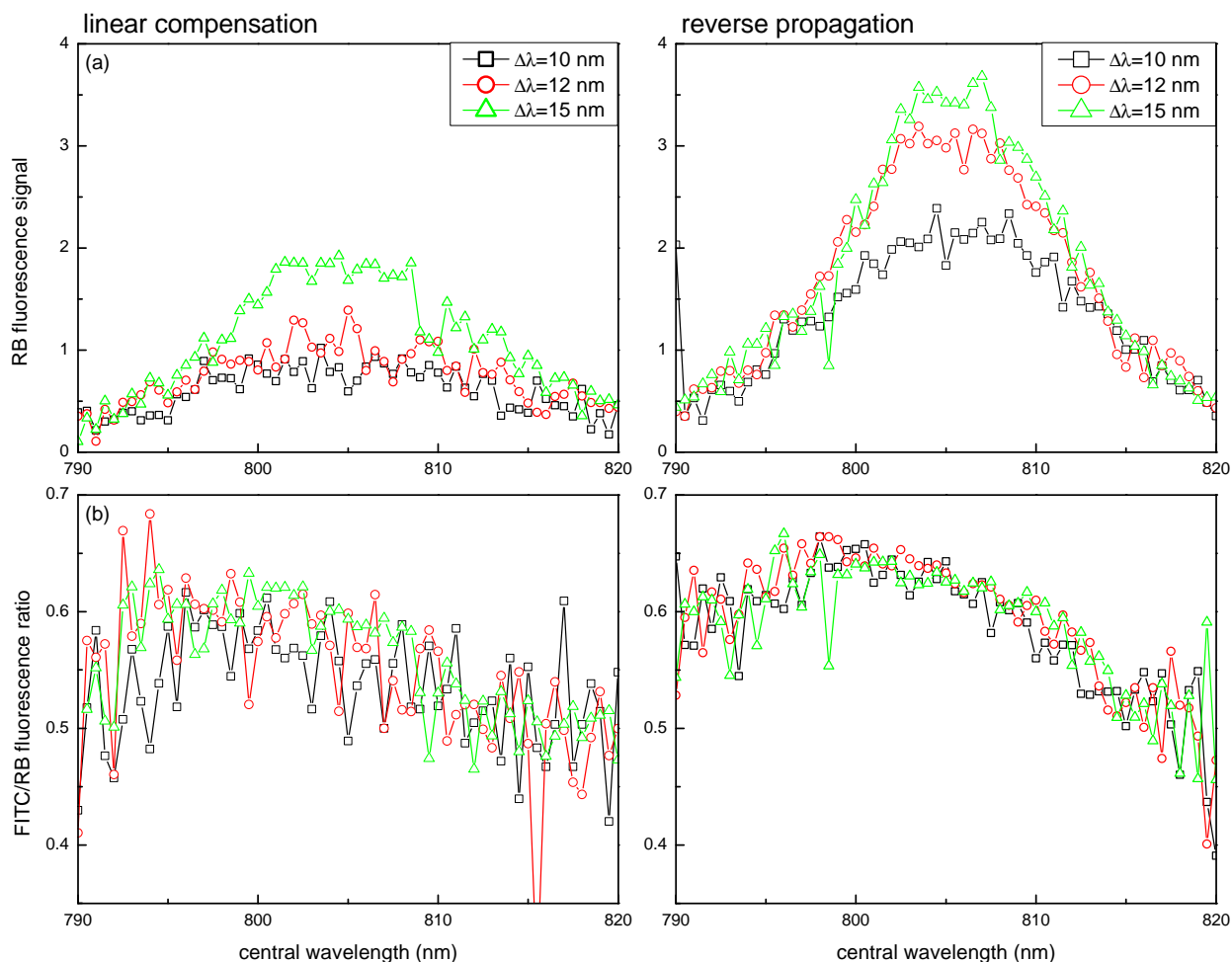


Figure 7.9: Selective excitation of FITC and RB with amplitude shaped pulses with shifting λ_0 for different $\Delta\lambda$ obtained by linear compensation (left) and reverse propagation (right): (a) fluorescence intensity of FITC and (b) fluorescence ratio.

As far as the fluorescence ratio is concerned, the difference between results obtained with the two pulse shaping methods is smaller, but also here the pulses generated by reverse propagation are superior to those generated by linear compensation. For the C1 and RB mixture the values are $\Gamma = 0.34$ and $\Gamma = 0.31$ respectively. For the FITC and RB mixture the values are difficult to determine because of the amount of noise. They are of the order of $\Gamma = 0.1$ and $\Gamma = 0.15$ which is still not that bad comparing to the value $\Gamma = 0.2$ without the fiber, but for an application in microscopy an improvement is necessary.

It is also interesting to compare the excitation efficiency achieved with the reverse propagation pulses to this achieved with the phase-only shaped pulses shown in the previous section. This has to be done carefully, using measurements performed in a single series to ensure that the pulse energy, position of the focus in the cuvette, integration time etc. were identical. This is the case for the FITC and RB measurements shown in figures 7.6 on page 94 and 7.9. The pulses with the sinusoidal phase achieve the best excitation efficiency, but then the fluorescence ratio stays almost constant. Because of that a comparison of the reverse propagation pulses to the pulses with third order polynomial phase that achieve a similar contrast is more meaningful. Although the energy of the pulses with shifting central wavelength was reduced due to amplitude shaping by a factor between 2 and 7 (depending on the spectral width and detuning from the central wavelength of the

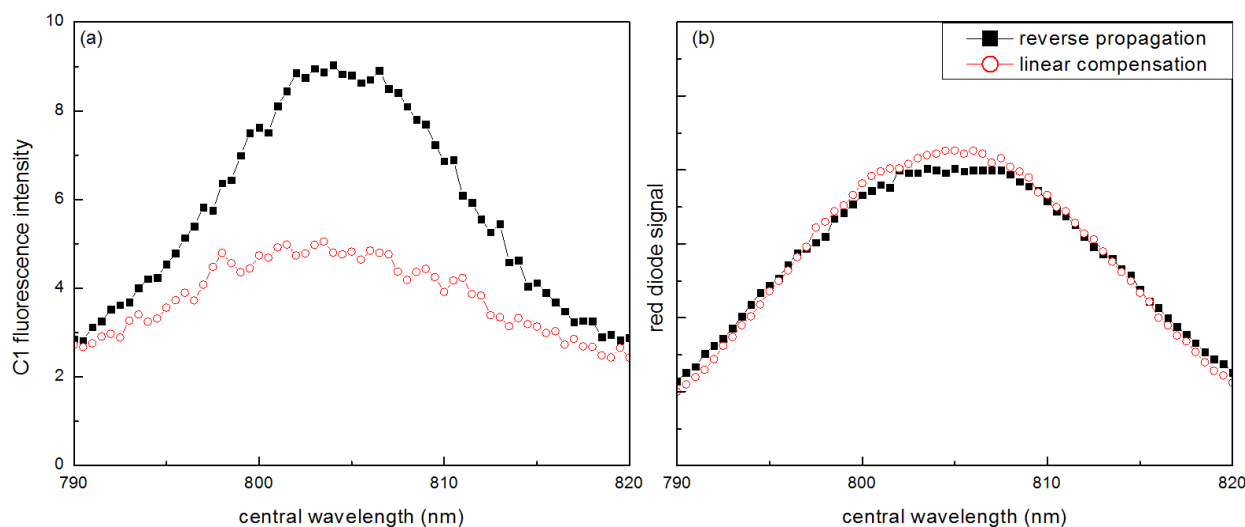


Figure 7.10: Comparison of (a) C1 fluorescence intensity and (b) photodiode signal for pulses with $\Delta\lambda=12$ nm and shifting λ_0 generated by reverse propagation (solid squares) and linear compensation (open circles).

laser pulse), the fluorescence signal is comparable to the signal obtained with phase-shaped pulses generated without reverse propagation. This can be explained by the pulses with shifting central wavelength being TL and not temporally stretched as the phase-shaped pulses. As a side effect, if a lower pulse energy is required for the same amount of signal, as it is the case here, sample damage by heating can be reduced.

7.5 Discussion

The measurements presented above show clearly that pulse shaping is a promising method for applications where selective two-photon excitation takes place in setups containing optical fibers, such as in vivo two-photon microscopy and imaging. Out of the different pulse shaping methods discussed here, reverse propagation is the best one. The pulses with shifting central wavelength generated by reverse propagation achieve simultaneously more contrast and signal than phase-only modulated pulses and pulses with shifting central wavelength obtained by linear compensation.

In principle, comparable results could be also obtained by other methods. Every pulse shape that is possible to generate by reverse propagation could be obtained by characterizing the pulse after the fiber and adapting the input pulse shape iteratively until the desired output pulse is reached. Another possibility is a multi-objective optimization algorithm (see section 5.2.2) with contrast and signal as optimization goals. However, these methods are not practical for TP microscopy. In the first case a bulky pulse characterization setup is required. For adaptive contrast optimization one needs to know a priori where the different areas of the sample are in order to have an observable that can be optimized. Compared to that, reverse propagation is quite simple. The fiber can be characterized before attaching it to the microscope and very little knowledge of the investigated sample itself is required. If one wants to avoid characterizing the fiber to simplify the experiment even more, then the phase-only shaped pulses with carefully chosen amount of quadratic chirp should be used.

The biggest limitation in my measurements was the modest spectral bandwidth of the pulse, especially if the spectral narrowing is taken into account. The measurements without the fiber presented in section 7.2, with the pulses that were not narrowed by SPM, indicate that it is possible to

obtain a higher contrast if more spectral bandwidth is available. Although it was not possible in the setup used in my work, generating and shaping pulses with up to 100 nm bandwidth is not an issue. When using broadband laser one has to choose the fiber carefully, but it has been reported that a pulse spectrum as broad as 120 nm can fully be transmitted (although with some modulations of unclear origin) through a polarization-maintaining single-mode fiber [84]. It would be interesting to combine a setup similar to the one described in [84] with the pulse shaping methods described in my work.

Summary

8

The aim of this work was developing methods of transporting shaped ultrashort pulses through an optical fiber and applying them to coherent control. For this two approaches were developed and tested in a series of experiments. The experiments were performed with 50 fs near-infrared pulses with energies of the order of 1 nJ and a 1 m long fused silica step-index fiber.

In the first part of this work I have investigated the possibility of coherent control of two-photon processes with phase-modulated pulses transported through the fiber. In the experiment laser pulses were formed by a pulse shaper, transported via an optical fiber where they experienced linear and nonlinear distortions and finally applied to excitation of two-photon transitions. SHG in crystals with different thickness was used as a model of the latter. I have shown that for transitions detuned from the doubled central frequency of the laser pulse the transform-limited pulse usually does not achieve the highest possible excitation efficiency. Moreover, I have demonstrated that antisymmetric spectral phase functions that in the linear regime can be used to excite narrow two-photon transitions selectively retain this ability even as the pulse is significantly modulated due to nonlinear effects. I investigated this effect in more detail for pulses with a π step spectral phase. By performing a simulation of nonlinear propagation in a fiber I have shown how the phase jump shifts with increasing pulse energy but its shape remains almost intact. Thus, if a suitable offset for dispersion compensation is applied, the phase of the output pulse stays approximately antisymmetric, although around a different point than initially.

In the second part I have presented the method of reverse propagation. The idea of combining numerical backward propagation with a pulse shaper for generating arbitrarily shaped pulses after the fiber has been proposed in literature but without experimental demonstration or any discussion of arising difficulties. This has been done in the course of this work. I have developed an algorithm that calculates the input pulse required to obtain a desired output pulse and from it the phase and transmission pattern to write on the modulator. Obtaining one pulse shape requires simulating the propagation only once, without the need to use iterative procedures. This is especially important because solving the nonlinear Schrödinger equation for a complex pulse propagating in a fiber is already a lengthy procedure due to the high sampling of the field and the number of steps required. I have also shown that this method is indeed capable of generating complex shaped pulses by obtaining a series of example pulses and characterizing them by cross-correlation with a broadband TL pulse.

One field where coherent control of multiphoton processes is especially relevant is nonlinear microscopy and imaging. To see if the methods developed in my work are suitable for this kind of application, I performed a series of measurements with selective excitation of molecules in solution. For I used laser dyes that exhibit TPA at the wavelength of the available laser pulse in a cuvette and collected the fluorescence with a pair of lenses and a spectrometer. Although this setup obviously is not capable of imaging, it is a good model of what happens in one particular point under a nonlinear microscope. Also the broad, overlapping spectra of the dyes are typical for fluorophores used in biological imaging. I have shown that both approaches presented in my work are suitable for efficient and selective excitation in such a system. The achieved contrast is lower than for the same measurements performed without fiber, but still reasonable. Most probably the results could be further improved if pulses with broader bandwidth were used.

Both approaches described in my work are not without limitations. The deviations from the expected result increase with increasing pulse energy so to extend these methods to pulse energies

higher than a few nJ further improvements are required. However, they have a clear advantage, in terms of efficiency and selectivity of excitation or generating the desired pulse shape, over the naive approach of neglecting the nonlinear effects and applying only a phase offset for dispersion compensation.

Bibliography

- [1] G. Agrawal. *Nonlinear Fiber Optics*. Academic Press, 2007.
- [2] R. Boyd. *Nonlinear Optics*. Academic Press, 2008.
- [3] Bahaa E. A. Saleh and Malvin Carl Teich. *Fundamentals of Photonics*. John Wiley & Sons, Inc., 2001.
- [4] D. Goswami. Optical pulse shaping approaches to coherent control. *Physics Reports*, 374(6):385 – 481, 2003.
- [5] Marcos Dantus and Vadim V. Lozovoy. Experimental coherent laser control of physico-chemical processes. *Chemical Reviews*, 104(4):1813–1860, 2004.
- [6] Sang-Hee Shim and Martin T. Zanni. How to turn your pump-probe instrument into a multidimensional spectrometer: 2D IR and vis spectroscopies via pulse shaping. *Physical Chemistry Chemical Physics*, 11(5):748, 2009.
- [7] Yaron Silberberg. Quantum coherent control for nonlinear spectroscopy and microscopy. *Annual Review of Physical Chemistry*, 60(1):277–292, 2009.
- [8] Antoine Monmayrant, Sébastien Weber, and Béatrice Chatel. A newcomer’s guide to ultrashort pulse shaping and characterization. *Journal of Physics B: Atomic, Molecular and Optical Physics*, 43(10):103001, 2010.
- [9] Paul Brumer and Moshe Shapiro. Control of unimolecular reactions using coherent light. *Chemical Physics Letters*, 126(6):541 – 546, 1986.
- [10] David J. Tannor and Stuart A. Rice. Control of selectivity of chemical reaction via control of wave packet evolution. *The Journal of Chemical Physics*, 83(10):5013–5018, 1985.
- [11] David J. Tannor, Ronnie Kosloff, and Stuart A. Rice. Coherent pulse sequence induced control of selectivity of reactions: Exact quantum mechanical calculations. *The Journal of Chemical Physics*, 85(10):5805–5820, 1986.
- [12] Anthony P. Peirce, Mohammed A. Dahleh, and Herschel Rabitz. Optimal control of quantum-mechanical systems: Existence, numerical approximation, and applications. *Phys. Rev. A*, 37:4950–4964, 1988.
- [13] Richard S. Judson and Herschel Rabitz. Teaching lasers to control molecules. *Physical Review Letters*, 68(10):1500, 1992.
- [14] Warren S. Warren, Herschel Rabitz, and Mohammed Dahleh. Coherent control of quantum dynamics: The dream is alive. *Science*, 259(5101):1581–1589, 1993.
- [15] D. Zeidler, S. Frey, K.-L. Kompa, and M. Motzkus. Evolutionary algorithms and their application to optimal control studies. *Phys. Rev. A*, 64:023420, 2001.
- [16] Matthew Comstock, Vadim Lozovoy, Igor Pastirk, and Marcos Dantus. Multiphoton intrapulse interference 6; binary phase shaping. *Optics Express*, 12(6):1061–1066, 2004.

- [17] T. Hornung, R. Meier, and M. Motzkus. Optimal control of molecular states in a learning loop with a parameterization in frequency and time domain. *Chemical Physics Letters*, 326(5-6):445–453, 2000.
- [18] S. M. Weber, A. Lindinger, F. Vetter, M. Plewicki, A. Merli, and L. Wöste. Application of parametric time and frequency domain shaping. *The European Physical Journal D - Atomic, Molecular, Optical and Plasma Physics*, 33:39–42, 2005. 10.1140/epjd/e2005-00033-9.
- [19] Stefan M. Weber, Mateusz Plewicki, Fabian Weise, and Albrecht Lindinger. Parametric polarization pulse shaping demonstrated for optimal control of NaK. *The Journal of Chemical Physics*, 128(17):174306, 2008.
- [20] F. Weise and A. Lindinger. Full parametric pulse shaping in phase, amplitude, and polarization using an effective four-array modulator. *Applied Physics B: Lasers and Optics*, 101:79–91, 2010. 10.1007/s00340-010-4038-2.
- [21] P. Wnuk and C. Radzewicz. Coherent control and dark pulses in second harmonic generation. *Optics Communications*, 272:496 – 502, 2007.
- [22] D. Yelin, D. Meshulach, and Y. Silberberg. Adaptive femtosecond pulse compression. *Opt. Lett.*, 22(23):1793–1795, 1997.
- [23] T. Baumert, T. Brixner, V. Seyfried, M. Strehle, and G. Gerber. Femtosecond pulse shaping by an evolutionary algorithm with feedback. *Applied Physics B: Lasers and Optics*, 65:779–782, 1997. 10.1007/s003400050346.
- [24] Patrick Nuernberger, Gerhard Vogt, Tobias Brixner, and Gustav Gerber. Femtosecond quantum control of molecular dynamics in the condensed phase. *Phys. Chem. Chem. Phys.*, 9(20):2470–2497, 2007.
- [25] Mathias Flörsheimer, Martin Bösch, Christof Brillert, Maria Wierschem, and Harald Fuchs. Second-harmonic microscopy - a quantitative probe for molecular surface order. *Advanced Materials*, 9(13):1061–1065, 1997.
- [26] Sophie Brasselet. Polarization-resolved nonlinear microscopy: application to structural molecular and biological imaging. *Advances in Optics and Photonics*, 3(3):205–271, 2011.
- [27] Doron Meshulach and Yaron Silberberg. Coherent quantum control of multiphoton transitions by shaped ultrashort optical pulses. *Physical Review A*, 60(2):1287, 1999.
- [28] Nirit Dudovich, Barak Dayan, Sarah M. Gallagher Faeder, and Yaron Silberberg. Transform-Limited pulses are not optimal for resonant multiphoton transitions. *Physical Review Letters*, 86(1):47, 2001.
- [29] P. Panek and A. Becker. Dark pulses for resonant two-photon transitions. *Physical Review A*, 74(2):023408, 2006.
- [30] D. Meshulach and Y. Silberberg. Coherent quantum control of two-photon transitions by a femtosecond laser pulse. *Nature*, 396:239–242, 1998.
- [31] Igor Pastirk, Johanna Dela Cruz, Katherine Walowicz, Vadim Lozovoy, and Marcos Dantus. Selective two-photon microscopy with shaped femtosecond pulses. *Optics Express*, 11(14):1695–1701, 2003.

- [32] Jennifer P. Ogilvie, Delphine Débarre, Xavier Solinas, Jean-Louis Martin, Emmanuel Beau-repaire, and Manuel Joffre. Use of coherent control for selective two-photon fluorescence microscopy in live organisms. *Optics Express*, 14(2):759–766, 2006.
- [33] Vadim V. Lozovoy, Igor Pastirk, Katherine A. Walowicz, and Marcos Dantus. Multiphoton intrapulse interference. II. control of two- and three-photon laser induced fluorescence with shaped pulses. *The Journal of Chemical Physics*, 118(7):3187, 2003.
- [34] M. Oberthaler and R. A. Höpfel. Special narrowing of ultrashort laser pulses by self-phase modulation in optical fibers. *Applied Physics Letters*, 63(8):1017, 1993.
- [35] Henry Hurwitz Jr. and R. Clark Jones. A new calculus for the treatment of optical systems. *J. Opt. Soc. Am.*, 31(7):493–498, 1941.
- [36] T. Brabec, Ch. Spielmann, P. F. Curley, and F. Krausz. Kerr lens mode locking. *Opt. Lett.*, 17(18):1292–1294, 1992.
- [37] Coherent. The Coherent Mira Seed Laser. Operator’s Manual, 1997.
- [38] Coherent. RegA Model 9050 Laser. Operator’s Manual, 2002.
- [39] Fabian Weise. *Parametric polarization pulse shaping methods and control of excitation dynamics in ultracold rubidium*. PhD thesis, Freie Universität Berlin, 2010.
- [40] Donna Strickland and Gerard Mourou. Compression of amplified chirped optical pulses. *Optics Communications*, 55(6):447 – 449, 1985.
- [41] G. Pretzler, A. Kasper, and K. J. Witte. Angular chirp and tilted light pulses in CPA lasers. *Applied Physics B: Lasers and Optics*, 70:1–9, 2000.
- [42] K. Osvay, A. P Kovacs, Z. Heiner, G. Kurdi, J. Klebniczki, and M. Csatari. Angular dispersion and temporal change of femtosecond pulses from misaligned pulse compressors. *IEEE Journal of Selected Topics in Quantum Electronics*, 10(1):213– 220, 2004.
- [43] F. Verluise, V. Laude, Z. Cheng, Ch. Spielmann, and P. Tournois. Amplitude and phase control of ultrashort pulses by use of an acousto-optic programmable dispersive filter: pulse compression and shaping. *Opt. Lett.*, 25(8):575–577, 2000.
- [44] A. M. Weiner. Femtosecond pulse shaping using spatial light modulators. *Review of Scientific Instruments*, 71(5):1929, 2000.
- [45] Marc M. Wefers and Keith A. Nelson. Generation of high-fidelity programmable ultrafast optical waveforms. *Opt. Lett.*, 20(9):1047–1049, 1995.
- [46] C. Froehly, B. Colombeau, and M. Vampouille. II Shaping and analysis of picosecond light pulses. volume 20 of *Progress in Optics*, pages 63 – 153. Elsevier, 1983.
- [47] T. Brixner and G. Gerber. Femtosecond polarization pulse shaping. *Opt. Lett.*, 26(8):557–559, 2001.
- [48] T. Brixner, G. Krampert, T. Pfeifer, R. Selle, G. Gerber, M. Wollenhaupt, O. Graefe, C. Horn, D. Liese, and T. Baumert. Quantum control by ultrafast polarization shaping. *Physical Review Letters*, 92(20):208301, 2004.

- [49] Fabian Weise and Albrecht Lindinger. Full control over the electric field using four liquid crystal arrays. *Optics Letters*, 34(8):1258–1260, 2009.
- [50] Mateusz Plewicki, Fabian Weise, Stefan M. Weber, and Albrecht Lindinger. Phase, amplitude, and polarization shaping with a pulse shaper in a Mach-Zehnder interferometer. *Applied Optics*, 45(32):8354–8359, 2006.
- [51] Omid Masihzadeh, Philip Schlup, and Randy A. Bartels. Complete polarization state control of ultrafast laser pulses with a single linearspatial light modulator. *Optics Express*, 15(26):18025–18032, 2007.
- [52] David Kupka, Philip Schlup, and Randy A. Bartels. Simplified ultrafast pulse shaper for tailored polarization states using a birefringent prism. *Review of Scientific Instruments*, 80(5):053110, 2009.
- [53] M. Plewicki, S.M. Weber, F. Weise, and A. Lindinger. Independent control over the amplitude, phase, and polarization of femtosecond pulses. *Applied Physics B: Lasers and Optics*, 86:259–263, 2007. 10.1007/s00340-006-2464-y.
- [54] David J. McCabe, Dane R. Austin, Ayhan Tajalli, Sébastien Weber, Ian A. Walmsley, and Béatrice Chatel. Space-time coupling of shaped ultrafast ultraviolet pulses from an acousto-optic programmable dispersive filter. *Journal of the Optical Society of America B*, 28(1):58–64, 2011.
- [55] Marc M. Wefers and Keith A. Nelson. Analysis of programmable ultrashort waveform generation using liquid-crystal spatial light modulators. *Journal of the Optical Society of America B*, 12(7):1343–1362, 1995.
- [56] C. Dorrer and F. Salin. Phase amplitude coupling in spectral phase modulation. *Selected Topics in Quantum Electronics, IEEE Journal of*, 4(2):342–345, 1998.
- [57] Benjamin J. Sussman, Rune Lausten, and Albert Stolow. Focusing of light following a 4-f pulse shaper: Considerations for quantum control. *Physical Review A*, 77(4):043416, 2008.
- [58] F. Frei, A. Galler, and T. Feurer. Space-time coupling in femtosecond pulse shaping and its effects on coherent control. *The Journal of Chemical Physics*, 130(3):034302, 2009.
- [59] Joshua Vaughan, T. Feurer, Katherine Stone, and Keith Nelson. Analysis of replica pulses in femtosecond pulse shaping with pixelated devices. *Opt. Express*, 14(3):1314–1328, 2006.
- [60] Ian A. Walmsley and Christophe Dorrer. Characterization of ultrashort electromagnetic pulses. *Advances in Optics and Photonics*, 1(2):308–437, 2009.
- [61] D.J. Kane and R. Trebino. Characterization of arbitrary femtosecond pulses using frequency-resolved optical gating. *Quantum Electronics, IEEE Journal of*, 29(2):571–579, 1993.
- [62] John N. Sweetser, David N. Fittinghoff, and Rick Trebino. Transient-grating frequency-resolved optical gating. *Opt. Lett.*, 22(8):519–521, 1997.
- [63] Bruno E. Schmidt, Waldemar Unrau, Aldo Mirabal, Shaohui Li, Marcel Krenz, Ludger Wöste, and Torsten Siebert. Poor man’s source for sub 7 fs: a simple route to ultrashort laser pulses and their full characterization. *Optics Express*, 16(23):18910–18921, 2008.

- [64] Jinendra K. Ranka, Alexander L. Gaeta, Andrius Baltuska, Maxim S. Pshenichnikov, and Douwe A. Wiersma. Autocorrelation measurement of 6-fs pulses based on the two-photon-induced photocurrent in a GaAsP photodiode. *Optics Letters*, 22(17):1344–1346, 1997.
- [65] Nona Rahmat. Selektive zweiphotonische Anregung in Farbstoff-Mischungen. Master's thesis, Freie Universität Berlin, 2012.
- [66] Jennifer P. Ogilvie, Kevin J. Kubarych, Antigoni Alexandrou, and Manuel Joffre. Fourier transform measurement of two-photon excitation spectra: applications to microscopy and optimal control. *Opt. Lett.*, 30(8):911–913, 2005.
- [67] Nikolay S. Makarov, Mikhail Drobizhev, and Aleksander Rebane. Two-photon absorption standards in the 550-1600 nm excitation wavelength range. *Opt. Express*, 16(6):4029–4047, 2008.
- [68] J. P. Gordon and H. Kogelnik. PMD fundamentals: Polarization mode dispersion in optical fibers. *Proceedings of the National Academy of Sciences*, 97(9):4541–4550, 2000.
- [69] F. Weise, M. Pawłowska, G. Achazi, and A. Lindinger. Parametrically phase-, amplitude-, and polarization-shaped femtosecond laser pulses guided via a step-index fiber. *Journal of the Optical Society of America B*, 28(3):406–415, 2011.
- [70] Fabian Weise, Monika Pawłowska, Georg Achazi, and Albrecht Lindinger. Full control of polarization and temporal shape of ultrashort laser pulses transmitted through an optical fibre. *Journal of Optics*, 13(7):075301, 2011.
- [71] B. Schmidt, M. Hacker, G. Stobrawa, and T. Feurer. Lab2-a virtual femtosecond laser lab.
- [72] Jinendra K. Ranka, Robert S. Windeler, and Andrew J. Stentz. Visible continuum generation in air-silica microstructure optical fibers with anomalous dispersion at 800 nm. *Opt. Lett.*, 25(1):25–27, 2000.
- [73] D. Mogilevtsev, T. A. Birks, and P. St. J. Russell. Group-velocity dispersion in photonic crystal fibers. *Opt. Lett.*, 23(21):1662–1664, 1998.
- [74] G. Stobrawa, M. Hacker, R. Netz, M. Bischoff, and R. Sauerbrey. Novel technique for the measurement of fiber dispersion properties. *Applied Physics B: Lasers and Optics*, 76(3):333–336, 2003.
- [75] Stefan Weber. *New concepts for optimal control experiments using femtosecond pulse shaping*. PhD thesis, Freie Universität Berlin, 2007.
- [76] Albrecht Lindinger, Stefan M. Weber, Cosmin Lupulescu, Franziska Vetter, Mateusz Plewicki, Andrea Merli, Ludger Wöste, Andreas F. Bartelt, and Herschel Rabitz. Revealing spectral field features and mechanistic insights by control pulse cleaning. *Physical Review A*, 71(1):013419, 2005.
- [77] S. M. Weber, F. Sauer, M. Plewicki, A. Merli, L. Wöste, and A. Lindinger. Multi-objective optimization on alkali dimers. *Journal of Modern Optics*, 54(16-17):2659–2666, 2007.
- [78] Takeshi Yasui, Yoshiyuki Tohno, and Tsutomu Araki. Determination of collagen fiber orientation in human tissue by use of polarization measurement of molecular Second-Harmonic-Generation light. *Applied Optics*, 43(14):2861–2867, 2004.

- [79] Peter Schön, Martin Behrndt, Dora Aït-Belkacem, Hervé Rigneault, and Sophie Brasselet. Polarization and phase pulse shaping applied to structural contrast in nonlinear microscopy imaging. *Physical Review A*, 81(1):013809, 2010.
- [80] Ling Fu and Min Gu. Polarization anisotropy in fiber-optic second harmonic generation microscopy. *Optics Express*, 16(7):5000–5006, 2008.
- [81] C.-C. Chang, H. P. Sardesai, and A. M. Weiner. Dispersion-free fiber transmission for femtosecond pulses by use of a dispersion-compensating fiber and a programmable pulse shaper. *Opt. Lett.*, 23(4):283–285, 1998.
- [82] S. W. Clark, F. Ö. Ilday, and F. W. Wise. Fiber delivery of femtosecond pulses from a ti:sapphire laser. *Optics Letters*, 26(17):1320–1322, 2001.
- [83] S. H. Lee, A. L. Cavalieri, D. M. Fritz, M. Myaing, and D. A. Reis. Adaptive dispersion compensation for remote fiber delivery of near-infrared femtosecond pulses. *Opt. Lett.*, 29(22):2602–2604, 2004.
- [84] Adam M. Larson and Alvin T. Yeh. Delivery of sub-10-fs pulses for nonlinear optical microscopy by polarization-maintaining single mode optical fiber. *Optics Express*, 16(19):14723–14730, 2008.
- [85] Tuan Le, Gabriel Tempea, Zhao Cheng, Martin Hofer, and Andreas Stingl. Routes to fiber delivery of ultra-short laser pulses in the 25 fs regime. *Optics Express*, 17(3):1240–1247, 2009.
- [86] Werner Göbel, Axel Nimmerjahn, and Fritjof Helmchen. Distortion-free delivery of nano-joule femtosecond pulses from a ti:sapphire laser through a hollow-core photonic crystal fiber. *Optics Letters*, 29(11):1285–1287, 2004.
- [87] Amnon Yariv, Dan Fekete, and David M. Pepper. Compensation for channel dispersion by nonlinear optical phase conjugation. *Opt. Lett.*, 4(2):52–54, 1979.
- [88] Robert A. Fisher, B. R. Suydam, and D. Yevick. Optical phase conjugation for time-domain undoing of dispersive self-phase-modulation effects. *Opt. Lett.*, 8(12):611–613, 1983.
- [89] Mankei Tsang and Demetri Psaltis. Dispersion and nonlinearity compensation by spectral phase conjugation. *Optics Letters*, 28(17):1558–1560, 2003.
- [90] Onur Kuzucu, Yoshitomo Okawachi, Reza Salem, Mark A. Foster, Alexander L. Gaeta, Amy C. Turner-Foster, and Michal Lipson. Dispersion and nonlinearity compensation using spectral phase conjugation. In *Conference on Lasers and Electro-Optics/International Quantum Electronics Conference*, page CPDB3. Optical Society of America, 2009.
- [91] Mankei Tsang, Demetri Psaltis, and Fiorenzo G. Omenetto. Reverse propagation of femtosecond pulses in optical fibers. *Opt. Lett.*, 28(20):1873–1875, 2003.
- [92] Rameez Asif, Chien-Yu Lin, M. Holtmannspoetter, and Bernhard Schmauss. Optimized digital backward propagation for phase modulated signals in mixed-optical fiber transmission link. *Opt. Express*, 18(22):22796–22807, 2010.

- [93] Eduardo F. Mateo, Fatih Yaman, and Guifang Li. Efficient compensation of inter-channel nonlinear effects via digital backward propagation in wdm optical transmission. *Opt. Express*, 18(14):15144–15154, 2010.
- [94] David Milam. Review and assessment of measured values of the nonlinear Refractive-Index coefficient of fused silica. *Applied Optics*, 37(3):546–550, 1998.
- [95] Stéphane Santran, Lionel Canioni, Laurent Sarger, Thierry Cardinal, and Evelyne Fargin. Precise and absolute measurements of the complex third-order optical susceptibility. *J. Opt. Soc. Am. B*, 21(12):2180–2190, 2004.
- [96] Eduardo Mateo, Likai Zhu, and Guifang Li. Impact of xpm and fwm on the digital implementation of impairment compensation for wdm transmission using backward propagation. *Opt. Express*, 16(20):16124–16137, 2008.
- [97] Eduardo F. Mateo, Fatih Yaman, and Guifang Li. Efficient compensation of inter-channel nonlinear effects via digital backward propagation in wdm optical transmission. *Opt. Express*, 18(14):15144–15154, 2010.
- [98] K. Isobe, A. Suda, M. Tanaka, H. Hashimoto, F. Kannari, H. Kawano, H. Mizuno, A. Miyawaki, and K. Midorikawa. Nonlinear optical microscopy and spectroscopy employing octave spanning pulses. *IEEE Journal of Selected Topics in Quantum Electronics*, 16(4):767–780, 2010.
- [99] Robert Hellwarth and Paul Christensen. Nonlinear optical microscopic examination of structure in polycrystalline ZnSe. *Optics Communications*, 12(3):318–322, 1974.
- [100] W. Denk, J. H. Strickler, and W. W. Webb. Two-Photon laser scanning fluorescence microscopy. *Science*, 248(4951):73–76, 1990.
- [101] Katherine A. Walowicz, Igor Pastirk, Vadim V. Lozovoy, and Marcos Dantus. Multiphoton intrapulse interference. 1. Control of multiphoton processes in condensed phases. *The Journal of Physical Chemistry A*, 106(41):9369–9373, 2002.
- [102] Guillaume Labroille, Rajesh S. Pillai, Xavier Solinas, Caroline Boudoux, Nicolas Olivier, Emmanuel Beaurepaire, and Manuel Joffre. Dispersion-based pulse shaping for multiplexed two-photon fluorescence microscopy. *Optics Letters*, 35(20):3444–3446, 2010.
- [103] L. Fu and M. Gu. Fibre-optic nonlinear optical microscopy and endoscopy. *Journal of Microscopy*, 226(3):195–206, 2007.

List of publications

- **M. Pawłowska**, N. Rahmat, G. Achazi, A. Patas, and A. Lindinger, “Selective excitation with shaped pulses transported through a fiber using reverse propagation”, submitted in April 2012
- **M. Pawłowska**, A. Patas, G. Achazi, and A. Lindinger, “Parametrically shaped femtosecond pulses in the nonlinear regime obtained by reverse propagation in an optical fiber”, *Optics Letters* 37, 13, 2709-2711 (2012)
- **M. Pawłowska**, A. Patas, G. Achazi, N. Rahmat, F. Weise, and A. Lindinger, “Shaped pulses transported through an optical fiber in the nonlinear regime for selective excitation of two-photon transitions”, *Journal of Optical Society America B*. 29, 4, 833-840 (2012).
- **M. Pawłowska**, A. Patas, G. Achazi, N. Rahmat, and A. Lindinger, “Transporting shaped pulses through an optical fiber in the nonlinear regime for selective excitation of two-photon transitions”, *CLEO/Europe and EQEC 2011 Conference Digest, OSA Technical Digest (CD)* (Optical Society of America, 2011), paper *CFP4*.
- F. Weise, **M. Pawłowska**, G. Achazi, and A. Lindinger, “Full control of polarization and temporal shape of ultrashort laser pulses transmitted through an optical fibre”, *Journal of Optics* 13, 7, 075301 (2011).
- F. Weise, G. Achazi, **M. Pawłowska** and A. Lindinger, “Systematic variation of parametrically shaped sub-pulse sequences after transmission through a photonic crystal fiber”, *Optics Communications*, 284, 15, 3759-3771 (2011)
- G. Achazi, A. Patas, F. Weise, **M. Pawłowska**, and A. Lindinger, “Reconstruction of polarization-shaped laser pulses after a hollow-core fiber using backreflection”. *Applied Optics* 50, 6, 915-923 (2011)
- F. Weise, **M. Pawłowska**, G. Achazi, and A. Lindinger, “Parametrically phase-, amplitude-, and polarization-shaped femtosecond laser pulses guided via a step-index fiber”, *Journal of Optical Society of America B* 28, 406-415 (2011)

Acknowledgements

First of all, I would very much like to thank Prof. Ludger Wöste for giving me the opportunity to work in his group, for creating a friendly atmosphere and most importantly for never letting us forget that physics is fun.

I sometimes say that the best thing about doing physics is the chance to work with other physicists. So here I would like to thank Fabian Weise, Georg Achazi and Alexander Patas, as well as Falko Schwaneberg and Mathieu Lalanne and all the other people with whom I worked together at various times.

I am grateful to Albrecht Lindinger for supervising my work and all the discussions and help, Cristina Stanca-Kaposta for being a friend and a mentor at the same time, Jörg Wichmann for coffee and optimism, Kamil Stelmaszczyk for all his friendship, Alexander Kothe and the rest of the Aziz team for the very interesting if also exhausting adventure in BESSY, as well as Nona Rahmat, Frauke Eimer, Oliver Gause, Franz Hagemann, Mathias Holz and all the others from the Wöste group.

Further thanks go to Brigitte Odeh, Thomas Zuschneid and Angelika Pasanec for patient help with all kinds of organizational issues and to Volker Jornitz, Martin Rust, Detlef Müller, Michael Kregielski and the rest of technical staff for knowing how to turn vague ideas into reality.

I remain grateful to prof. Czesław Radzewicz, Dr. Piotr Fita and other wonderful people from the Ultrafast Processes Laboratory in the University of Warsaw, who taught me my way around a femtosecond laser lab during my Master studies and afterwards continued to inspire me and discuss physics and life by email and instant messengers.

I would like to acknowledge the financial support of Sonderforschungsbereich 450 and of Studienstiftung des deutschen Volkes.

And last but not least, I have to thank my family and friends for encouraging and supporting me and patiently waiting out the phases when I was too busy and stressed out to tell them how important they were to me.

Curriculum Vitae

For reasons of data protection,
the curriculum vitae is not included in the online version

Eidstattliche Erklärung

Ich versichere, dass ich diese Arbeit selbständig verfasst und keine anderen als die angegebenen Quellen und Hilfsmittel verwendet habe.

Berlin, 29.06.2012

Ort, Datum

.....

Unterschrift